RHODES UNIVERSITY

MASTER'S OF SCIENCE THESIS

Studying the brightest radio sources in the southern sky

Author:
Precious Katlego Sejake

Supervisors:
Dr. Sarah V. White
Dr. Sphesihle Makhathini
Prof. Ian Heywood

Orcid iD number:
https://orcid.org/0000-0002-1588-0384

A thesis submitted in fulfillment of the requirements
for the degree of Master's of science

in the

Faculty of Science
Department of Physics and Electronics

March 11, 2022

Declaration of Authorship

I, Precious Katlego Sejake, declare that this thesis titled, "Studying the brightest radio sources in the southern sky" and the work presented in it are my own. I confirm that:

- This work was done wholly or mainly while in candidature for a research degree at this University.
- Where any part of this thesis has previously been submitted for a degree or any other qualification at this University or any other institution, this has been clearly stated.
- Where I have consulted the published work of others, this is always clearly attributed.
- Where I have quoted from the work of others, the source is always given. With the exception of such quotations, this thesis is entirely my own work.
- I have acknowledged all main sources of help.
- Where the thesis is based on work done by myself jointly with others, I have made clear exactly what was done by others and what I have contributed myself.

Signed: 

Date: 11/03/2022

Abstract

Active Galactic Nuclei (AGN) are among the most remarkable and powerful extra-galactic radio sources in the Universe. The study of AGN enables us to understand better the critical mechanisms leading to the launch of radio jets, and its link to the central engine. Radio jets are thought to impact their host galaxy by promoting or suppressing star formation. By studying AGN, we can better understand their formation, evolution, and environment.

The host galaxy cross-identification is a crucial step to be carried out to build a multi-wavelength analysis of powerful radio sources; AGN. The GaLactic and Extra-galactic All-sky Murchison Widefield Array (GLEAM) 4Jy (G4Jy) Sample comprises 1,863 of the powerful radio sources in the southern sky. However, 140 sources from the G4Jy Sample were followed-up with the Open Time on MeerKAT. Of these 140 sources, 126 had an ambiguous host galaxy, and 13 had an identified host galaxy; however, there were some discrepancies in the literature concerning the host galaxy. The host-galaxy identification of these sources is limited by the poor resolution of radio data at 25" to 45".

This study aims to assess the radio morphology of these 140 sources and identify their host galaxy using the $\sim 7''$ resolution images from MeerKAT in conjunction with datasets at other wavelengths. This analysis is carried out by visually inspecting the overlays. The overlays comprise radio contours from 150 MHz, 200 MHz, 843/1400 MHz and 1300 MHz overlaid on the mid-infrared image (3.4 μm).

The MeerKAT images reveal sources with various radio morphologies. While most of the sources have radio morphology of typical symmetric lobes, 10 radio sources have head-tail morphology, 14 are wide-angle tail (WAT), and 5 have X-, S-/Z-shaped morphology. Overall, we find host galaxies for 70% of the sources in the sample, with the remainder comprising sources with ambiguous host galaxy (20.7%) and sources with a faint mid-infrared host galaxy (9.3%). These results highlight the importance of angular resolution and sensitivity for morphological classification and host galaxy cross-identification.

Acknowledgements

I would like to start by extending my sincere, most profound gratitude to my Supervisors; Dr Sarah V. White, Professor Ian Heywood and Dr Sphesihle Makhathini, for taking me as their student and guiding me throughout this research. Particularly I would like to thank Dr Sarah White for her patience, valuable inputs, always encouraging me to take care of myself mentally and physically. Many thanks to Prof Ian Heywood for providing me with images and reducing the MeerKAT data.

I would like to extend my deepest gratitude to the South African Radio Astronomy Observatory (SARAO) for offering me a scholarship to pursue this research. I would not have been able to enrol for this research if it was not for SARAO funding.

I would like to thank my family for their prayers, words of encouragement and the support they have given me during this research. Finally, I would like to thank the Rhodes Centre for Radio Astronomy Techniques & Technologies (RATT) group for making our work environment very conducive.

Contents

List of Figures

List of Tables

List of Abbreviations

AGN	Active Galactic Nuclei
BLRGs	Broad-Line Radio Galaxies
CASA	Common Astronomy Software Applications
FITS	Flexible Image Transport System
FR I	Fanaroff–Riley type I
FR II	Fanaroff–Riley type II
FSRQs	Flat Spectrum Radio Quasars
GLEAM	GaLactic and Extragalactic All-sky MWA
G4Jy	GLEAM four Jansky
GMRT	Giant Metrewave Radio Telescope
GRG	Giant Radio Galaxy
HST	Hubble Space Telescope
IFRS	Infrared Faint Radio Sources
ISM	Inter-Stellar Medium
MS	Measurement Set
MWA	Murchison Widefield Array
NAT	Narrow-Angle Tail
NLRGs	Narrow-Line Radio Galaxies
NRAO	National Radio Astronomy Observatory
NVSS	NRAO VLA Sky Survey
QSO	Quasi Stellar Objects
RFI	Radio Frequency Interference
RL AGN	Radio Loud AGN
RQ AGN	Radio Quiet AGN
SDSS	Sloan Digital Sky Survey
SKA	Square Kilometre Array
SMBH	SuperMassive Black Hole
SSRQs	Steep Spectrum Radio Quasars
TGSS	TIFR GMRT Sky Survey
TIFR	Tata Institute of Fundamental Research
UKST	UK Schmidt Telescope
VLA	Very Large Array

WAT	Wide-Angle Tail
2dFGRS	Two degree Field Galaxy Redshift Survey
2MASS	Two Micron All Sky Survey
2MRS	2MASS Redshift Survey
6dFGS	Six degree Field Galaxy Survey

Physical Constants

Speed of Light	$c_0 = 2.997\,924\,58 \times 10^8\,\mathrm{m\,s^{-1}}$ (exact)
Solar Luminosity	$L_\odot = 3.826 \times 10^{26}\,\mathrm{W}$
Hubble's constant	$H_0 = 70\,\mathrm{km\,s^{-1}\,Mpc^{-1}}$
Matter density parameter	$\Omega_m = 0.3$
Dark energy density parameter	$\Omega_\Lambda = 0.7$
Jansky	$1\,\mathrm{Jy} = 10^{-26}\,\mathrm{W\,m^{-2}\,Hz^{-1}}$

List of Symbols

F_B	Optical (B band) flux density	Jy
F_5	Radio (5 GHz) flux density	Jy
α	Spectral index	
S	Flux density	Jy
ν	Observing frequency	Hz
BMAJ	Beam major axis	$^\circ$
BMIN	Beam minor axis	$^\circ$
BPA	Position angle	$^\circ$
R.A.	Right Ascension	$^\circ$
Dec.	Declination	$^\circ$
b	Galactic latitude	$^\circ$
z	Redshift	
$L_{1.3\ \mathrm{GHz}}$	Radio luminosity at 1.3 GHz	$\mathrm{W\,Hz^{-1}}$
$S_{int1.3\ \mathrm{GHz}}$	Integrated flux density at 1.3 GHz	Jy
$S_{core1.3\ \mathrm{GHz}}$	Core intensity at 1.3 GHz	Jy
σ	RMS noise	$\mathrm{mJy\,beam^{-1}}$

Dedicated to to my daughter; Thuto Sejake...

Chapter 1

Introduction

Galaxies are the main observable components of the Universe. Up to now, a number of studies have shown that almost all galaxies harbour a supermassive black hole (SMBH) at their centre ranging from 10^6 to 10^{10} solar masses (Kormendy and Richstone, 1995). About 1% of galaxies are known to have a compact nucleus whose light outshines that of the entire galaxy. This very luminous compact nucleus, powered by the SMBH, is known as an active galactic nucleus (AGN). Studies of AGNs are crucial in understanding the formation and evolution of galaxies. To date, several studies have revealed strong correlations between the SMBH properties and their host galaxy (Gebhardt et al., 2000; Greene and Ho, 2006). These correlations suggest a connection between the central SMBH activity and the evolution of galaxies.

1.1 Galaxies and their evolution

Galaxies are systems of stars, the intergalactic medium (gas and dust), and dark matter bound together by gravity. They are diverse objects classified according to characteristics such as stellar population mass, age, morphology, size, colour or nuclear activity. The environment in which a galaxy resides has a tremendous impact on its physical properties. For instance, the merger or interaction between two galaxies causes dust and gas flow and disturbs their morphology. The morphological classification of galaxies dates back to the 20th century; Hubble (1926) classified galaxies into three categories; elliptical, spiral and irregular (Figure 1.1). Elliptical galaxies have a light profile shaped like an ellipse at optical wavelengths. Their shape ranges from almost spherical (designated as E0) to significantly elongated (designated as E6). Elliptical galaxies are found in various sizes, ranging from the largest to the smallest known galaxies. They lack spiral arms and contain far less interstellar gas and dust than spiral galaxies, with little or no star formation occurring within them. Their stars appear to wander erratically about the galactic centre. Spiral galaxies, on the

other hand, consist of a central bulge, a disc with spiral arms, a halo (designated 'normal spirals'), and a bar (designated 'barred spirals'). Galaxies that do not fall into either category are called irregular galaxies. These galaxies are small and lack coherent structure. They often form as a result of disturbances caused by the gravitational pull of neighbouring galaxies. Such interactions between nearby galaxies, which may eventually merge, might occasionally result in enhanced star formation, resulting in starburst galaxies. Starburst galaxies are those observed to be forming stars at an extremely rapid pace, which is about 10^3 times greater than in a normal galaxy. As a result of such high star formation rates, it is anticipated that the supply of gas and dust within the galaxy will run out within 10^8 years. This indicates that these episodes of extremely intense star formation occurred recently and will be halted in a matter of years.

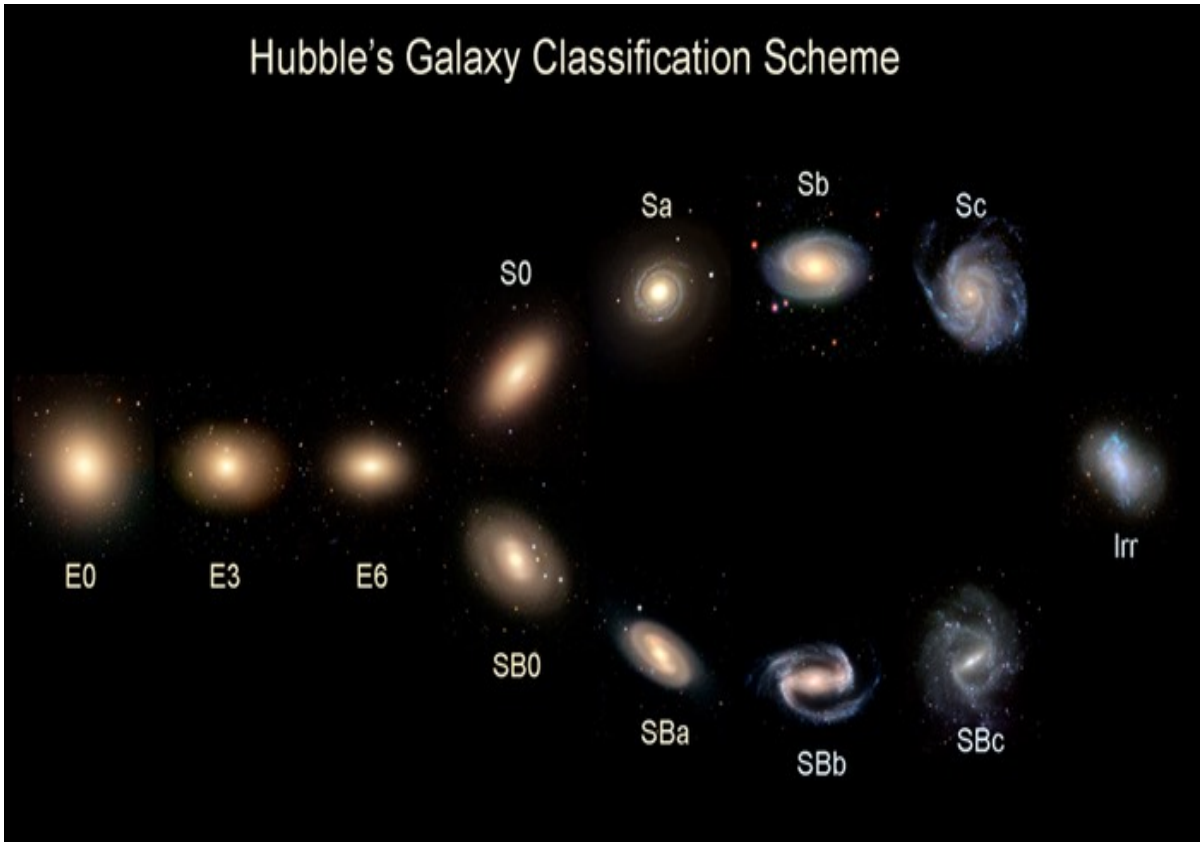

FIGURE 1.1: The Hubble tuning fork. The left of the image shows elliptical galaxies (spherical E0, to elongated E6). Additionally, lenticular galaxies (S0 and SB0) are visible in the image, where the B signifies that the central bulge is bar-shaped. After lenticular galaxies are spiral galaxies, split into 'normal' and 'barred'. The bulge becomes less prominent from the left to right of spiral galaxies as the spiral arms become increasingly open. The galaxy on the far right is classified as irregular; it has an unusual shape. Image retrieved from: http://astro.physics.uiowa.edu/ITU/labs/foundational-labs/classifying-galaxies/part-1-hubbles-tuning-fork.html

Normal and active galaxies are two types of galaxies that differ in the origin of their total energy output. The overall energy production of normal galaxies is the sum of star and interstellar gas emissions, principally at optical wavelengths. Normal galaxies' spectra are defined by stellar absorption and emission lines. On the other hand, active galaxies emit non-stellar radiation and account for a small fraction of galaxies. They have a compact nucleus (AGN) which produce high bolometric luminosities ranging from 10^{11} to 10^{15} $L_{\odot}$ compared to normal galaxies which have bolometric luminosities up to about 10^{11} $L_{\odot}$. At the centre of an active galaxy is a SMBH which accretes matter from the accretion disc. The processes of both black hole accretion and star formation are known to impact galaxy evolution. Based on the Madau and Dickinson (2014) diagram (Figure 1.2), both processes have similar trajectories across cosmic time, with a peak occurring at a redshift of 2. This indicates a co-evolution of black holes and their host galaxies. Several studies (e.g., Magorrian et al. 1998; Gebhardt et al. 2000; Ferrarese and Merritt 2000; Greene and Ho 2006; Kormendy and Ho 2013) have observed a tight correlation between the SMBH mass and the velocity dispersion of the host galaxy's bulge. This correlation suggests a strong connection between black hole formation and stellar bulge properties.

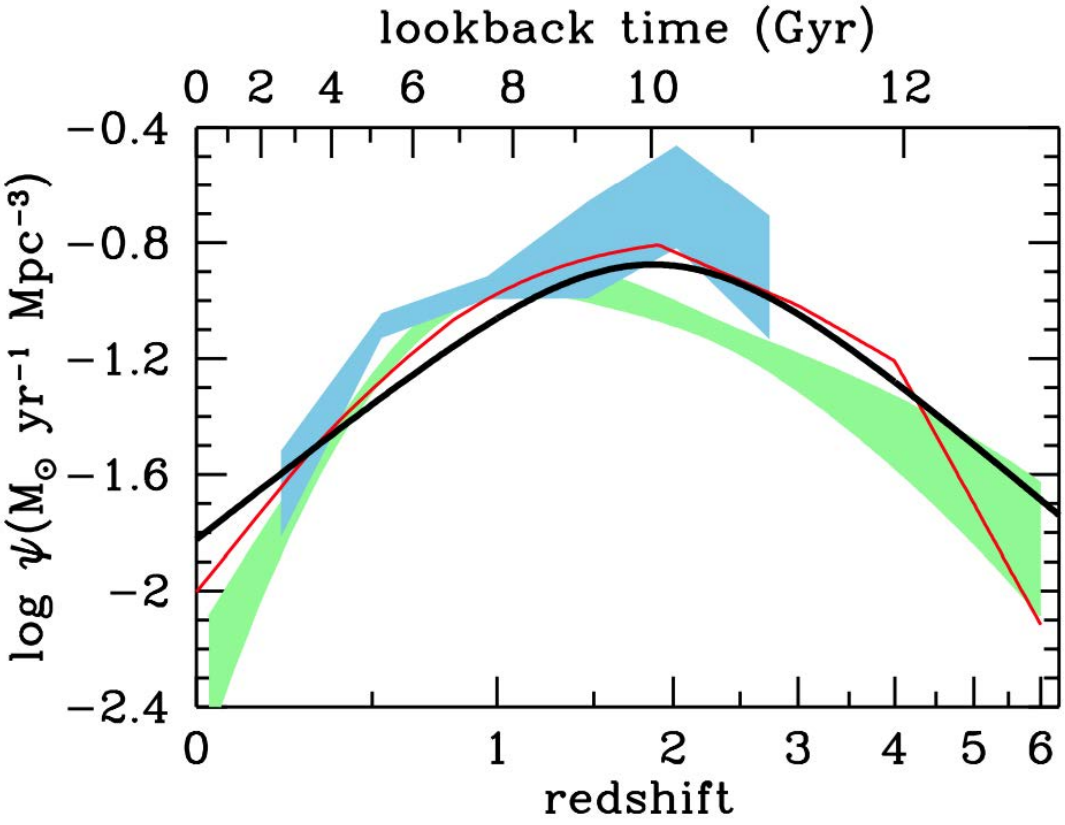

FIGURE 1.2: The cosmic evolution of star formation history (thick solid black line) compared with the black hole accretion history using data from X-ray (red line; Shankar, Weinberg, and Miralda-Escudé 2009, and light green shading; Aird et al. 2010) and infrared (light blue shading; García-Burillo et al. 2014) scaled by a factor of 3,300. Image and caption credit: Madau and Dickinson (2014)

1.2 Active Galactic Nuclei (AGN)

AGN are compact luminous regions at the centre of their host galaxy that radiate across the entire electromagnetic spectrum. AGN are thought to be driven by the material being accreted onto a SMBH at the galaxy's centre (Salpeter, 1964; Lynden-Bell, 1969). This process generates a powerful burst of radiation where the accretion disc's surrounding gas is photoionised. The physics and environments of these unusual galaxies have gradually gained interest in the realm of astrophysics and are currently among the most researched astronomical objects.

When orientation effects, different spin parameters (the ratio of the angular momentum of the black hole and its mass) and different accretion powers are taken into account, it is envisaged that a single unified model is able to characterise all AGN (Urry and Padovani, 1995). Figure 1.3 depicts the most generally adopted of these unified

models. This concept has a central *SMBH*, surrounded by an *accretion disc* that primarily emits X-ray, ultraviolet, and optical continuum emission. The *broad-line region* is near the black hole ($\sim 0.01 - 1$ pc distance), caused by clouds of fast-moving gas in the black hole's potential, producing strong optical and ultraviolet emission lines. This broad-line zone is obscured from some viewing angles by a dusty *torus* or distorted disc extending beyond the broad-line region. The dusty torus (at a distance of $\sim 0.1 - 10$ pc from the black hole) is a distribution of gas and dust, and it emits in the infrared wavelength band. The infrared emission comes from reprocessed ultraviolet radiation by high (often Compton thick) columns densities, which is re-radiated by torus dust. When the torus is in our line of sight, it obscures the optical emission from the central galaxy. Further out is the *narrow-line region* caused by slower-moving gas clouds. The last component in the AGN unified model is *radio jets* launched near the black hole along the direction of the disc spin axis, travelling often close to the speed of light. Thus the jet emission is strongly beamed in the direction of the jet motion, according to the theory of Special Relativity. Due to the multi-wavelength nature of AGN, studies spanning the electromagnetic spectrum, from radio to gamma rays, are required to gain a complete understanding of these objects.

The majority of AGN were previously classed as quasars or Seyfert galaxies based on the amount of radiation released by the central source. In Seyfert galaxies, the total energy emitted by the nuclear source at optical wavelengths is comparable to the galaxy's entire luminosity. The AGN in quasars can be so luminous that it outshines the host galaxy luminosity by orders of magnitude. Today, the definitions of the various classes have evolved to reflect the underlying physics rather than the way we see them. The presence of high-ionisation emission lines in the spectra, for example, identifies Seyfert galaxies. AGN are typically classified according to; (1) radio loudness into radio-loud (RL) or radio-quiet (RQ) classes; and (2) spectral characteristics into Type 0, 1, or 2 (see Table 1.1). The radio-loud or radio-quiet classification is mainly based on the ratio of radio (5 GHz) to optical (B band) flux density, where radio-loud AGNs have $F_5/F_B \geq 10$ while radio-quiet AGNs have $F_5/F_B \leq 10$ (Kellermann et al., 1989). Type 1 AGN have broad emission lines and a bright continuum in their spectra. In contrast, Type 2 AGN have narrow emission lines and a weak continuum. Based on the radio loudness and spectral characteristics, AGNs are classified into four categories; Seyfert galaxies, quasars, radio galaxies and blazars.

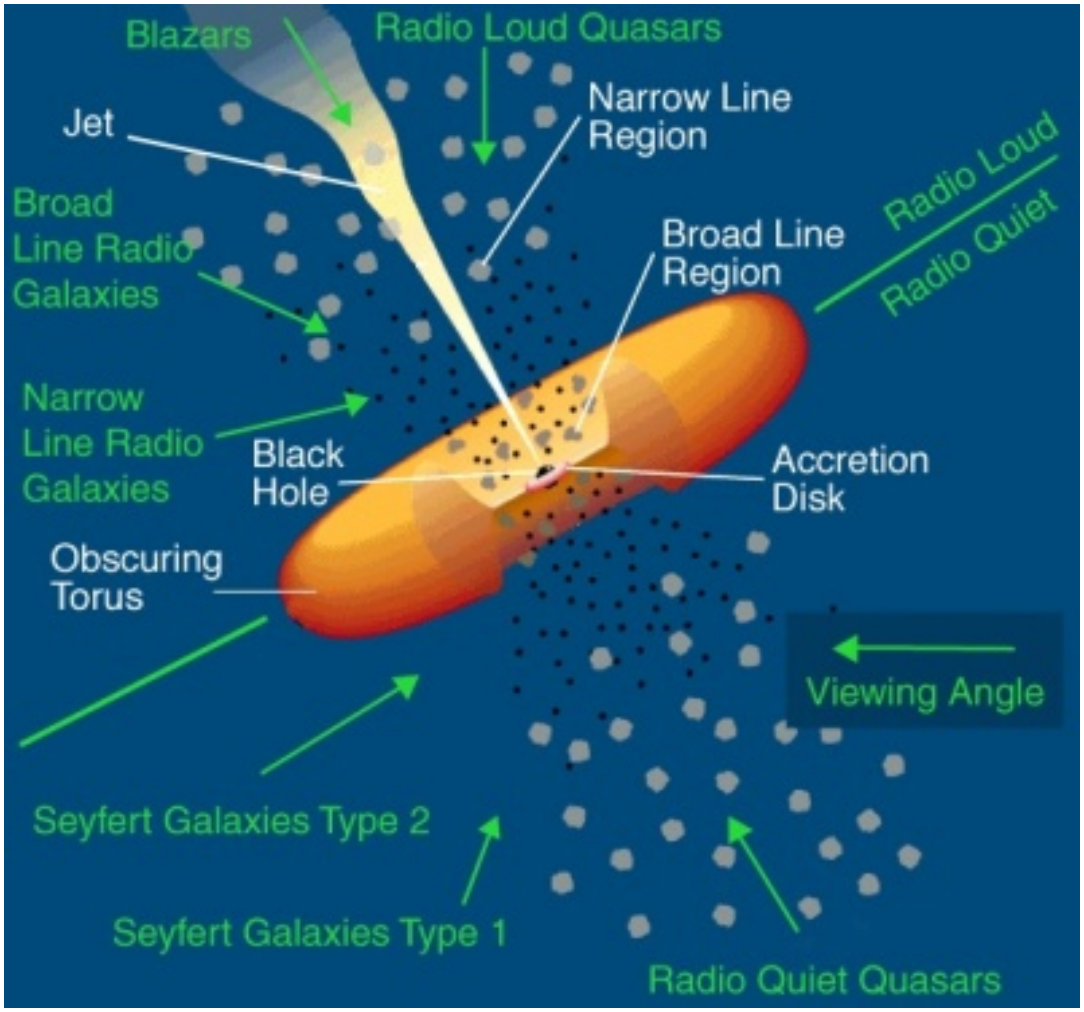

FIGURE 1.3: Schematic representation of an AGN. The AGN components are highlighted in white, and different classes of AGN are highlighted in green, with the green arrows indicating the observing angle of each AGN class. Image retrieved from https://saoastronews.wordpress.com/2015/04/18/magnetic-field-detection-in-an-active-galaxy-nucleus/ based on that of Urry and Padovani (1995)

TABLE 1.1: AGN classification based on radio loudness, optical spectrum and viewing angle. Table adopted from Urry and Padovani (1995)

Radio loudness	Optical emission line properties			
	Type 2 (Narrow Line)	Type 1 (Broad Line)	Type 0 (Unusual)	
Radio-quiet	Seyfert 2	Seyfert 1 QSO		Black hole spin? ↓
Radio-loud	NLRG { FR I, FR II	BLRG SSRQ FSRQ	Blazars { BL Lacs, FSRQ	
	Decreasing angle to line of sight →			

When the torus is observed edge-on, the SMBH, accretion disc and broad-line regions are obscured by the dusty torus. Thus, spectra reveal emission lines from the narrow region alone, as well as some infrared emission from the obscuring torus itself. Seyfert 2 and radio-loud narrow-line radio galaxies (NLRGs) are detected in this scenario. However, if the AGN is observed at an angle of $\sim$ 45 degrees from the torus, both narrow and broad-line regions are visible. In this case, the observed AGN classes are; Seyfert 1, radio-quiet quasars (QSO), radio-loud broad-line radio galaxies (BLRGs), and radio-loud quasars (steep spectrum radio quasars; SSRQs and flat spectrum radio quasars; FSRQs). Lastly, when the torus is observed face-on, we see the nucleus and jets. The jet's radiation travels at nearly the speed of light and can be beamed. The narrow and broad lines may be overshadowed by this emission, resulting in featureless spectra (Type 0 AGN). In this case, blazars are detected.

1.2.1 Seyfert galaxies

Seyfert galaxies were the first class of AGN discovered (Seyfert, 1943). They are radio-quiet AGN (RQ AGN) with a nuclear luminosity that is far lower than that of quasars, and they have a detectable host galaxy. At optical wavelengths, they are spiral galaxies with a bright core whose spectra is characterised by strong emission lines broader than typical velocities in normal galaxies. Seyfert galaxies are divided into Seyfert 1 and Seyfert 2 based on the observed emission lines in their spectra. In addition to the visible light emitted by their cores, Seyfert 1 are very bright emitters of ultraviolet and

X-rays emission. Their spectra exhibit two types of emission lines: narrow lines and broad lines. In contrast, the spectra of Seyfert 2 galaxies show narrow lines.

1.2.2 Quasars

Quasars (quasi-stellar-objects; QSO) are incredibly bright objects with unusual features, and they are often seen at high redshifts. With a relative width of $\Delta\lambda/\lambda \sim 0.03$, their spectra reveal strong emission lines that can be very broad. The line width is created by the gas having very high random velocities. Suppose the line width is interpreted as Doppler broadening caused by the superposition of lines of emitting gas with a very broad velocity distribution; we get velocities of around $\Delta v \sim 10000$ km/s. These objects' AGN are significantly brighter than the rest of the galaxy, making them seem virtually point-like on optical imaging. Astronomers were only able to discern structure in the optical emission of a large sample of quasars using the Hubble Space Telescope (HST) (Bahcall et al., 1997). Many characteristics of quasars are similar to those of Seyfert 1 galaxies, which have a bright nucleus and broad emission lines. As a result, quasars are thought to be among the most luminous members of AGN. Quasars have extraordinarily high total luminosities, with some radiating more than 1000 times the luminosity of our home galaxy, the Milky Way. Furthermore, this radiation must originate from a very tiny region, the size of which can be determined, for example, from the source's variability timescale. These and other characteristics lead to the conclusion that the central engine of active galaxies must be a SMBH.

1.2.3 Radio galaxies

Radio galaxies are radio-loud AGN (RL AGN) hosted by elliptical galaxies. They are the first class of AGN to have their optical counterpart identified in the early radio surveys (McMahon et al., 2002). Radio galaxies are characterised by a radio core, jets (on either one side or both sides of the host galaxy), lobes and hotspots. The radio core is the compact source at the centre of a radio galaxy. The position of this radio core coincides with the position of an identified optical/infrared host galaxy. The radio core is characterised by a flat radio spectrum ($\alpha > -0.5$), where $S \propto \nu^{\alpha}$. S is the integrated flux density at frequency ν and α is the spectral index. Radio lobes are characterised by a steep spectrum ($\alpha < -0.5$). The radio core emission has a flat spectrum due to the superposition of many synchrotron self-absorbed spectra from the base of the jet (Blandford and Königl, 1979). The lobes have steep spectra due to the predominant emission mechanism being optically-thin synchrotron (Blandford and Königl, 1979).

An example of a radio galaxy (a typical Fanaroff-Riley Type II; FR II) is shown in Figure 1.4.

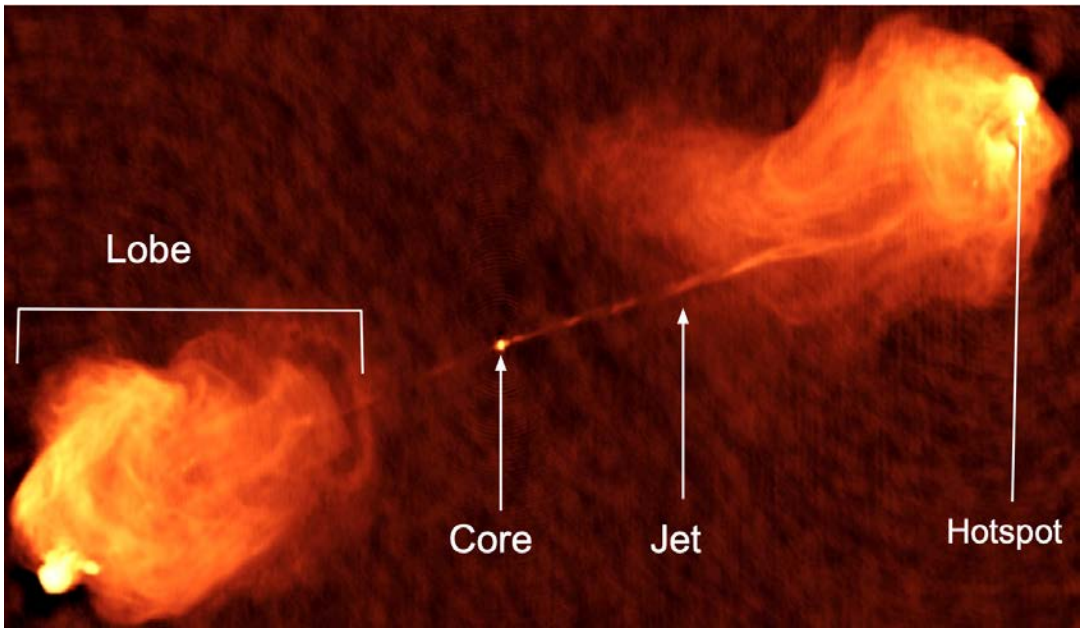

FIGURE 1.4: VLA 5 GHz intensity map of a radio galaxy, Cygnus A. The radio core, lobes and hotspots are visible in the image. Image credit: Carilli and Barthel (1996)

1.2.4 Blazars

Blazars represent the most extreme class of AGN, accounting for the vast majority of extragalactic gamma-ray sources. They are AGN with a relativistic jet directed very close to the line of sight, generating both synchrotron and inverse Compton gamma rays. Additionally, the jet's radiation travels at nearly the speed of light and is beamed. The narrow and broad lines may be overshadowed by this emission, resulting in a featureless spectra (Type 0 AGN). Blazars are variable radio sources, frequently enduring extreme brightness variations over short timescales from hours to days. Blazars are divided into two significant kinds based on the strength of their emission lines; FSRQs and BL Lac objects. BL Lac objects have spectra with no or very few emission lines. They are located at low redshifts. They were initially misidentified as variable stars until their spectra were analysed. Their name is derived from the variable-star designation given to the first object of this type to be investigated, BL Lacertae.

1.3 Morphological classification of radio sources

Radio galaxies exhibit various radio morphologies like compact, extended and complex morphologies. While machine learning algorithms (Aniyan and Thorat, 2017; Alhassan, Taylor, and Vaccari, 2018; Wu et al., 2018; Becker et al., 2021) and likelihood ratio approaches (Weston et al., 2018; Williams et al., 2019) are being developed for morphological classification and cross-identification respectively, visual inspection remains the most reliable technique for cross identifying radio sources with extended and complex morphologies. Visual inspection of radio galaxy morphology has been the most widely used traditional tool to classify extended radio galaxies (e.g. Fanaroff and Riley 1974; Banfield et al. 2015; White et al. 2020a; White et al. 2020b; Kondapally et al. 2021; Barkus et al. 2022). The morphological classification of galaxies is an approach based on grouping them by their visual appearance. By studying radio galaxies based on their morphology, astronomers can understand the formation and evolution of galaxies and their sub-components as a function of luminosity, environment, stellar mass and star formation rate over cosmic time.

1.3.1 Fanaroff & Riley classification scheme

Fanaroff and Riley (1974) divided radio galaxies into two classes according to the morphology of their radio structure. Fanaroff–Riley type I (FR I) radio galaxies are core-dominated sources with fainter lobes. FR II radio galaxies are edge-brightened sources with collimated jet and bright hotspots at the ends of the lobes. The criteria for classifying a source as FR I or FR II was based on the ratio of the distance between the brightest regions on opposing sides of the radio core to the total source extent from one end to the opposite. FR I sources have a ratio of less than 0.5 and FR II greater than 0.5. Fanaroff and Riley (1974) showed that there is a sharp division in luminosities ($L_{178MHz} \approx 2 \times 10^{25}$ W Hz^{-1}sr^{-1}) between the two classes (where FR II are more luminous than FR I). However, this FR I/ FR II break based on the radio power was recently questioned by Mingo et al. (2019). They deduced that at low flux densities, there is no association between radio morphology and radio power.

1.3.2 Commonly observed radio morphologies

1. **Head-tail and Wide-angle tail (WAT) radio galaxies**

   Head- and bent-tailed radio galaxies form a class of radio galaxies with distorted morphology. Usually, they are found in clusters, and their radio-emitting jets

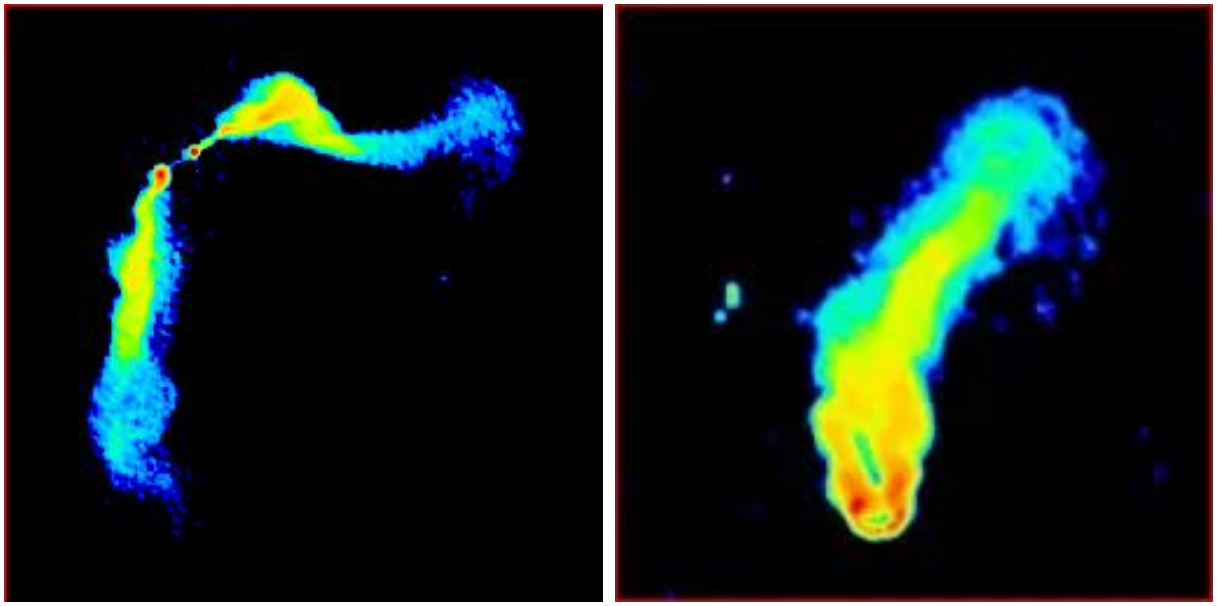

(A) 3C 465 (B) NGC 1265

FIGURE 1.5: Intensity maps of WAT radio galaxy (left panel; 3C 465) and NAT radio galaxy (right panel; NGC 1265). Both images are retrieved from https://blog.galaxyzoo.org/2014/01/16/more-information-on-tailed-radio-galaxies-part-1/

have been bent into a narrow 'U' and wide 'C' shape by ram pressure from the surrounding medium. These radio galaxies are generally referred to as narrow-angle tails (NAT) and wide-angle tails (WAT). WAT radio galaxies are characterised by a large angle between the radio jets and lobes (O'Donoghue, Eilek, and Owen, 1993), while NAT radio galaxies are characterised by a small angle between the jets and lobes (Bliton et al., 1998). The prototype of the WAT class is 3C 465 in A 2634 (Eilek et al. 1984; Figure 1.5A). The prototype of the NAT class is NGC 1265 (Figure 1.5B) in the Perseus cluster (O'Dea and Owen, 1986). Radio sources in the G4Jy subset (Section 3.1) with head-tail and WAT morphology are presented in Subsection 4.1.3.

2. **X-, S-/Z- shaped galaxies**

   Intriguing subclasses of radio galaxies with peculiar morphology are X-, S-/Z-shaped radio galaxies. These types of radio galaxies have a low surface brightness secondary lobes misaligned from the radio core in addition to the high surface brightness primary lobes (Ekers et al., 1978; Leahy and Parma, 1992). The secondary lobes are typically referred to as 'wings', and they are often more diffuse, still collimated and can be more extended analogue to the primary lobes. The X- or S-/Z-shaped morphology depends on the alignment of the secondary

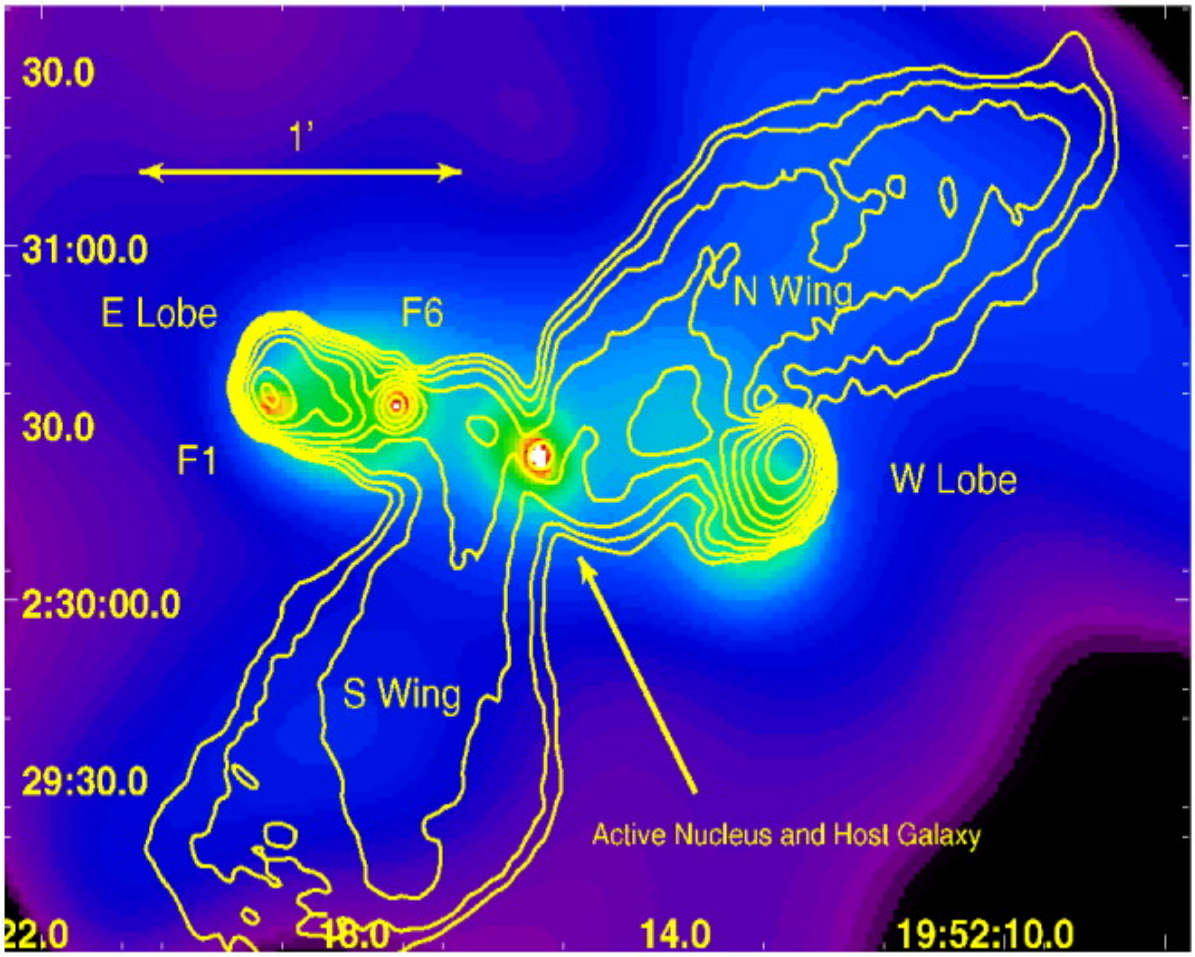

FIGURE 1.6: Overlay of 3C 403, an X-shaped radio galaxy, taken from Kraft et al. (2005). The 8.4 GHz radio contours from VLA are overlaid on an adaptively smoothed, exposure-corrected, background-subtracted Chandra ACIS-S image. The low surface brightness secondary lobes are aligned north-south (N lobe and S lobe), and the high surface brightness primary lobes are aligned east-west (E lobe and W lobe).

lobes with respect to the primary lobes. For S-/Z-shaped morphology, the secondary lobes emerge from the edge of the primary lobes. In contrast, for X-shaped morphology, the secondary lobes axis is nearly perpendicular to the axis of the primary lobes. Moreover, the wings of the X-shaped radio source are aligned close to the minor axis of the optical host galaxy, while the primary lobes are aligned close to the major axis of the elliptical host (Capetti et al., 2002; Joshi et al., 2019). An example of an X-shaped radio galaxy is 3C 403, shown in Figure 1.6. Radio galaxies with X- and S-/Z-shaped morphology are presented in Subsection 4.1.2.

While it is commonly accepted that the primary lobes are formed by the interaction of the jets with the surrounding medium, the origin of the secondary lobes

is still unclear. A variety of models have been developed to explain the origin of the wings (secondary lobes) in X-shaped radio galaxies. Several of these models are described below. However, it is essential to note that these models cannot explain the shape and properties of all X-shaped radio galaxies.

(a) *Backflow diversion model*:: In this model, the elliptical host galaxy's interstellar medium (ISM) plays a critical role in shaping the radio galaxy by exerting buoyancy pressure on the backflowing plasma within the primary lobes (Leahy and Williams, 1984; Worrall, Birkinshaw, and Cameron, 1995). Thus, the synchrotron plasma is redirected away from the lobe axis in the direction of rapidly decreasing ISM pressure. Therefore, X-shaped radio galaxies could serve as probes for studying how jets interact with their surrounding environment and how they are deflected.

(b) *Spin-flip model*: When a jet abruptly changes direction, it creates an X-shape structure. In this concept, the SMBH's axis of rotation, or "spin axis," changes orientation, causing the jet's direction to change (e.g. Dennett-Thorpe et al. 2002; Merritt and Ekers 2002; Gergely and Biermann 2009). The change in the jet's direction occurs when two galaxies merge. Thus their SMBHs spiral around each other and eventually merge too. The resulting merged SMBH has an axis of rotation different from that of the two SMBHs before the merger. If one of the SMBHs launches a jet along its spin axis before the merger, and the ensuing merged SMBH also launches a jet, the new jet will appear to change direction, resulting in the characteristic X-shape. As a result, the secondary lobes are a relic of the old jet (launched before the SMBH merger), while the interaction of the new jet with the surrounding medium forms the primary lobes. This model is particularly intriguing because it implies that X-shaped radio galaxies are related to gravitational waves (a natural result of the merger of two black holes). Furthermore, X-shaped radio emissions will serve as indicators of galaxy (and cluster) mergers.

(c) *Two unresolved AGN*: In this model, the low surface brightness secondary lobes (wings) occurs as a result of two pairs of jets launched from two unresolved AGNs where the radio jets have different directions (Lal and Rao, 2005). However, this model does not explain why the low surface brightness secondary lobes are aligned close to the minor axis of the elliptical host galaxy.

3. **Giant radio galaxies (GRGs)**

   GRGs form a subclass of radio galaxies initially defined to have a projected linear size of $\geq$ 1 Mpc, where $\Omega_m = 0.5$ and $H_0 = 50$ km/s/Mpc (Willis, Strom, and Wilson, 1974). The lower projected linear size limit is now 0.7 Mpc (Dabhade et al., 2020) assuming a Lambda CDM model with $\Omega_m = 0.31$ and $H_0 = 67.8$ km/s/Mpc (Planck Collaboration et al., 2016). Given their incredible megaparsec sizes, GRGs are among the largest known objects in the Universe, with the largest known GRG (to date) having a projected linear size of 4.69 Mpc (Machalski et al., 2008). Their incredible size makes them ideal candidates to study the large-scale structure of the Universe (Malarecki et al., 2015) and probe the warm-hot intergalactic medium (Safouris et al., 2009; Malarecki et al., 2013).

1.4 Motivation

AGN influence their host galaxy through thermal feedback linked with black hole accretion and kinematic feedback linked with relativistic radio jets. The overall impact of radio jets on their host galaxy is still a debatable matter. A study by Morganti et al. (2013) showed that radio jets might expel gas from a system resulting in the suppression of star formation. However, radio jets might trigger the collapse of molecular gas, promoting star formation (Croft et al., 2006). Furthermore, the jet production mechanism is still poorly understood, and the evolution of these sources with respect to redshift. This is due to the fact that comprehensive studies are typically restricted to the 173 'radio loud' active galaxies that make up the updated Third Cambridge Catalogue of Radio Sources (3CRR; Laing, Riley, and Longair 1983). With the goal of determining how the attributes of such sources change as a function of redshift and/or environment, White et al. (2020a) and White et al. (2020b) have assembled a sample (comprising 1,863 radio sources) that is more than ten times larger than the revised 3CRR catalogue. These radio sources have flux densities above 4 Jy at 151 MHz. They are selected at low radio frequencies with the Murchison Widefield Array (MWA; Tingay et al. 2013), which is the low-frequency precursor telescope for the Square Kilometre Array (SKA).

As the overall impact of radio jets is still unclear, a large sample of AGN with powerful jets is needed to provide robust statistics on the properties of these AGNs and to take into consideration the attributes such as the jet inclination with respect to the plane of the galaxy (García-Burillo et al., 2014), jet power (Mukherjee et al., 2016), and the molecular gas reservoirs' size (Emonts et al., 2011). The GLEAM (GaLactic and Extragalactic All-sky MWA) 4-Jy (G4Jy; White et al. 2020a; White et al. 2020b) is such

a catalogue. However, of 1,863 radio sources, 140 have an ambiguous host galaxy, or there are some discrepancies in the literature regarding the host galaxy (White et al., 2020b). As a result, the host galaxy of these radio sources could not be identified.

This project aims to identify galaxies hosting radio emission, as previous data have prevented this crucial step due to poor resolution (25 to 45 arcsec resolution). The host-galaxy identification is required in order to link the low-frequency radio data with other datasets, allowing us to construct a comprehensive, multi-wavelength perspective of the various processes occurring within these objects. The sample used comprises of 140 radio sources observed with MeerKAT (at 5 arcsec resolution). By combining radio data with mid-infrared data, we identify galaxies hosting their radio emission through visual inspection and literature checks.

1.5 Objectives

1. Create overlays comprising of radio data from different surveys overlaid on the mid-infrared images.
2. Visually inspect the overlays to (i) determine the radio morphology and (ii) identify the host galaxy.
3. Plot the positional offset between the host-galaxy position and the brightness-weighted centroid position.
4. Obtain redshifts (from literature) for sources with an identified host galaxy.
5. Calculate the integrated flux density, spectral indices, radio luminosity at 1.3 GHz and the linear size.

1.6 Thesis outline

The dissertation is outlined as follows. Chapter 2 describes the radio, mid-infrared and optical data I used to conduct this research. A brief overview of MeerKAT observations and data reduction is given. Chapter 3 outlines how the sample (G4Jy subset) was selected and the method used to classify the radio sources in this subset into their respective radio morphologies and identify their host galaxies. I also explain how these sources' properties (integrated flux density, spectral index and radio luminosity) are calculated. In Chapter 4, I present the main results of this research. I give comments on most of the sources. Chapter 5 discusses the results, and finally, a

summary of this work is given in Chapter 6.

Throughout this thesis, a Lambda-CDM model was assumed: $H_0 = 70\,\mathrm{km/s/Mpc}$, $\Omega_m = 0.3$ and $\Omega_\Lambda = 0.7$ (Planck Collaboration et al., 2016)

Chapter 2

Data/Observations

This chapter describes the MeerKAT observations (data reduction performed by Heywood 2020) and the primary surveys utilised to generate the overlays (Section 3.2) for the radio sources in the G4Jy subset (Section 3.1). The GLEAM survey allows us to explore the whole southern sky at frequencies below 300 MHz. This radio survey has broad spectral coverage and is sensitive to low-frequency diffuse radio emission. However, due to the inadequate spatial resolution ($\sim$ 2 arcmin) of MWA (Phase-I) data, other radio surveys (150 MHz and 843/1400 MHz) were required to analyse the radio morphologies of the G4Jy Sample (White et al., 2020a; White et al., 2020b). Nevertheless, even with higher-resolution images (25 arcsec resolution and 45 arcsec resolution), some G4Jy sources showed complex morphologies, making host galaxy identification difficult. As a result, this study used images from MeerKAT, with $\sim$ 7 arcsec resolution, to examine the radio morphology of the 140 G4Jy sources. Furthermore, we employed mid-infrared images and optical spectra. Mid-infrared images enable us to identify the host galaxy, even when the AGN is obscured by dust. Optical spectra enable us to determine the redshifts, which is used to calculate the properties of the host galaxy; physical sizes of the AGN and radio luminosities.

2.1 Radio data

2.1.1 MeerKAT observation

MeerKAT (Jonas and MeerKAT Team, 2016) is the SKA-Mid precursor telescope located 90 km from Carnarvon in the Northern Cape, South Africa. Radio interferometry comprised of 64 antennas that are 13.5 m in diameter. The telescope's objectives determine the configuration of the antennas. Centred in the core region of around 1 km in diameter are 48 antennas. Spread out in the outer region are 16 antennas which provide a maximum baseline of 8 km.

Of 140 sources from the G4Jy Sample, 138 sources were successfully observed (Project code: SCI-20190418-SW-01, PI: White) in June 2019 with the MeerKAT L-band (856 -

1712 MHz) receivers. Given the combination of the brightness of the G4Jy sources, together with the high sensitivity and (u,v) plane coverage of MeerKAT, the 5-minute snapshot observation per G4Jy target was adequate to achieve the two key objectives of unambiguous host-galaxy identification and morphological classification. Due to the G4Jy sources being distributed across the southern sky, these targets were observed in four blocks, grouped based on Right Ascension. Each block contained approximately 25% of non-target observational overheads. This overhead comprised scans of the primary calibrator (either PKS B1934−638 or PKS 0408−65, depending on the R.A.), an R.A.-dependent secondary calibrators (observed after every five target scans), the primary polarisation calibrator (either 3C 138 or 3C 286), and slewing time. The primary calibrator was used to solve for; the instrumental bandpass response (frequency-dependent gains), instrumental delays, and set the absolute flux scale. The secondary calibrators were used to solve for the time-dependent gains and provide additional delay corrections if the calibrator is brighter than 2 Jy at 1.3 GHz. Additionally, the secondary calibrators were used to set the astrometric reference frame. Calibration aims to counteract the effects of the instrument and/or local temporary conditions that may interfere with the scientific outcomes of the observation. The telescope correlator was set up to provide 8-second integrations and 4,096 frequency channels. The latter of which were averaged by a factor of 4 before processing.

The data were processed (by Heywood 2020) as follows. The KAT Data Access Library[1] was used to convert the raw MeerKAT visibilities for each of the four blocks to Measurement Set (MS) format. The low gain edges of the telescope's bandpass response were removed by applying the standard flagging commands to the targets. These commands were also employed to flag known regions of persistent RFI on interferometer spacings less than 600 m. After applying auto flagging software to the calibrator sources, instrumental delay, gain, and bandpass corrections were determined using the calibrators. After applying these corrections to the calibrators, the residual (corrected-model) visibilities were auto flagged again, and the instrumental corrections were re-derived and applied to the targets. The phase and delay self-calibration were performed using the multifrequency clean segment model derived from deconvolution within a masked region. Hereafter, the corrected data were re-imaged and primary beam corrected. Briggs 1995 robust value of 0.3 was used on most targets except for a few where uniform (robust = −2.0) weighting was used to increase angular resolution and eliminate residual sidelobe emission due to calibration errors. The use of a robust cleaning mask and a deep cleaning threshold within that mask means that the vast majority of the emission for each source is thoroughly

[1] https://github.com/ska-sa/katdal

deconvolved, and is therefore in the multi-frequency clean component models produced by WSCLEAN. The resulting MeerKAT images have a resolution of ~ 7 arcsec and a typical median rms of 0.078 mJy/beam.

The self-calibrated data were additionally re-imaged in eight frequency chunks, with the data on spacings less than 164 wavelengths removed from the (u,v) plane's inner region. The resulting cube was utilised to generate a spectral-index map for each source. This was accomplished by masking all pixels with a Stokes I brightness of less than 1 mJy/beam, then extracting the spectrum of each sightline through the cube and fitting for its slope in log-brightness vs log-frequency space. During the construction of the spectral index maps the differing resolutions of the sub-bands is alleviated by convolving the clean component models with a consistent restoring beam. Note also that the 1 mJy threshold simply uses the full band, Stokes I brightness to define a spatial region, and does not represent a brightness cut off in the components that are included in the spectral index calculation.

The CASA (McMullin et al., 2007) and TRICOLOUR[2] packages were used for flagging. The CASA package was used for referenced calibration, while the CUBICAL (Kenyon et al., 2018) software was utilised for self-calibration. The WSCLEAN (Offringa et al., 2014) software was used for all imaging. The EIDOS (Asad et al., 2021) package was used to perform primary beam correction in the image plane, utilising an azimuthally averaged image of the Stokes I primary beam, evaluated at the band centre frequency 1284 MHz. The data processing scripts (available online[3]) can be consulted for further information on data reduction process. Furthermore, these scripts were used to deploy the data processing jobs across the two supercomputers we used, specifically the ilifu[4] cloud computing facility and the Centre for High-Performance Computing (CHPC[5]) *Lengau* cluster.

2.1.2 GLEAM

MWA is one of the three SKA precursor telescopes located at the Murchison Radio-Astronomy Observatory in Western Australia. The site was chosen because of its extraordinarily low levels of radio frequency interference (RFI). The MWA is made up of 128 aperture arrays (tiles) spread out over an area that is approximately 2.5 km in diameter. Around 40% of the tiles are located in the central core, and the remaining

[2] https://github.com/ska-sa/tricolour/
[3] https://github.com/IanHeywood/oxkat
[4] http://www.ilifu.ac.za
[5] https://www.chpc.ac.za/

tiles are distributed for (u,v) coverage.

From August 2013 to July 2014, the MWA surveyed the southern sky (Declination, Dec. $< 30^{\circ}$, Galactic latitude, $|b| > 10^{\circ}$) at low radio frequencies (72 to 231 MHz) with a bandwidth of 30.72 MHz. These observations made up the GLEAM (Hurley-Walker et al., 2017) survey. The GLEAM Survey's resolution varies with declination and is roughly $2.5' \times 2.2'/\cos(\delta + 26.7^{\circ})$, where δ is the declination, at the central frequency of 154 MHz. This study employs 200 MHz images from the GLEAM survey with a resolution of ~ 2 arcmin for visual inspection. For Dec. $< 30^{\circ}$ and $|b| > 10^{\circ}$, the GLEAM survey cover 24,381 square degrees. Above a 5σ (50 mJy) threshold, the survey is 99.97% reliable, 90% complete at 170 mJy, and 50% complete at 55 mJy.

2.1.3 TGSS

The Giant Metrewave Radio Telescope (GMRT; Swarup 1991), located 80 km north of Pune, India, comprises 30 stationary parabolic antennas, 45 m in diameter. Fourteen of these antennas are arranged in a compact configuration and the remaining in a Y-shaped configuration. This configuration corresponds to the minimum and maximum GMRT baseline of 25 km and 100 km, respectively. Six high-performance feeds are installed on each antenna, covering the frequency range of 150 to 1500 MHz.

GMRT observed the sky at 150 MHz frequency in the declination range -55° to $+90^{\circ}$. These observations were carried out from April 2010 to March 2012, and they make up the Tata Institute of Fundamental Research (TIFR) GMRT Sky Survey first alternative data release (TGSS ADR1). However, because of the inadequate quality of the data at low elevations, observations at Dec. $> -53^{\circ}$ were retained for ADR1, which I employ in this analysis. Additionally, this survey's coverage of the region 6.5h < R.A. < 9.5h, $25^{\circ} <$ Dec. $< 39^{\circ}$ (Intema et al., 2017) is insufficient. Hence, I use data that do not fall inside this region. This survey gives useful spatial information at low frequencies with a $25'' \times 25''/\cos(\delta - 19^{\circ})$ resolution thus complementing the MWA's broad frequency range and surface-brightness sensitivity. The survey has a 7σ threshold (5 mJy/beam) sensitivity limit and an astrometric precision of < 2 arcsec in R.A. and Dec.

2.1.4 SUMSS

The Molonglo Observatory Synthesis Telescope (MOST; Mills 1981; Robertson 1991) is a 1.6 km long cylindrical paraboloid reflector located near Canberra, Australia. In

1996-97, MOST was upgraded to give a 2.7° diameter field of view (Large et al., 1994; Bock, Large, and Sadler, 1999). This radio telescope observed the southern sky (Dec. $< -30°$ and $|b| > 10°$) at 843 MHz between 1997 and 2003 (Mauch et al., 2003; Murphy et al., 2007), creating the continuum survey; the Sydney University Molonglo Sky Survey (SUMSS). At Dec. $< 50°$, SUMSS has a sensitivity limit of 5σ (6 mJy/beam) and 10 mJy/beam at Dec. $> 50°$. The observed astrometric accuracy for sources brighter than 200 mJy at 843 MHz is 1-2 arcsec, while the highest positional error observed for the survey is 30 arcsec. The NRAO (National Radio Astronomy Observatory) VLA Sky Survey (NVSS; Condon et al. 1998) has a similar resolution and sensitivity to SUMSS. This study makes use of SUMSS images for GLEAM components at Dec. $\leq -39.5°$ and NVSS images for GLEAM components at Dec. $\geq 39.5°$.

2.1.5 NVSS

The Very Large Array (VLA; Thompson et al. 1980) is an imaging interferometer comprising 25 m 27 dishes located 50 miles west of Socorro, New Mexico - on the Plains of San Agustin. The arrays are arranged in a Y-shape, giving out four configurations:

- the A configuration - maximum dish separation of 36 km
- the B configuration - maximum dish separation of 10 km
- the C configuration - maximum dish separation of 3.6 km
- the D configuration - maximum dish separation of 1 km

From September 1993 to October 1996, VLA surveyed the northern sky above Dec. $> -40°$ (82% of the sky) at the frequency of 1.4 GHz (L band) using the D and DnC configurations. During the fourth quarter of 1997, additional observations were made to fill in small gaps in this coverage. These observations were compiled to make up the complete 1.4 GHz continuum survey, NVSS (Condon et al., 1998). This survey has a resolution of 45 arcsec and a sensitivity limit of 5σ (2.5 mJy/beam). The observed astrometric accuracy is less than 1 arcsec for sources brighter than 15 mJy.

2.2 Mid-infrared: AllWISE catalogue

The Wide-field Infrared Survey Explorer (WISE; Wright et al. 2010), a NASA medium-class explorer, was launched on 14 December 2009 and completed its first survey of the entire sky on 17 July 2010. This space-based mission mapped the whole sky at four infrared wavelength bands (W1, W2, W3, and W4) centred at wavelength 3.4, 4.6, 12, and 22 μm and have a corresponding angular resolution of 6.1, 6.4, 6.5, and

12.0 arcsec, respectively. As such, WISE is well suited for probing AGN activity and characterisation of host galaxies in systems where AGN activity is not the major emission source.

WISE's four bands make it an ideal tool for studying the stellar structure and interstellar processes in galaxies. The two shorter wavelength bands (W1 and W2) map the stellar mass distribution in galaxies, whereas the longer wavelength bands (W3 and W4) map warm dust emission and polycyclic aromatic hydrocarbon emission, both of which trace the current star formation activity. Further, WISE colours (W1 − W2 and W2 − W3) have been used to separate different astronomical objects (e.g., Wright et al. 2010; Mateos et al. 2012; Mingo et al. 2016), which occupy certain regions in the WISE colour-colour plot (Figure 2.1).

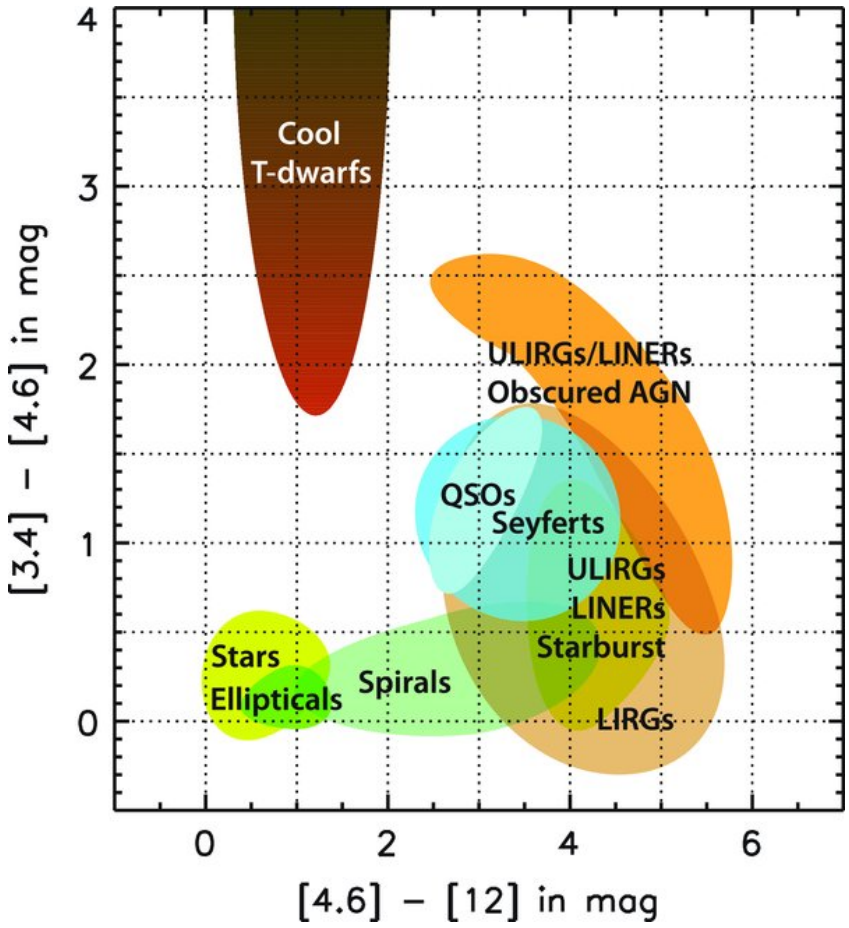

FIGURE 2.1: WISE colour-colour diagram adopted from Wright et al. (2010). This figure illustrates the different regions occupied by different astronomical objects where AGNs have W1 − W2 > 0.5. It is seen that different populations seem to overlap, except for brown dwarfs being isolated from the other groups.

This study employs 6.1 arcsec resolution images (W1 band: 3.4 μ) and AllWISE (Cutri

et al., 2013) positions for host galaxy identification, supplemented by radio contours from the surveys outlined in Section 2.1. The W1 band images are chosen as they have high resolution and better sensitivity analogue to W2, W3, and W4 images. AllWISE comprises data taken during the cryogenic and post-cryogenic phases of the survey, which were processed with improved calibration and reductions algorithms. Analogue to WISE, AllWISE has improved sensitivities of 0.054, 0.071, 0.73, and 5.0 mJy at the 5σ threshold and the positional inaccuracy of $\sim$ 1 arcsec.

2.3 Optical redshift survey: 6dFGS

The six-degree field galaxy survey (6dFGS) is a combination of redshift and peculiar velocities survey of galaxies in the southern sky (Dec. $< 0^{\circ}$, $|b| > 10^{\circ}$). From May 2001 to January 2006, 6dFGS was carried out with the UK Schmidt Telescope (UKST; Tritton 1978) at Siding Spring Observatory, utilising the 6dF multifibre spectrograph (Jones et al., 2004; Jones et al., 2005; Jones et al., 2006). The 6dF multifibre spectrograph uses 6.7 arcsec optical fibres and can record 150 simultaneous spectra over a 5.7-degree-diameter field. The 6dFGS spans a total area of 17 046 deg square, roughly ten times that of the 2dF Galaxy Redshift Survey (2dFGRS; Colless et al. 2001) and more than twice the region covered by the Sloan Digital Sky Survey seventh data release (SDSS DR7; Abazajian et al. 2009) in terms of spectroscopic coverage. The 6dFGS target sample was chosen from the Two Micron All Sky Survey (2MASS; Jarrett et al. 2000), where the K_s-band magnitude is less than 11.25 mag. Additionally, the target list was completed by selecting galaxies down to (H, J, r_f, b_j) = (13.05, 13.75, 15.6, 16.75). The use of near-infrared selection means that the primary sample provides a substantially unbiased (i.e. roughly mass-selected) survey of galaxies with old stellar populations in the nearby Universe. Furthermore, dust extinction has a minimal effect on near-infrared observations.

The primary goals of 6dFGS were to (i) improve our knowledge of the cosmography of the nearby Universe over the southern sky and (ii) to provide a sample of $\sim$10000 nearby early-type galaxies in order to study their intrinsic properties and to measure peculiar velocities via determination of Fundamental Plane distances. The 6dFGS has been useful in studies of luminosity and stellar mass function (Colless et al., 2007), large scale structure (Fleenor et al., 2005; Fleenor et al., 2006; Proust et al., 2006; Boué et al., 2008), and the influence of local density and velocity distribution (Erdoğdu et al., 2006a; Erdoğdu et al., 2006b). In this study, I use redshifts from this survey to calculate the radio luminosity and linear sizes of the G4Jy subset. The final data release of the

6dFGS comprises 179 263 objects and 117 405 distinct and credible redshifts with cz > 600 km/s. 6dFGS has a median redshift of 0.053.

Chapter 3

Methodology

3.1 Sample construction; the G4Jy subset

The sample for which we aim to identify the host galaxy of the radio emission is a subset of the G4Jy Sample. The G4Jy Sample comprises 1,863 brightest radio sources in the southern sky. Of 1,863 radio sources, 1,606 (86%) already have an identified host galaxy and are therefore assigned host flag 'i' in the G4Jy catalogue (White et al., 2020a; White et al., 2020b). However, 13 of these radio sources, with host flag 'i', had some discrepancies in the literature concerning the host galaxy. They were, therefore, part of the 140 G4Jy sources that were followed up using Open Time on MeerKAT. Among the remaining sources with no identified host galaxy in the G4Jy Sample, 129 radio sources (assigned host flag 'u') had an ambiguous identification. However, at the time of the MeerKAT proposal, there were 126 sources with the host flag 'u'. These 126 sources, together with 13 sources with host flag 'i' and G4Jy 1523 (host flag 'm'), all amounting to 140, were followed up with the Open Time on MeerKAT (PI: White) in June 2019. These radio sources had unusual morphologies evident in NVSS/SUMSS and/or TGSS, making it challenging to characterise their radio morphologies and identify their host galaxy. As a result, they were followed up with MeerKAT, which provides better sensitivity and high-resolution ($\sim$ 7 arcsec) images compared to TGSS (resolution of 25 arcsec) and NVSS/SUMSS (resolution 45 arcsec).

3.2 Overlays

In order to determine the radio morphology and identify the host galaxy of the G4Jy-subset sources, I created overlays for each radio source by writing a python script which uses the APLpy python package (Robitaille and Bressert, 2012). The overlays are $\sim$ 10 arcmin by 10 arcmin across and comprise radio data from four surveys (GLEAM, NVSS/SUMSS, TGSS and MeerKAT) overlaid on the mid-infrared WISE (W1 band) image. Out of the four bands from WISE, the W1 band has the best sensitivity and resolution; thus, we used W1 band images as our grayscale base for the

TABLE 3.1: A list of radio sources in the G4Jy subset for which White et al. (2020a) and White et al. (2020b) provided their host galaxy. However, because of the inconsistencies in the literature concerning the host galaxy, higher resolution data was required to confirm these host-galaxy identifications.

G4Jy name	GLEAM component names
G4Jy 40	GLEAM J002056−190853 and GLEAM J002112−191041
G4Jy 285	GLEAM J024103+084523 and GLEAM J024107+084452
G4Jy 333	GLEAM J031152−312959
G4Jy 570	GLEAM J054049−614233
G4Jy 717	GLEAM J083710−195152
G4Jy 747	GLEAM J090147−255516
G4Jy 917	GLEAM J112554−352321
G4Jy 1094	GLEAM J134855−252700
G4Jy 1205	GLEAM J145509−365543
G4Jy 1260	GLEAM J152659−135059
G4Jy 1537	GLEAM J192606−573954
G4Jy 1638	GLEAM J203444−354849
G4Jy 1741	GLEAM J215415−455319 and GLEAM J215435−454954

overlays. We chose mid-infrared images as the grayscale base for our overlays because they enable us to detect even the most dust-obscured host galaxies. This would not be achievable with optical images. Moreover, mid-infrared emission incorporates contributions from evolved stellar populations, avoiding the optical survey bias toward actively star-forming galaxies. Radio contours from GLEAM are indicated with red colour, NVSS/SUMSS contours are indicated with blue colour, TGSS contours are indicated with yellow colour, and contours from MeerKAT are indicated with purple colour (Figure 3.1). For each radio survey, the contours are $n \times \sigma$, where σ is the local rms and $n = 3, 6, 12, 24...$ and so on. However, for MeerKAT images in which artefacts are present, a higher cutoff threshold was applied to present comprehensible overlays. The local rms was calculated by taking the standard deviation of the image array (normally Gaussian distribution) where the following pixels were masked out. Pixel values at the faint end of the pixel histogram below the 2% percentile (outliers) were masked out to remove deep negatives. Pixels values at the positive end of the pixel histogram above the 80% percentile (poor man's source detection) were masked out to remove the positive tail.

Additionally, plotted in the overlays are beam sizes (GLEAM; red, NVSS/SUMSS; blue, TGSS; yellow and MeerKAT; purple), GLEAM positions (red square/s), NVSS/SUMSS

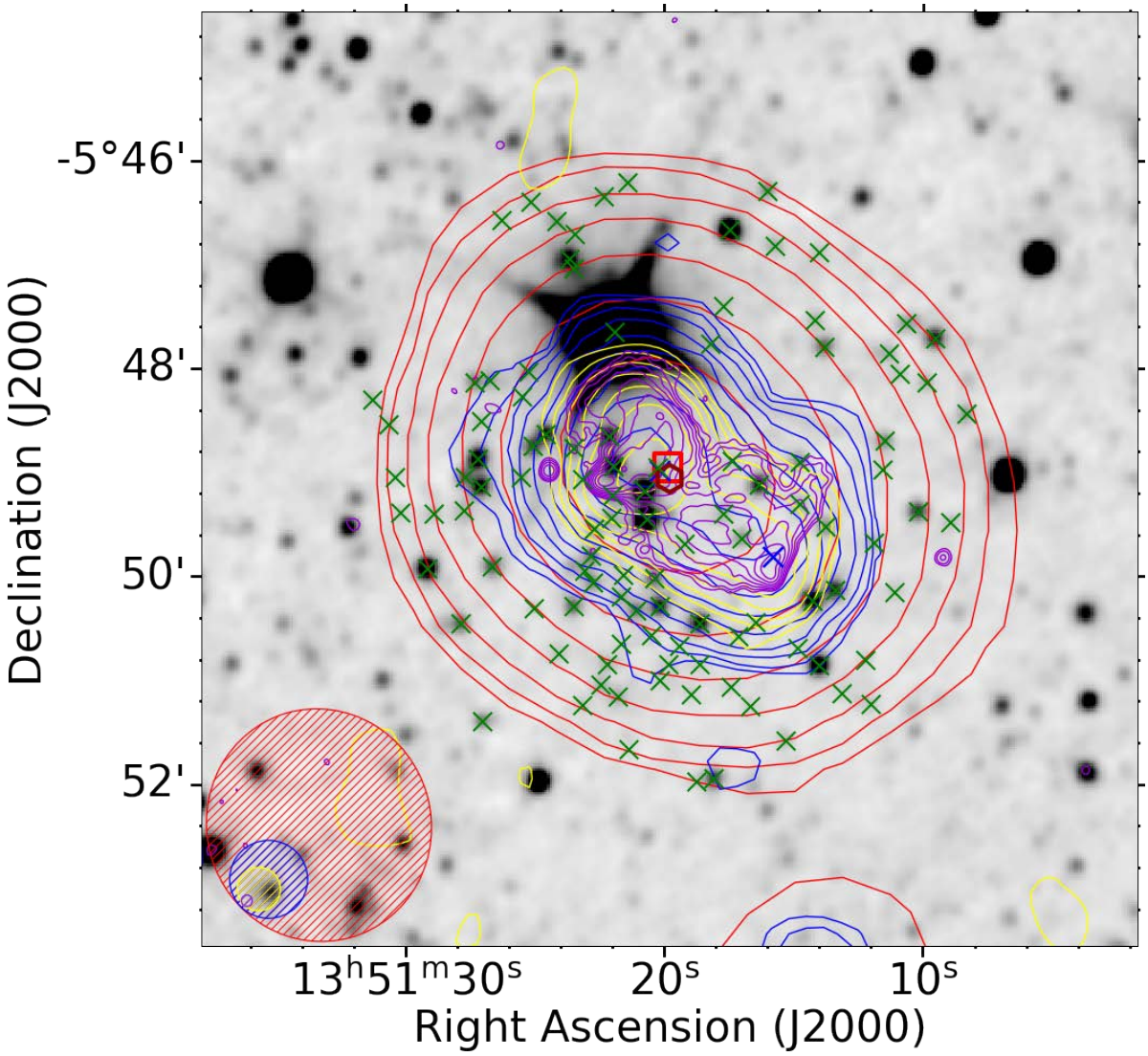

FIGURE 3.1: An example of a 10 by 10 arcmin overlay for G4Jy 1097.

positions (blue crosses), the brightness-weighted centroid position (cyan hexagon) and AllWISE positions (green crosses; 'x'). The beam information (major axis; BMAJ, minor axis; BMIN, and position angle; BPA) was obtained from the header of each FITS image. The GLEAM positions and brightness-weighted centroid positions were obtained from the G4Jy catalogue.

The GLEAM positions were obtained by running AEGEAN[1], the source finder algorithm, on GLEAM 'wide band' images (White et al., 2020a; White et al., 2020b). The output is the positions of the components detected above 5σ ($S_{200\,\mathrm{MHz}} \geq 50$ mJy). The brightness-weighted centroid position (Equation 3.1) was calculated for each source in the G4Jy Sample to enable the G4Jy Sample to be cross-matched with AllWISE to identify the host galaxy (White et al., 2020a; White et al., 2020b). The MWA beam has a typical resolution of $\sim$ 2 arcmin; thereby, some G4Jy sources are detected as multiple GLEAM components. In order to determine which components are associated with the same 'parent' source, NVSS and SUMSS data were exploited as they have better resolution than MWA. The centroid position ($\mathrm{Centroid_{RA}}$, $\mathrm{Centroid_{Dec}}$) was calculated by averaging the NVSS or SUMSS components, where the flux densities are taken as weights. The plot of the separation between the brightness-weighted centroid position and the host galaxy position is presented in Chapter 5.

$$\begin{aligned} \mathrm{Centroid_{RA}} &= \frac{\sum_{i=1}^{n} \mathrm{RA}_i F_i}{\sum_{i=1}^{n} F_i} \\ \mathrm{Centroid_{Dec}} &= \frac{\sum_{i=1}^{n} \mathrm{Dec}_i F_i}{\sum_{i=1}^{n} F_i} \end{aligned} \tag{3.1}$$

RA_i and Dec_i are the right ascension and declination of the ith component. F_i is the flux density of the ith component.

The AllWISE positions enable the position of the host galaxy to be pinpointed if detectable. For AllWISE positions, we cross-matched the G4Jy subset with the AllWISE catalogue within the radius of 3-arcmin using TOPCAT (Taylor 2005). The 3-arcmin search radius was chosen to enable even the host-galaxy identification for radio sources with complex morphologies like head-tail and bent-tail morphologies (Section 4.1.3). Radio sources with bent-tail morphology have their host galaxy near the apex of the radio emission. The host galaxy of head-tail radio sources is at the head of the radio emission rather than between the two distinct radio lobes.

[1] https://github.com/PaulHancock/Aegean

3.3 Radio morphology classification

Understanding the radio morphology of the radio source is crucial to identifying the host galaxy. In this study, we classify the radio morphology of the G4Jy subset into four categories based on the higher resolution images from MeerKAT:

- 'single' – the source has a typical compact morphology in the MeerKAT image,
- 'double' – the radio source has two distinct lobes in the MeerKAT image, but no radio core is detected, or the source has extended, elongated emission in the MeerKAT image that is suggestive of radio lobes,
- 'triple' – the source is resolved into three components (radio core and two lobes) in the MeerKAT image,
- 'complex' – the morphology of the radio source does not fall into the three categories listed above.

3.4 Host galaxy identification and flags

By analysing the radio morphology combined with the distribution of AllWISE sources, we can determine which galaxy is most likely to be the source of the radio emission. The host galaxy is most likely at the centre if the source has a single morphology. For sources with double morphology, the host galaxy is most likely positioned between the two radio lobes. However, if more than one AllWISE positions are on-axis, we leave the source unidentified since there is no detection of the radio core. We anticipate that the host galaxy will correspond with the position of the radio core for radio sources with triple morphology. Finally, for sources with complex morphology (not including head-tails), we are unable to provide a host galaxy. Following White et al. (2020a) and White et al. (2020b), we assign the following labels to each source in the G4Jy subset to signify the host flag:

- 'i'– the radio source has an identified host galaxy in the AllWISE catalogue or 2MASS,
- 'u'– due to the complexity of the radio morphology in the MeerKAT contours and/or the spatial distribution of AllWISE/2MASS sources, it is unclear which AllWISE/2MASS source is likely the host galaxy,
- 'm'– host-galaxy identification is restricted by the mid-infrared data in that the relevant source is not detected by AllWISE or 2MASS, or is obscured by nearby bright mid-infrared emission,

- 'n'– due to the type of radio emission concerned, no AllWISE/2MASS source should be indicated.

3.5 Integrated flux density at 1.3 GHz

Flux density is the radiation energy received per unit area and thus has units $\mathrm{Wm^{-2}Hz^{-1}}$. However, observed flux densities in radio are usually small and therefore are often expressed in Jansky (Jy) units, where 1 Jy $= 10^{-26}$ $\mathrm{Wm^{-2}Hz^{-1}}$. Of 140 G4Jy sources, 138 sources were successfully observed with MeerKAT. I used MeerKAT images to calculate (i) the integrated flux density at 1.3 GHz ($S_{\mathrm{int,\,1.3\ GHz}}$) for these 138 G4Jy sources, and (ii) the core intensity at 1.3 GHz ($S_{\mathrm{peak,\,1.3\ GHz}}$) for radio sources with an identified host galaxy in the G4Jy subset.

To obtain the integrated flux density at 1.3 GHz, I first created a polygon region (indicated with a black line in Figure 3.2) that follows the shape of the 3σ contour level using DS9 (Joye and Mandel, 2003) for each source in the G4Jy subset. However, we are interested in the pixels enclosed by the 3σ contour level. Therefore, the pixels between the DS9 region and the 3σ contour were masked out, thus leaving us with only pixels within the 3σ contour. I then sum the flux densities of the pixels within the region. This sum is in units of Jy/beam; therefore, it was divided by the beam area (Equation 3.2) to convert it into Jy units.

$$\text{Beam area} = \frac{\pi \mathrm{BMAJ} \times \mathrm{BMIN}}{4\ln(2)\,|\mathrm{CDELT1} \times \mathrm{CDELT2}|} \tag{3.2}$$

BMAJ and BMIN are the major and minor axis in degrees, and CDELT is the angular extent of a single pixel in degrees. These parameters were extracted from the FITS header of the MeerKAT image of each radio source in the G4Jy subset.

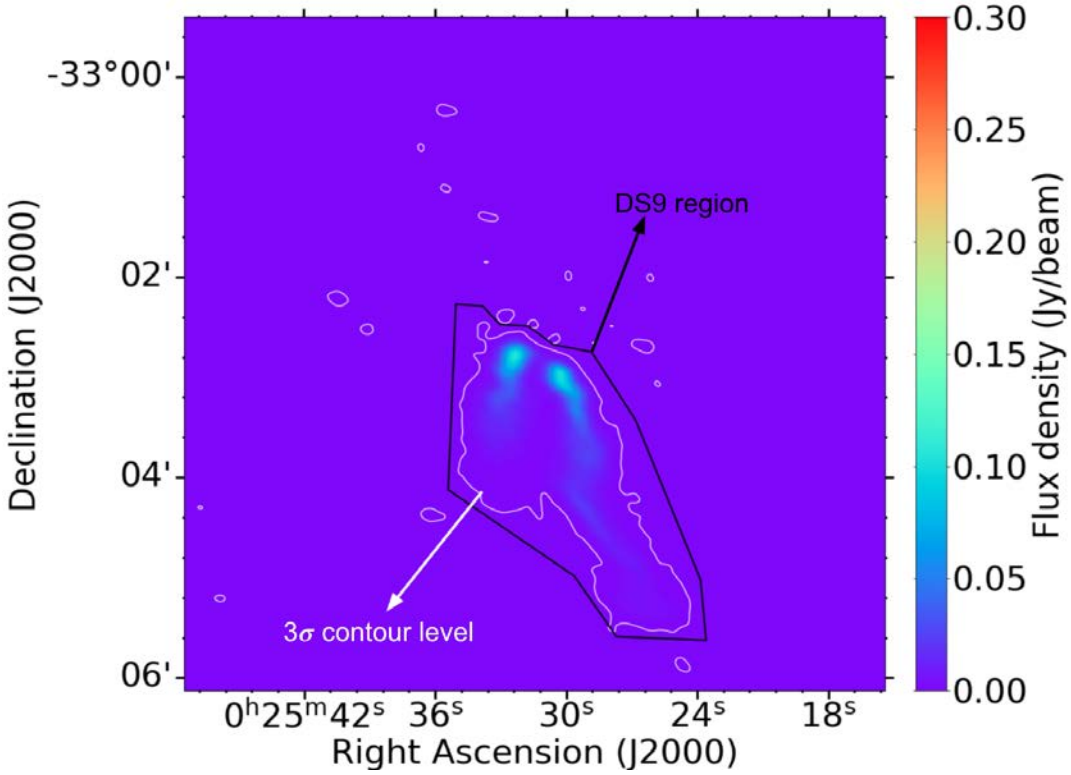

FIGURE 3.2: The 1.3 GHz intensity map of G4Jy 47. This image is to demonstrate which pixels were used to calculate the integrated flux density at 1.3 GHz. The black polygon region, created with DS9, follows the shape of the 3σ contour level (white region enclosed by the black region).

3.6 Spectral indices

The two-point spectral index between 151 MHz and 1300 MHz was calculated for sources in the G4Jy subset using equation 3.3:

$$\alpha_{\nu_1}^{\nu_2} = \frac{\log_{10}(S_{\nu_2}) - \log_{10}(S_{\nu_1})}{\log_{10}(\nu_2) - \log_{10}(\nu_1)} \tag{3.3}$$

where S_{ν_1} and S_{ν_2} are the integrated flux densities at $\nu_1 = 151$ MHz and $\nu_2 = 1300$ MHz, respectively.

Chapter 4

Results

The majority of the text in this chapter will be submitted to MNRAS.

The host galaxy identification of the radio sources in the G4Jy subset relies upon the $\sim$7 arcsec resolution images from MeerKAT as existing radio images (of 25 to 45 arcsec resolution) do not provide sufficient detail. With the sensitivity and resolution of MeerKAT, the 'complex' morphologies of these sources evident in NVSS/SUMSS and/or TGSS are resolved, enabling host galaxy identification for 98 radio sources out of 140. I identified the host galaxy of each source by visually inspecting the overlays and manually pinpointing the host galaxy. Of the 98 sources, 96 have a mid-infrared counterpart, where 4 (G4Jy 708, G4Jy 1523, G4Jy 1548 and G4Jy 1798) of 96 radio sources were identified using 2MASS images instead of WISE images. The host galaxy of G4Jy 1523 in AllWISE is affected by the nearby bright star, while the host galaxy of the other three sources is not detected in AllWISE. The remaining two sources, G4Jy 1371 and G4Jy 1540, have a host galaxy that is too faint to be detected by the mid-infrared surveys. However, their host galaxies are detected in the optical survey, Pan STARRS (Panoramic Survey Telescope and Rapid Response System; Chambers et al. 2019). Of the 140 G4Jy sources, 98 radio sources are assigned host flag 'i', 27 are assigned host flag 'u', 14 are assigned host flag 'm', and G4Jy 77 is assigned host flag 'n'.

Table 4.1 shows the morphological classification used (following White et al. (2020a) and White et al. (2020b)) and the number of sources in each category based on their host flag. Overall, 10 sources have 'single' morphology evident in the MeerKAT images, 79 have 'double' morphology, 34 have 'triple' morphology, and 15 have 'complex' morphology. Table 4.2 presents the findings of this study. In this chapter, I give comments on some of the sources in the G4Jy subset. The G4Jy subset sources with 'single' morphology and an identified host galaxy are presented in Appendix C. These radio sources have a compact morphology evident in all surveys. Sources with 'triple' morphology with typical symmetric lobes, evident in MeerKAT images, and have an identified host galaxy are presented in Appendix D. Appendix E presents sources with 'double' morphology with typical symmetric lobes and an identified host galaxy. Sources with no identified host galaxy and have 'double' morphology with typical symmetric lobes are presented in Appendix F. Appendix H presents sources with 'complex' morphology.

TABLE 4.1: The morphological classification and host galaxy flag statistics of the G4Jy subset based on the analysis of the overlays with the focus on MeerKAT contours and the distribution of AllWISE sources.

Morphology	Host flag				
	i	u	m	n	
Single	4		6		10
Double	53	18	8		79
Triple	34				34
Complex	6	8		1	15
	97	26	14	1	

TABLE 4.2: Properties of the sources in the G4Jy subset. Columns 1-3 are; G4Jy name, host flag, and the host galaxy name, Column 4 is the redshift and Column 5 is the redshift reference. Column 6 is the spectral index at 151 and 1300 MHz. Column 7 is the core intensity at 1300 MHz. This is the flux density extracted at the pixel value of the radio core position in the MeerKAT image. Columns 8-9 are the flux densities at 1300 MHz and 1400 MHz (obtained from the G4Jy catalogue), and Columns 10-11 are the radio luminosities at 1300 MHz and 1400 MHz. Columns 12-13 are the linear size and radio morphology label based on the visual inspection of the MeerKAT images.

G4Jy name	Host flag	Host galaxy	z	ref	$\alpha_{151\ \mathrm{MHz}}^{1300\ \mathrm{MHz}}$	$S_{\mathrm{core,1300\ MHz}}$ [mJy/beam]	$S_{1300\ \mathrm{MHz}}$ [Jy]	$S_{1400\ \mathrm{MHz}}$ [Jy]	$L_{1300\ \mathrm{MHz}}$ [W/Hz]	$L_{1400\ \mathrm{MHz}}$ [W/Hz]	Linear size [Mpc]	Morphology
G4Jy 14	i	AllWISE J000707.12+053609.6	0.216	(3)	−1.027	98.166	0.441 ± 0.085	0.806	6.05×10^{25}	1.11×10^{26}	0.563	Double
G4Jy 40	i	AllWISE J002107.53−191005.4	0.096	(1)	−0.627	0.230	1.261 ± 0.140	1.022	2.83×10^{25}	2.30×10^{25}	0.103	Triple
G4Jy 47	i	AllWISE J002531.45−330246.2	0.05	(1)	−0.815	0.424	1.527 ± 0.162	1.494	8.95×10^{24}	8.75×10^{24}	0.091	Double
G4Jy 77	n				−2.604		0.046 ± 0.027	0.035				Complex
G4Jy 84	i	AllWISE J004605.01−633319.2	0.075	(1)	−0.82	0.269	0.731 ± 0.100		9.94×10^{24}		0.215	Triple
G4Jy 95	u				−0.924		0.714 ± 0.090	0.668				Double
G4Jy 113	i	AllWISE J010241.76−215254.2	0.057	(1)	−1.811	2.172	0.215 ± 0.060	0.199	1.75×10^{24}	1.62×10^{24}	0.132	Double
G4Jy 120	i	AllWISE J010522.21−450517.2	0.71	(6)	−0.922	3.154	2.914 ± 0.221		6.28×10^{27}		1.004	Double
G4Jy 129	i	AllWISE J011141.93−685937.5			−0.812	0.274	2.027 ± 0.158					Triple
G4Jy 284	i	AllWISE J023926.84−112752.6			−0.884	4.072	0.656 ± 0.123	0.592				Double
G4Jy 285	i	AllWISE J024106.17+084416.9	0.021	(2)	−0.526	−0.084	1.346 ± 0.160	1.468	1.33×10^{24}	1.45×10^{24}	0.246	Triple
G4Jy 311	i	AllWISE J025552.77−202749.0			−0.798	0.919	1.182 ± 0.174	1.071				Double
G4Jy 318	i	AllWISE J030122.39−250445.1			−0.742	1.022	0.833 ± 0.148	0.77				Triple
G4Jy 328	i	AllWISE J030919.39−103844.5			−0.587	101.319	1.192 ± 0.168	1.131				Double
G4Jy 333	i	AllWISE J031154.01−313010.6	0.25	(5)	−0.628	−0.037	1.1 ± 0.171	1.052	1.92×10^{26}	1.84×10^{26}	0.416	Triple
G4Jy 338	u				−1.007		0.463 ± 0.110	0.484				Double
G4Jy 343	i	AllWISE J031744.12−550628.2	0.806	(4)	−0.88	15.237	0.656 ± 0.122		1.87×10^{27}		0.285	Triple
G4Jy 350	i	AllWISE J032259.32−881600.4			−0.857	12.729	1.524 ± 0.121					Double
G4Jy 365	i	AllWISE J033145.83−651754.2			−0.694	27.093	1.323 ± 0.161					Double
G4Jy 372	i	AllWISE J033801.08−572344.8			−1.02	153.245	0.748 ± 0.127					Double
G4Jy 375	m				−1.08		0.396 ± 0.088					Double
G4Jy 376	i	AllWISE J034046.51−340845.1			−0.894	0.080	0.669 ± 0.129	0.617				Triple
G4Jy 413	u				−0.839		0.766 ± 0.143	0.728				Double
G4Jy 441	u				−0.64		1.498 ± 0.156	1.36				Double
G4Jy 453	u											
G4Jy 456	i	AllWISE J042536.76+083217.7	1.1	(4)				1.314			0.651	
G4Jy 472	i	AllWISE J043309.35−534346.4			−0.951	2.222	0.613 ± 0.118					Triple
G4Jy 478	i	AllWISE J043539.49−494051.8			−0.839	1.836	0.777 ± 0.138					Double

Continued on next page

Table 4.2 – continued from previous page

G4Jy name	Host flag	Host galaxy	z	ref	$\alpha_{151\ \mathrm{MHz}}^{1300\ \mathrm{MHz}}$	$S_{\mathrm{core,1300\ MHz}}$ [mJy/beam]	$S_{1300\ \mathrm{MHz}}$ [Jy]	$S_{1400\ \mathrm{MHz}}$ [Jy]	$L_{1300\ \mathrm{MHz}}$ [W/Hz]	$L_{1400\ \mathrm{MHz}}$ [W/Hz]	Linear size [Mpc]	Morphology
G4Jy 488	i	AllWISE J044111.01+251839.6			−0.922	17.610	0.595 ± 0.087	0.716				Double
G4Jy 513	u				−0.692		2.85 ± 0.279	2.779				Complex
G4Jy 527	m				−0.64		1.215 ± 0.158	1.119				Double
G4Jy 526	i	AllWISE J051101.54−331600.8			−0.726	8.790	1.09 ± 0.175	0.998				Double
G4Jy 528	i	AllWISE J051104.82−131730.3	0.043	(1)	−0.786	9.890	0.959 ± 0.147	0.957	4.11×10^{24}	4.11×10^{24}	0.086	Triple
G4Jy 530	i	AllWISE J051247.41−482416.5	0.306	(4)	−0.807	−0.446	2.951 ± 0.267		8.46×10^{26}		0.496	Double
G4Jy 545	i	AllWISE J052615.97+114036.3			−0.864	0.233	1.014 ± 0.126	1.054				Double
G4Jy 548	i	AllWISE J052857.49+151905.3			−0.78	−0.026	1.317 ± 0.138	1.208				Triple
G4Jy 559	u				−0.722		1.561 ± 0.183					Double
G4Jy 566	m				−0.977		0.506 ± 0.082					Double
G4Jy 568	i	AllWISE J054016.90−330929.9	1.5	(4)	−0.957	0.125	0.609 ± 0.122	0.574	8.34×10^{27}	7.86×10^{27}	0.436	Triple
G4Jy 570	i	AllWISE J054050.82−614237.2	0.081	(6)	−0.748	7.425	0.89 ± 0.137		1.41×10^{25}		0.119	Double
G4Jy 573	i	AllWISE J054515.99−315859.1			−0.93	37.801	0.598 ± 0.120	0.54				Double
G4Jy 575	i	AllWISE J054617.91−172551.8			−0.728	377.901	1.137 ± 0.159	1.045				Double
G4Jy 587	u				−0.768		1.544 ± 0.178					Complex
G4Jy 601	i	AllWISE J061637.48−142049.2			−0.734	45.207	1.117 ± 0.157	0.991				Double
G4Jy 611	i	AllWISE J062620.46−534135.1	0.055	(1)	−0.855	28.387	7.43 ± 0.420		5.31×10^{25}		0.064	Double
G4Jy 623	i	AllWISE J063957.52−274542.5			−0.74	0.641	1.246 ± 0.188	1.182				Double
G4Jy 637	i	AllWISE J070129.05+231325.6	0.092	(2)	−0.782	43.508	1.064 ± 0.122	0.958	2.22×10^{25}	1.99×10^{25}	0.176	Triple
G4Jy 641	i	AllWISE J070532.94−451308.8			−0.876	1.760	0.835 ± 0.147					Triple
G4Jy 643	u				−0.626		1.058 ± 0.165					Double
G4Jy 652	i	AllWISE J071818.14−580834.4			−0.819	14.858	0.701 ± 0.130					Double
G4Jy 654	m				−0.845		0.66 ± 0.131	0.58				Single
G4Jy 665	i	AllWISE J073104.92−523808.6	0.09	(1)	−0.842	2.970	0.836 ± 0.145		1.67×10^{25}		0.226	Triple
G4Jy 671	i	AllWISE J074146.64−523415.9			−0.697	8.006	1.062 ± 0.162					Triple
G4Jy 672	i	AllWISE J074331.61−672625.5	1.51	(1)	−0.462	485.179	4.275 ± 0.307		3.77×10^{28}		0.212	Double
G4Jy 676	m				−0.847		0.907 ± 0.130					Single
G4Jy 677	i	AllWISE J075545.68+021029.0			−0.889	44.878	1.118 ± 0.149	1.008				Double
G4Jy 680	i	AllWISE J080236.28−095739.9	0.07	(1)	−0.679	0.253	2.555 ± 0.234	2.174	2.98×10^{25}	2.54×10^{25}	0.732	Triple
G4Jy 687	i	AllWISE J081158.15−052121.8			−0.868	6.275	0.787 ± 0.122	0.73				Triple
G4Jy 693	i	AllWISE J081611.74−703945.3	0.033	(1)	−0.581	0.328	1.466 ± 0.174		3.63×10^{24}		0.091	Triple
G4Jy 700	u				−0.819		2.409 ± 0.218	1.984				Complex
G4Jy 708	i	2MASS J08284359+2437221	0.083	(6)	−2.205	0.833	0.045 ± 0.024	0.647	8.45×10^{23}	1.22×10^{25}	0.129	Triple
G4Jy 717	i	AllWISE J083711.18−195156.6	1.032	(4)	−0.171	2471.810	5.161 ± 0.353	4.743	1.62×10^{28}	1.49×10^{28}	0.139	Single

Continued on next page

Table 4.2 – continued from previous page

G4Jy name	Host flag	Host galaxy	z	ref	$\alpha_{151\ \mathrm{MHz}}^{1300\ \mathrm{MHz}}$	$S_{\mathrm{core},1300\ \mathrm{MHz}}$ [mJy/beam]	$S_{1300\ \mathrm{MHz}}$ [Jy]	$S_{1400\ \mathrm{MHz}}$ [Jy]	$L_{1300\ \mathrm{MHz}}$ [W/Hz]	$L_{1400\ \mathrm{MHz}}$ [W/Hz]	Linear size [Mpc]	Morphology
G4Jy 730	i	AllWISE J085300.25−204730.7			−0.81	590.190	2.476 ± 0.241	2.292				Double
G4Jy 747	i	AllWISE J090147.26−255516.2	0.305	(4)	−0.732	333.058	6.489 ± 0.395	6.253	1.81×10^{27}	1.74×10^{27}	0.217	Double
G4Jy 758	i	AllWISE J091237.88−641130.6			−0.864	0.181	0.626 ± 0.116					Double
G4Jy 781	u				−0.915		0.587 ± 0.102	0.54				Double
G4Jy 869	i	AllWISE J104645.27−360138.5			−0.833	26.957	1.459 ± 0.162	1.32				Double
G4Jy 901	i	AllWISE J111119.43−403051.9			−0.699	253.768	1.27 ± 0.146					Double
G4Jy 917	i	AllWISE J112552.95−352340.3	0.033	(1)	−0.671	3.340	2.669 ± 0.203	2.606	6.63×10^{24}	6.48×10^{24}	0.068	Complex
G4Jy 935	u				−0.69		0.934 ± 0.122					Complex
G4Jy 939	u				−0.673		2.806 ± 0.195	2.571				Double
G4Jy 984	i	AllWISE J121738.77+033948.2	0.078	(3)	−0.834	44.599	1.306 ± 0.159	1.116	1.93×10^{25}	1.65×10^{25}	0.037	Complex
G4Jy 1067	i	AllWISE J132610.59−272538.6	0.044	(1)	−0.602	2.064	1.715 ± 0.223	1.595	7.65×10^{24}	7.12×10^{24}	0.148	Triple
G4Jy 1073	i	AllWISE J133225.71−330809.9	0.049	(2)	−0.768	1.474	1.553 ± 0.214	1.423	8.71×10^{24}	7.98×10^{24}	0.062	Triple
G4Jy 1094	i	AllWISE J134854.17−252724.5	0.126	(1)	−1.123	0.137	0.367 ± 0.103	0.329	1.55×10^{25}	1.39×10^{25}	0.175	Triple
G4Jy 1097	u				−0.643		1.076 ± 0.167	1.059				Double
G4Jy 1117	u				−2.004		0.105 ± 0.056	0.154				Complex
G4Jy 1190	i	AllWISE J144635.50−084605.3	0.071	(6)	−0.813	8.772	1.05 ± 0.169	0.956	1.27×10^{25}	1.16×10^{25}	0.092	Triple
G4Jy 1201	i	AllWISE J145422.82−192509.2			−0.779	90.105	1.157 ± 0.183	1.1				Double
G4Jy 1205	i	AllWISE J145509.61−365507.4	0.095	(1)	−0.773	2.128	1.319 ± 0.197	1.19	2.94×10^{25}	2.65×10^{25}	0.16	Triple
G4Jy 1220	u				−1.414		0.374 ± 0.087					Complex
G4Jy 1247	i	AllWISE J152132.67−400104.0			−1.146	1.752	0.497 ± 0.120					Triple
G4Jy 1260	i	AllWISE J152659.45−135100.0	1.687	(4)	−0.36	2482.420	2.991 ± 0.288	2.865	3.02×10^{28}	2.90×10^{28}	0.132	Single
G4Jy 1262	i	AllWISE J153014.29−423151.7	0.5	(6)	−0.934	4.687	5.797 ± 0.405		5.42×10^{27}		0.518	Double
G4Jy 1289	u				−0.833		2.13 ± 0.241	2.003				Double
G4Jy 1297	i	AllWISE J160240.38+154521.1	0.037	(2)	−0.718	0.205	0.928 ± 0.124	0.929	2.92×10^{24}	2.92×10^{24}	0.066	Double
G4Jy 1305	m				−0.875		0.69 ± 0.137	0.618				Single
G4Jy 1311	i	AllWISE J161338.86−771931.5	0.099	(6)	−0.702	−0.106	1.369 ± 0.165		3.30×10^{25}		0.13	Triple
G4Jy 1324	i	AllWISE J162035.89−710006.5			−0.899	6.835	0.975 ± 0.147					Triple
G4Jy 1329	m				−0.928		0.693 ± 0.142	0.593				Double
G4Jy 1342	i	AllWISE J163135.04−750905.9	0.11	(1)	−1.017	8.626	1.024 ± 0.145		3.19×10^{25}		0.137	Double
G4Jy 1362	u				−0.897		0.982 ± 0.164	0.898				Double
G4Jy 1365	i	AllWISE J164604.85−222804.6	0.799	(4)	−0.773	625.672	2.15 ± 0.243	1.994	5.65×10^{27}	5.24×10^{27}	0.107	Double
G4Jy 1371	i	PanSTARRS 108382532433733198			−0.664	1420.916	1.442 ± 0.179	1.329				Single
G4Jy 1377	i	AllWISE J165712.85−134909.5	0.124	(6)	−0.593	8.625	1.355 ± 0.190	1.311	5.20×10^{25}	5.03×10^{25}	0.146	Double
G4Jy 1403	i	AllWISE J172040.93−011157.2	0.029	(2)	−1.001	0.942	1.019 ± 0.149	0.761	1.97×10^{24}	1.47×10^{24}	0.058	Complex

Continued on next page

Table 4.2 – continued from previous page

G4Jy name	Host flag	Host galaxy	z	ref	$\alpha_{151\ \mathrm{MHz}}^{1300\ \mathrm{MHz}}$	$S_{\mathrm{core,1300\ MHz}}$ [mJy/beam]	$S_{1300\ \mathrm{MHz}}$ [Jy]	$S_{1400\ \mathrm{MHz}}$ [Jy]	$L_{1300\ \mathrm{MHz}}$ [W/Hz]	$L_{1400\ \mathrm{MHz}}$ [W/Hz]	Linear size [Mpc]	Morphology
G4Jy 1410	i	AllWISE J172437.79−024305.6	0.033	(1)	−0.519	8.876	1.877 ± 0.206	1.854	4.64×10^{24}	4.59×10^{24}	0.043	Double
G4Jy 1415	i	AllWISE J173122.25+210501.1			-0.844	−1.416	0.662 ± 0.099	0.653				Triple
G4Jy 1429	u				−0.618		2.162 ± 0.241					Double
G4Jy 1431	u				−0.787		1.027 ± 0.142	0.936				Double
G4Jy 1438	u				−0.956		0.766 ± 0.102	1.409				Complex
G4Jy 1444	u				−0.722		1.142 ± 0.169					Double
G4Jy 1449	m				−0.9		0.821 ± 0.125	0.717				Double
G4Jy 1450	i	AllWISE J175824.93+082826.9			−0.762	116.874	0.835 ± 0.126	0.756				Double
G4Jy 1452	i	AllWISE J175851.11−673829.0			−1.109	−0.297	0.637 ± 0.124					Double
G4Jy 1455	i	AllWISE J180117.98−662301.8	0.93	(6)	−0.697	285.146	2.1 ± 0.226		7.51×10^{27}		0.486	Single
G4Jy 1464	m				−0.814		1.038 ± 0.172					Double
G4Jy 1468	i	AllWISE J181231.40+262916.6			−0.93	40.300	1.183 ± 0.122	1.115				Double
G4Jy 1469	u				−1.006		0.652 ± 0.126					Double
G4Jy 1473	u				−1.132		0.39 ± 0.104					Complex
G4Jy 1474	m				−0.878		2.796 ± 0.289	2.711				Double
G4Jy 1491	m				−0.606		1.153 ± 0.186					Single
G4Jy 1493	m				−1.031		0.482 ± 0.077	0.422				Double
G4Jy 1494	u				−0.986		0.81 ± 0.142					Double
G4Jy 1501	i	AllWISE J184037.09−293353.9			−0.909	13.469	0.625 ± 0.138	0.745				Double
G4Jy 1503	i	AllWISE J184214.94−351753.9			−0.944	33.857	0.636 ± 0.139	0.629				Double
G4Jy 1518	i	AllWISE J191548.68−265257.4	0.226	(6)	−1.053	−5.869	1.608 ± 0.219	2.043	2.46×10^{26}	3.12×10^{26}	0.158	Double
G4Jy 1523	i	2MASS J19175722−2439053			−0.754	12.587	0.853 ± 0.159	0.836				Complex
G4Jy 1527	i	AllWISE J191947.64−525301.7	1.0	(4)	−1.002	0.546	0.47 ± 0.115		2.46×10^{27}		0.388	Triple
G4Jy 1534	u				−0.889		0.635 ± 0.137					Double
G4Jy 1537	i	AllWISE J192605.75−574016.4	0.061	(1)	−0.968	0.749	0.742 ± 0.140		6.62×10^{24}		0.166	Triple
G4Jy 1539	m				−0.678		1.111 ± 0.182	0.848				Single
G4Jy 1540	i	PanSTARRS 80412918521248951			−0.957	−0.058	0.607 ± 0.134	0.603				Double
G4Jy 1548	i	2MASS J19313531−1406009			−0.99	5.554	0.859 ± 0.157	1.226				Double
G4Jy 1553	u				−0.803		1.325 ± 0.199	1.262				Double
G4Jy 1554	i	AllWISE J193252.79−081803.4	0.101	(1)	−0.718	5.761	1.867 ± 0.227	1.85	4.71×10^{25}	4.66×10^{25}	0.167	Complex
G4Jy 1582	i	AllWISE J195230.53−011720.7	0.055	(1)	−0.684	3.249	2.007 ± 0.224	1.618	1.42×10^{25}	1.15×10^{25}	0.349	Double
G4Jy 1585	i	AllWISE J195513.78+015409.3			−0.853	55.181	0.787 ± 0.135	1.013				Double
G4Jy 1617	i	AllWISE J202338.06+170236.1			−0.649	0.037	1.221 ± 0.142	1.172				Triple
G4Jy 1638	i	AllWISE J203444.74−354901.7	0.089	(1)	−0.735	78.395	1.811 ± 0.229	1.717	3.50×10^{25}	3.32×10^{25}	0.04	Double

Continued on next page

Table 4.2 – continued from previous page

G4Jy name	Host flag	Host galaxy	z	ref	$\alpha^{1300\ \mathrm{MHz}}_{151\ \mathrm{MHz}}$	$S_{\mathrm{core,1300\ MHz}}$ [mJy/beam]	$S_{1300\ \mathrm{MHz}}$ [Jy]	$S_{1400\ \mathrm{MHz}}$ [Jy]	$L_{1300\ \mathrm{MHz}}$ [W/Hz]	$L_{1400\ \mathrm{MHz}}$ [W/Hz]	Linear size [Mpc]	Morphology
G4Jy 1663	m				-0.848		0.655 ± 0.136	0.598				Single
G4Jy 1697	i	AllWISE J212937.79−224824.4			-0.791	95.595	0.896 ± 0.157	0.833				Double
G4Jy 1706	i	AllWISE J213516.47−173433.4			-0.687	442.701	1.132 ± 0.174	1.06				Double
G4Jy 1740	i	AllWISE J215407.02−515012.8			-0.7	37.574	3.845 ± 0.322					Double
G4Jy 1741	i	AllWISE J215422.96−455231.3	0.145	(1)	-0.778	5.818	0.793 ± 0.148		4.35×10^{25}		0.882	Triple
G4Jy 1784	i	AllWISE J223746.49−114538.7	1.0	(4)	-0.878	124.113	1.191 ± 0.168	1.634	5.72×10^{27}	7.84×10^{27}	0.197	Double
G4Jy 1798	i	2MASS J22564194−4617351	0.08	(6)	-0.645	104.001	1.202 ± 0.174		1.85×10^{25}		0.087	Complex
G4Jy 1843	i	AllWISE J233510.30−663655.7		(7)	-0.69	4.332	2.472 ± 0.227					Double
G4Jy 1852	i	AllWISE J234745.06−280826.2	0.029	(1)	-1.853	2.041	0.098 ± 0.047	0.085	1.94×10^{23}	1.68×10^{23}	0.068	Double
G4Jy 1859	i	AllWISE J235706.20−022618.6	1.278	(3)	-0.839	-2.841	0.751 ± 0.116	0.767	6.30×10^{27}	6.44×10^{27}	0.491	Triple

Redshift references: (1) Jones et al. (2004), (2) Huchra et al. (2012), (3) Alam et al. (2015), (4) Flesch (2015), (5) de Jong et al. (2017), (6) NASA/IPAC Extragalactic Database (NED), and (7) SIMBAD

4.1 Radio sources with an identified host galaxy

Figure 4.1 is an overlay of G4Jy 40. The white "+" sign highlights the radio emission's host galaxy and the white diamond highlights the position of the 6dFGS counterpart, which implies that this source has a redshift in the 6dFGS catalogue. Overlaid on the grayscale WISE image are contours from GLEAM, NVSS/SUMSS, TGSS and MeerKAT with red, blue, yellow and purple colours, respectively. Plotted at the bottom left corner are the beam sizes of each survey.

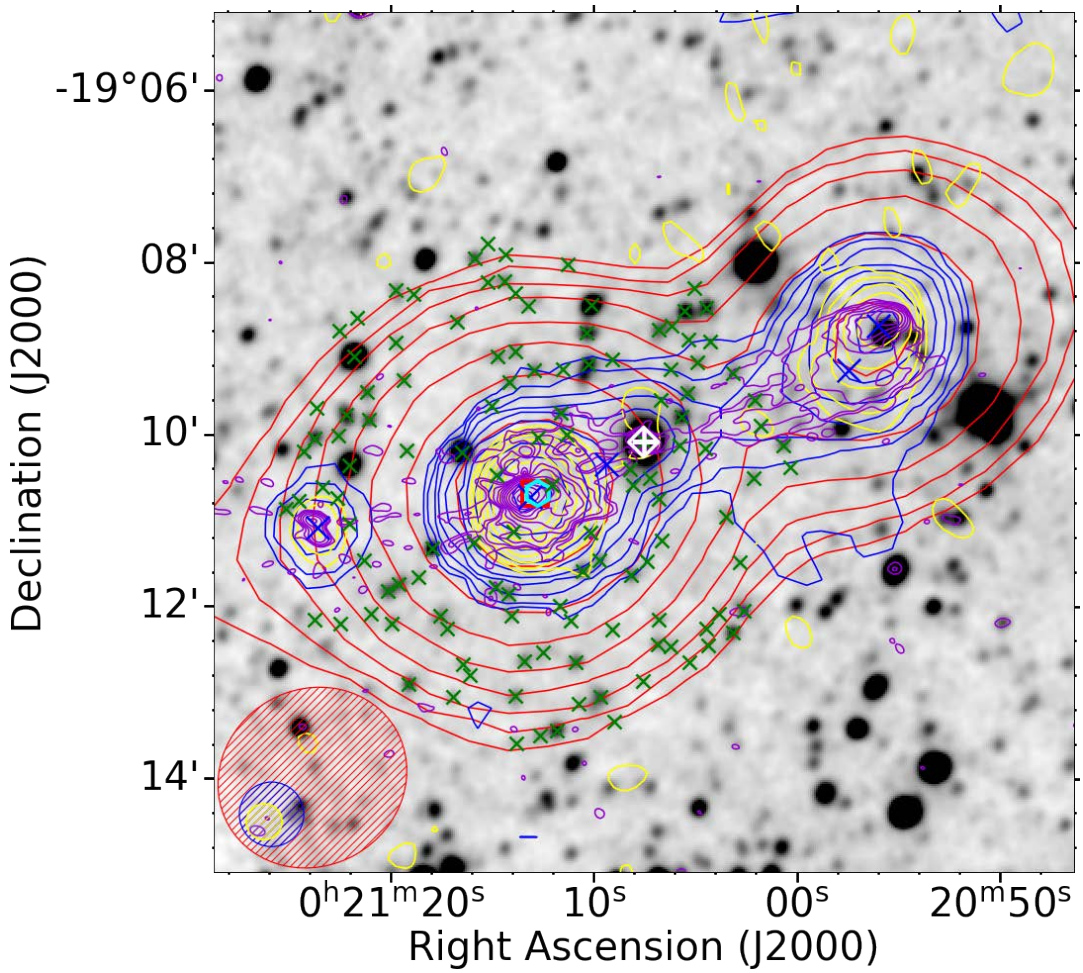

FIGURE 4.1: An overlay of G4Jy 40, centred at R.A. = 00:21:07.53, Dec. = -19:10:05.4. The radio contours are from GLEAM (170 - 231 MHz; red), NVSS (1.4 GHz; blue), TGSS (150 MHz; yellow) and MeerKAT (1.3 GHz; purple), overlaid on the inverted grayscale WISE (3.4 μm) image. The contour levels are $[3, 6, 12, 24, ..] \times \sigma$, where $\sigma =$ 0.087 mJy/beam, is the local rms. Shown in the bottom left corner is the beam size for each survey; GLEAM (red), NVSS (blue), TGSS (yellow) and MeerKAT (purple). The green crosses ('x') are the positions from AllWISE within 3 arcmin of the brightness-weighted centroid position (cyan hexagon), and the white '+' sign is the AllWISE position of the identified host galaxy for this source. The white diamond is the 6dFGS position, the red square is the GLEAM component position, and the blue crosses are positions of NVSS components.

4.1.1 Previous identifications

White et al. (2020b) and White et al. (2020a) provided the host galaxy for 13 (Figure 4.1, 4.2 and 4.4) of the 140 G4Jy radio sources. However, as these were 'borderline' identifications (with some accompanied by discrepancies in the literature), higher-resolution data was needed to confirm the host galaxy. With the MeerKAT follow-up images, we confirm the host galaxy of the 13 sources provided by White et al. (2020b) and White et al. (2020a).

G4Jy 40 (Figure 4.1): White et al., 2020b; White et al., 2020a inferred the host galaxy (AllWISE J002107.53−191005.4) of this radio source (with radio lobes GLEAM J002056−190853 and GLEAM J002112−191041) based on the interpretation of Nilsson (1998) that G4Jy 40 has a 'double' morphology with the largest angular size of 252 arcsec, using the radio map of Schilizzi and McAdam (1975). However, the 4.7 GHz image from Reid, Kronberg, and Perley (1999) reveals a radio source with 'triple' morphology that spans ∼160 arcsec from lobe to lobe. Due to the incorrect coordinates presented in the Reid, Kronberg, and Perley (1999) image, a higher resolution image with a large field-of-view needs to be used to confirm if GLEAM J002056−190853 is associated with G4Jy 40. The ∼ 7 arcsec resolution image from MeerKAT reveals a radio source with 'triple' morphology. The tight concentric contours at the centre (R.A. = 00:21:05.54, Dec. = −19:10:05.34) verify that AllWISE J002107.53−191005.4 (g002107.53−191005.4, $z = 0.096$) is the mid-infrared host galaxy of the extended emission, and GLEAM J002056−190853 and GLEAM J002112−191041 are the radio lobes, with flux densities of 0.919323 Jy and 4.862407 Jy at 151 MHz, respectively.

G4Jy 285 (GLEAM J024103+084523 and GLEAM J024107+084452; Figure 4.2A): The host galaxy of the extended radio emission of G4Jy 285, also known as NGC 1044 (4C +08.11), is AllWISE J024106.17+084416.9, also detected in 2MRS (J02410618+0844167, $z = 0.021$). This identification is in agreement with White et al. (2020b) and White et al. (2020a) and van Velzen et al. (2012). The radio source traces a zig-zag emission; however, it was unclear whether the low-frequency emission towards the north east (GLEAM J024133+084940) is associated with G4Jy 284 (White et al., 2020b; White et al., 2020a). We cannot confirm whether the radio emission is associated with G4Jy 284 as there is no detection of this emission in our 1.3 GHz image from MeerKAT. We only have a shallow 'snapshot' image. A longer observation time might reveal something.

G4Jy 333 (GLEAM J031152−312959; Figure 4.2B): MeerKAT contours reveal 'triple' morphology with edge-brightened lobes. We confirm that AllWISE J031154.01−313010.6 is the host galaxy. However, we find no redshift information in the literature.

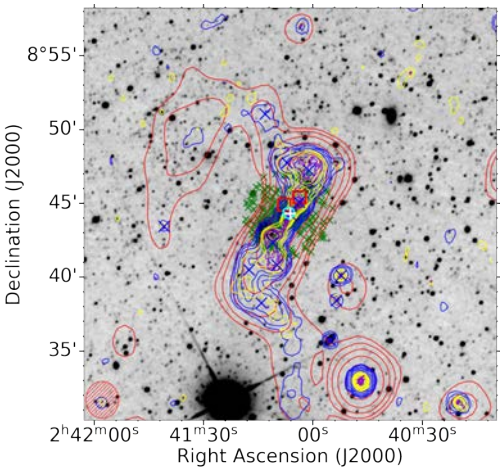

(A) G4Jy 285

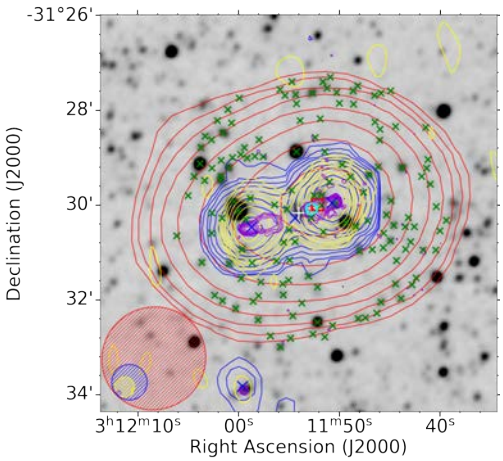

(B) G4Jy 333

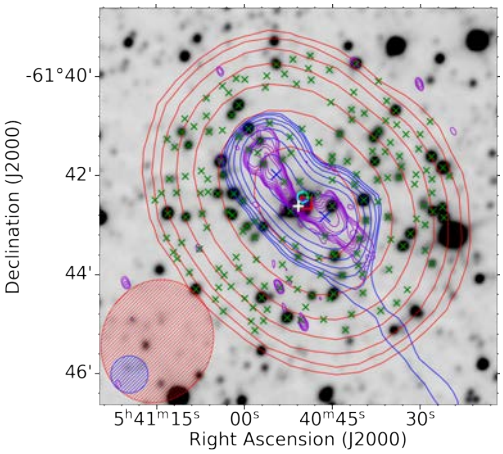

(C) G4Jy 570

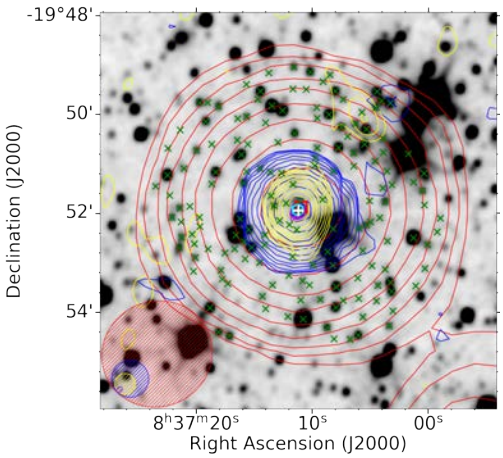

(D) G4Jy 717

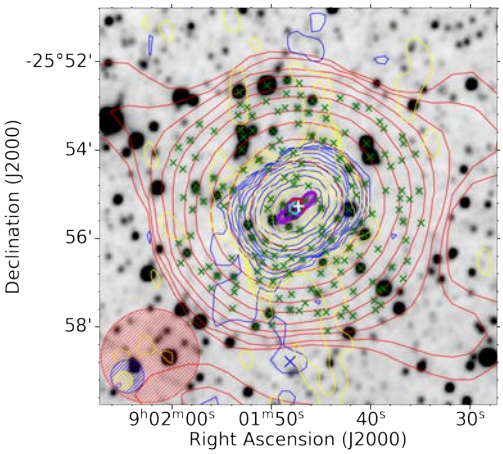

(E) G4Jy 747

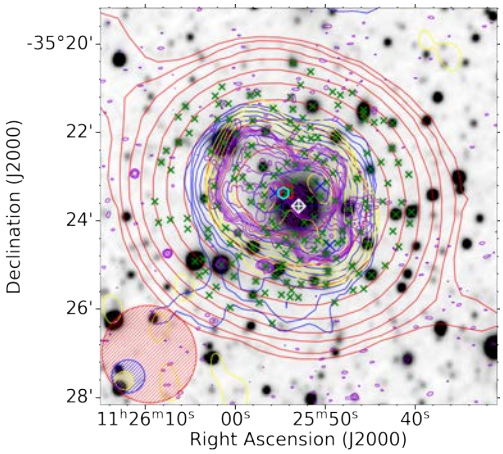

(F) G4Jy 917

FIGURE 4.2: Overlays for 6 of 13 sources in the G4Jy sample with debatable host galaxy. The datasets, symbols, beams and contours are the same as those described in Figure 4.1.

G4Jy 570 (GLEAM J054049−614233; Figure 4.2C): 'Double' extended morphology is evident in SUMSS and MeerKAT contours. This radio source (PKS B0540−617) is in cluster A3362. The host galaxy of this radio source is AllWISE J054050.82−614237.2 ($z = 0.081$) which agrees with White et al. (2020b) and White et al. (2020a) and the optical identification of Jones and McAdam (1992).

G4Jy 717 (GLEAM J083710−195152; Figure 4.2D): This radio source, known as PKS B0834−19, has a 'single' morphology evident in all surveys. We confirm that the host galaxy of this source is AllWISE J083711.18−195156.6 ($z = 1.032$), which agrees with the optical identification provided by Fugmann, Meisenheimer, and Roeser (1988) and di Serego Alighieri et al. (1994). We note the artefacts in the MeerKAT image, which result in an overestimated integrated flux density at 1.3 GHz. We, therefore, present an overlay where the lowest contour level has been adjusted to 48σ. G4Jy 717 has the flattest spectral index ($\alpha^{151\ MHz}_{1300\ MHz} = -0.17$) in the G4Jy subset.

G4Jy 747 (GLEAM J083710−195152, PKS 0859−25; Figure 4.2E): 'Double' extended radio morphology is evident in the MeerKAT contours. We confirm that AllWISE J090147.26−255516.2 ($z = 0.305$) is the host galaxy of the radio emission.

G4Jy 917 (GLEAM J112554−352321; Figure 4.2F): PKS B1123−315 is in the cluster AS 665. The higher resolution image from MeerKAT shows the distinct inner structure of this radio source where knots are evident in the eastwards jet (Figure 4.3). Furthermore, this jet is bent forming a right angle while the emission resulting from the westwards jet appears to be pushed towards south. The radio core is evident in the 1.3 GHz image from MeerKAT, which coincides with the position of the radio core from the 4.9 GHz image provided by Ekers et al. (1989). The host galaxy of the radio emission is AllWISE J112552.95−352340.3, which appears in 6dFGS (g1125529−352340, $z = 0.033$). This identification is in agreement with van Velzen et al. (2012), and a deeper MeerKAT image will be presented by Thorat et al. (in prep.).

G4Jy 1094 (GLEAM J134855−252700; Figure 4.4A): The WAT radio morphology is evident in the MeerKAT image. We confirm that the radio source is hosted by the mid-infrared AllWISE source J134854.17−252724.5, detected in 6dFGS at $z = 0.126$. This radio source is in the cluster Abell 1791, located at the centre (Slee, Perley, and Siegman, 1989).

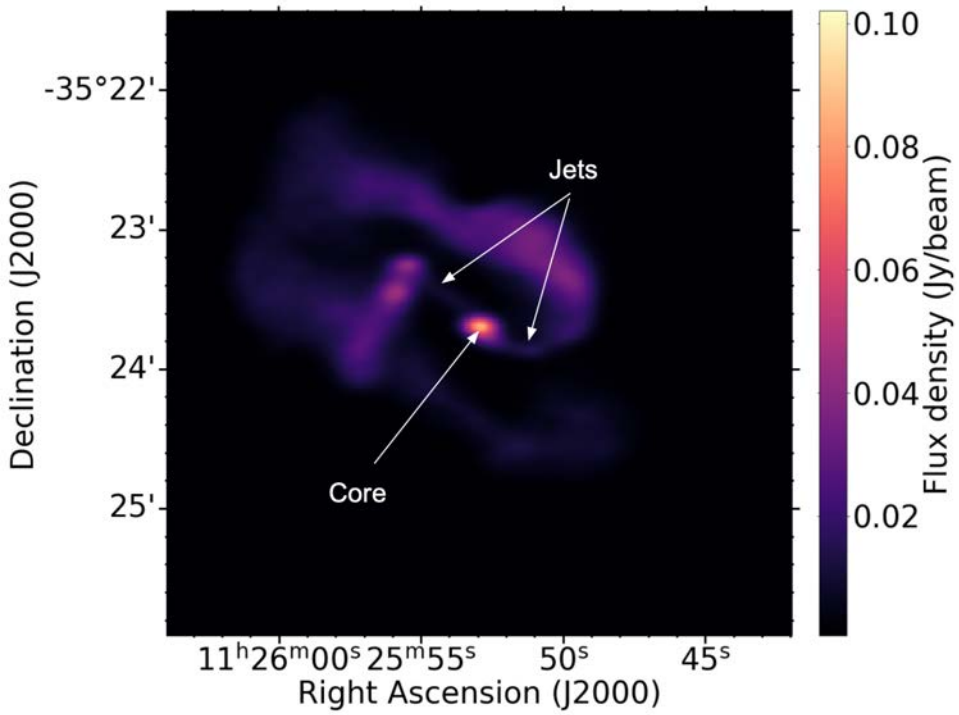

FIGURE 4.3: The 1.3 GHz intensity map of G4Jy 917. A radio source with unusual morphology at 1.3 GHz (resolution ~ 7)

G4Jy 1205 (GLEAM J145509−365543; Figure 4.4B): The radio source known as PKS B1452−367 has a 'triple' morphology with diffuse edges evident in MeerKAT contours. We confirm that the mid-infrared AllWISE J145509.61−365507.4 (g1455096−365508, $z = 0.095$) is the host galaxy.

G4Jy 1260 (GLEAM J152659−135059; Figure 4.4C): The radio source known as PKS B1526−136 has a 'single' morphology evident in all surveys. We confirm that the host galaxy is the mid-infrared AllWISE J152659.45−135100.0 at redshift $z = 1.687$. This radio-loud quasar has the highest redshift in the G4Jy subset (so far) and is one of the sources with a very flat spectral index ($\alpha^{151\ MHz}_{1300\ MHz} = -0.36$).

G4Jy 1537 (GLEAM J192606−573954, PKS B1921−577; Figure 4.4D): 'Triple' morphology is evident in the 1.3 GHz image from MeerKAT. We confirm that the mid-infrared AllWISE J192605.75−574016.4 (6dFGS g1926057−574017, $z = 0.061$) is the host galaxy of the WAT radio source.

G4Jy 1638 (GLEAM J203444−354849; Figure 4.4E): The head-tail radio morphology is evident in the 1.3 GHz image from MeerKAT. The corresponding host galaxy of the radio emission is AllWISE J203444.74−354901.7, appearing in 6dFGS as g2034447−354902 ($z = 0.089$).

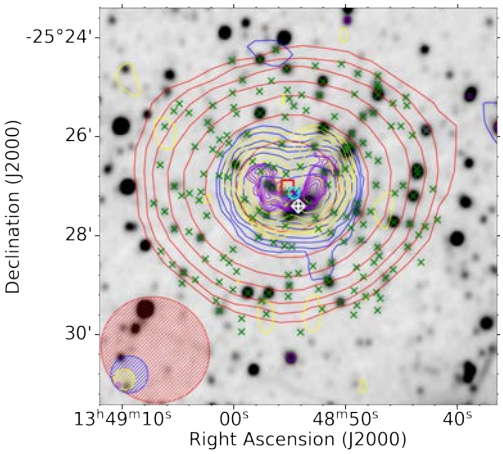

(A) G4Jy 1094

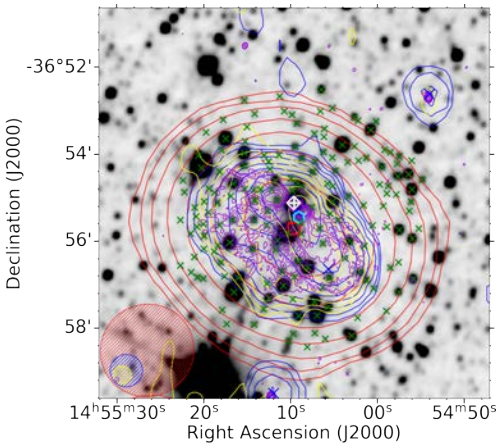

(B) G4Jy 1205

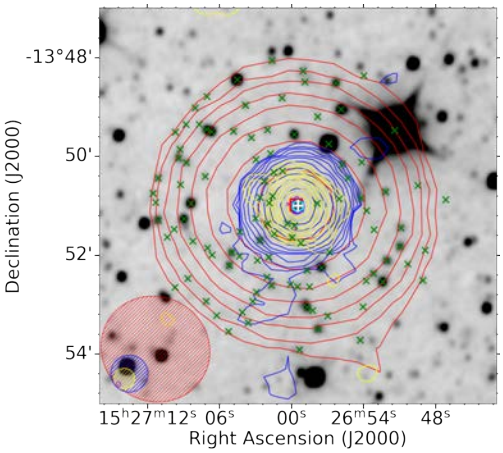

(C) G4Jy 1260

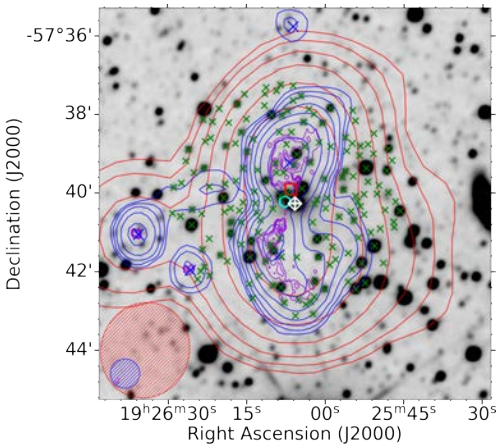

(D) G4Jy 1537

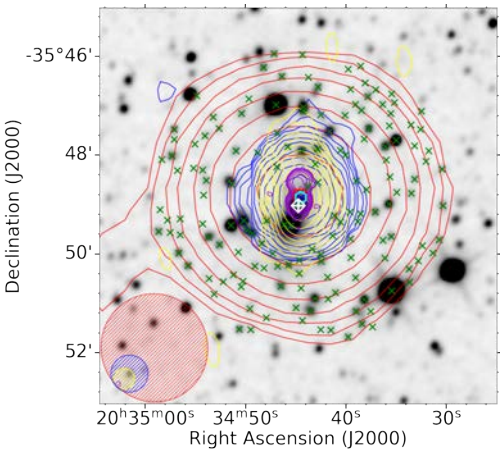

(E) G4Jy 1638

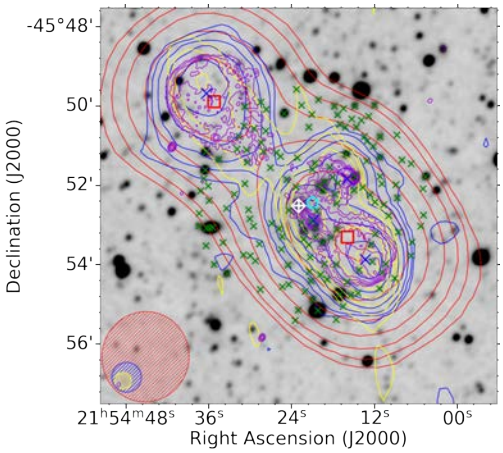

(F) G4Jy 1741

FIGURE 4.4: Overlays for 6 of 13 sources in G4Jy sample with debatable host galaxy. The datasets, symbols, beams and contours are the same as those described in Figure 4.1.

G4Jy 1741 (GLEAM J215415−455319 and GLEAM J215435−454954; Figure 4.4F): Edge-brightened radio lobes and a compact core are evident in the 1.3 GHz image from MeerKAT. We confirm that AllWISE J215422.96−455231.3 is the host galaxy of the 'triple' morphology radio source, detected in 6dFGS (g2154230−455232, $z = 0.145$).

4.1.2 Newly identified X- and S-/Z-shaped radio sources

Subclasses of radio galaxies with intriguing morphology are X- and S-/Z-shaped galaxies. These sources are characterised by a pair of primary lobes with high surface brightness and secondary lobes with low surface brightness. The secondary lobes in S-/Z- shaped galaxies emerge from the edges of primary lobes. In the G4Jy subset, 4 radio sources have an X-shaped morphology, and one source has an S-/Z-shaped morphology (Figure 4.5). The 1.3 GHz MeerKAT intensity maps of these sources are presented in Appendix A to illustrate the orientation of the low surface brightness secondary lobes with respect to the high surface brightness primary lobes.

G4Jy 284 (GLEAM J023926−112806; Figure 4.5A): A (borderline) X-shaped morphology, and the detection of the radio core, is evident in the MeerKAT contours. The mid-infrared source that coincides with the radio core is AllWISE J023926.84−112752.6. However, there is no redshift information in the literature for the host galaxy.

G4Jy 530 (GLEAM J051250−482358; PKS 0511−48; Figure 4.5B): For this radio source, Smith and Robertson (1985) reported an optical identification that matches AllWISE J051247.41−482416.5, classified as a Seyfert type 2 galaxy. However, White et al. (2020b) and White et al. (2020a) asserted that the radio map of Smith and Robertson (1985) is not of sufficient resolution to rule out the presence of another mid-infrared source on the axis connecting the radio lobes. The X-shape morphology evident in the MeerKAT contours support the optical identification of Smith and Robertson (1985), and we, therefore, identify AllWISE J051247.41−482416.5 as the host galaxy. The low surface brightness radio emission (secondary lobes) might be due to plasma backflow in the primary lobes.

G4Jy 1377 (GLEAM J165712−134911; Figure 4.5C): This radio source is known as PKS B1654−137. An X-shaped morphology is evident in the MeerKAT contours, with the primary lobes aligned northwest and southeast, while the secondary lobes are aligned northeast and southwest. The mid-infrared counterpart of this radio source is the AllWISE source, J165712.85−134909.5, at $z = 0.124$.

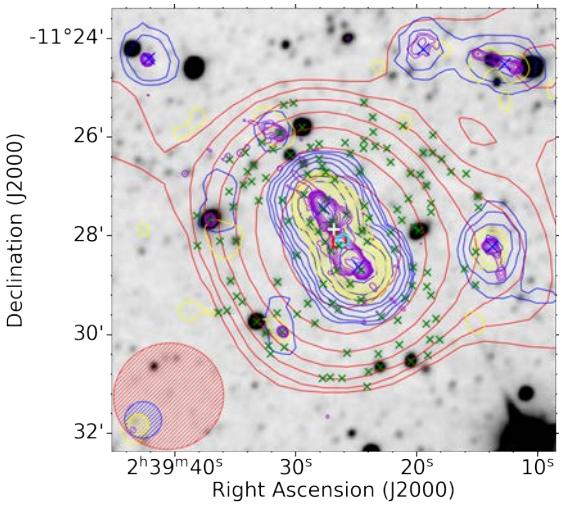

(A) G4Jy 284

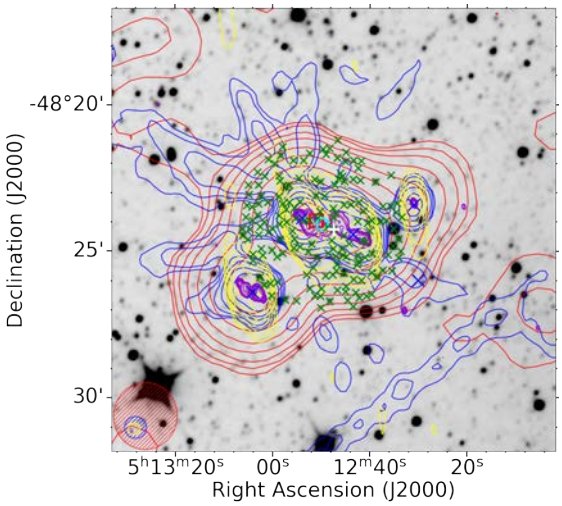

(B) G4Jy 530

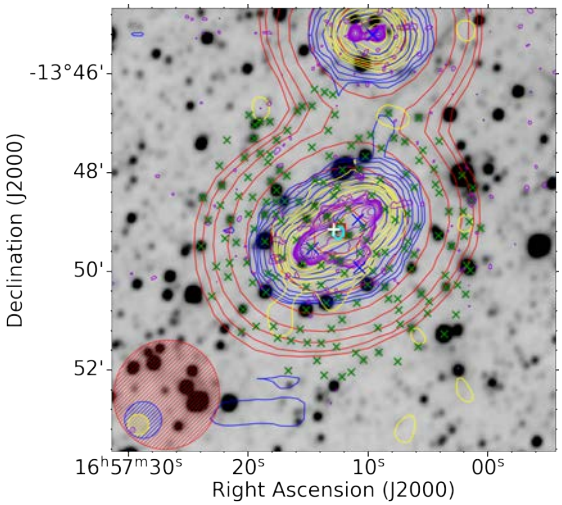

(C) G4Jy 1377

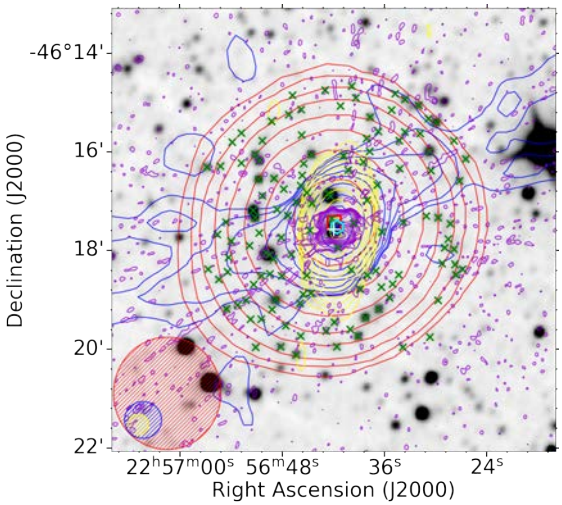

(D) G4Jy 1798

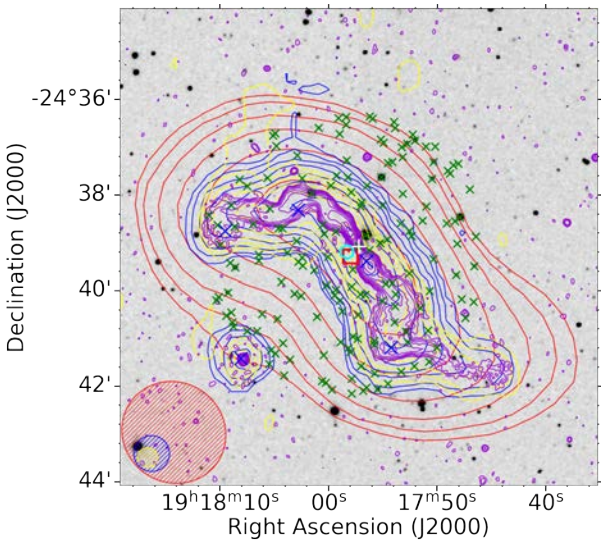

(E) G4Jy 1523

FIGURE 4.5: Overlays for four sources with X shape morphology and one source (G4Jy 1523) with S-/Z-shape morphology in the G4Jy subset. For G4Jy 1523, the grayscale image is from PanSTARRS as the host galaxy in mid-infrared is affected by nearby star. The datasets, symbols, beams and contours are the same as those described in Figure 4.1.

G4Jy 1798 (GLEAM J225641-461726; Figure 4.5D): There are two AllWISE positions near the centroid, and it is not clear which AllWISE position is the most-likely host galaxy. The MeerKAT image reveals an X-shaped galaxy with the primary lobes aligned northwest and southeast while the secondary lobes are aligned northeast and southwest. We then use a 2MASS image as our grayscale and identify the mid-infrared host galaxy as 2MASS J22564196−4617345, at $z = 0.080$.

G4Jy 1523 (GLEAM J191757−243917; Figure 4.5E): MeerKAT contours reveal a Z-shaped radio morphology suggestive of precessing jets. The radio source was previously assigned host flag 'm' as the host galaxy in the AllWISE image is obscured by the nearby star (White et al., 2020b; White et al., 2020a). As a result, the 2MASS image was used as the grayscale base image for the overlay, and the identified host galaxy is 2MASS J19175722−2439053. We find no redshift information in the literature.

4.1.3 Newly identified head-tail and WAT radio sources

Head-tail and WAT radio galaxies are a subclass of radio galaxies associated with clusters. The WAT and head-tail morphology observed is explained by the radio galaxy falling into a cluster. The ram pressure from the surrounding medium pushes the radio jets and lobes backwards, forming a WAT or head-tail morphology (e.g., Jones and Owen 1979; O'Dea and Owen 1986).

G4Jy 14 (GLEAM J000707+053607; Figure 4.6A): 'Double', extended radio morphology, suggestive of radio lobes, is evident in NVSS and TGSS contours. The host galaxy could not be provided for this source as there were two mid-infrared positions at a similar distance from the centroid position, and there was no detection of the radio core. However, the radio contours from MeerKAT reveals two resolved sources, with one being a head-tail radio source towards the northeast. We, therefore, mark the two sources as unrelated and identified the host galaxy of the head-tail radio source as the mid-infrared AllWISE J000707.12+053609.6 ($z = 0.2161$).

G4Jy 113 (GLEAM J010241−215227; Figure 4.6B): The radio source whose radio morphology from NVSS and TGSS is challenging to understand is located in the cluster Abell 133. White et al. (2020b) and White et al. (2020a) could not provide the host galaxy due to the disagreements in the literature concerning the radio morphology of G4Jy 113. Slee et al. (2001) classified the radio source as a cluster relic generated via merger shocks, while Rizza et al. (2000) and Fujita et al. (2002) classified this source as a remnant radio lobe. Our radio image from MeerKAT indicates that G4Jy 113

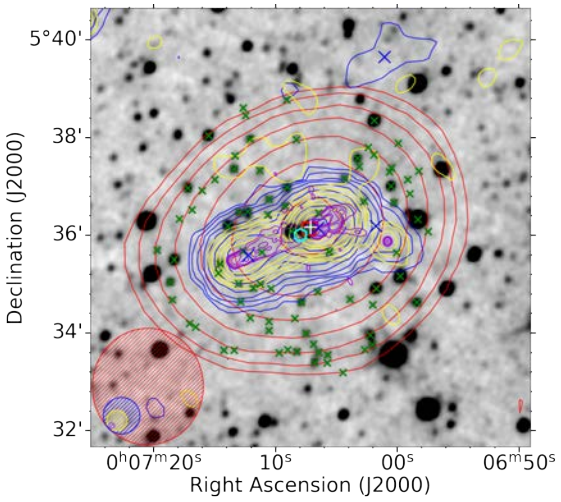

(A) G4Jy 14

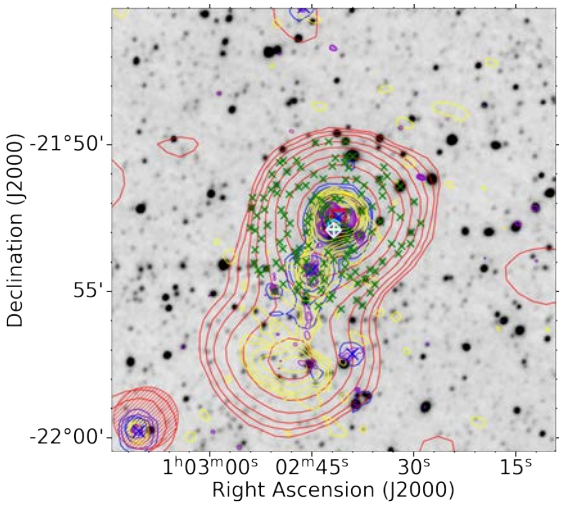

(B) G4Jy 113

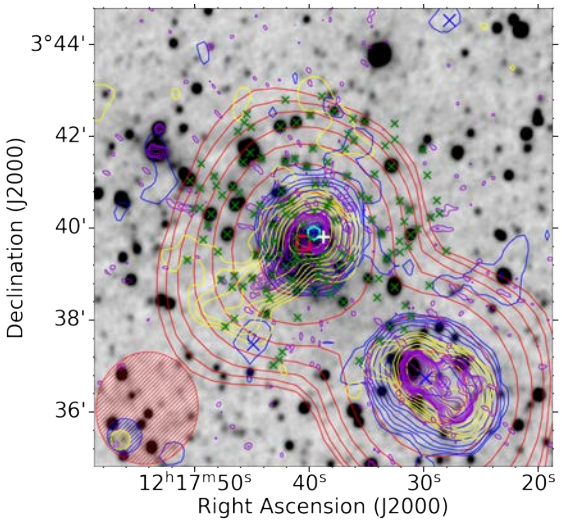

(C) G4Jy 984 (towards NE) and G4Jy 983 (towards SW)

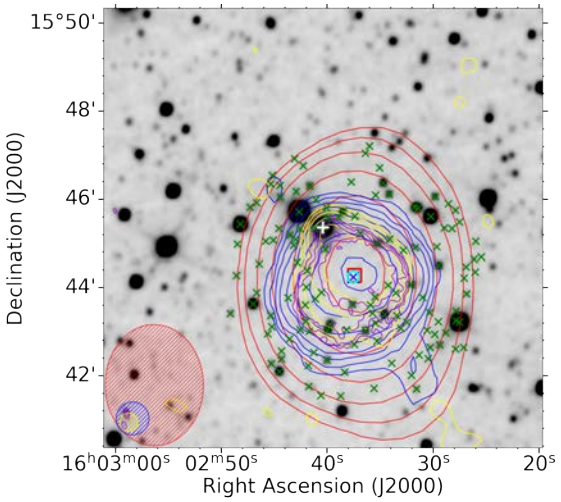

(D) G4Jy 1297

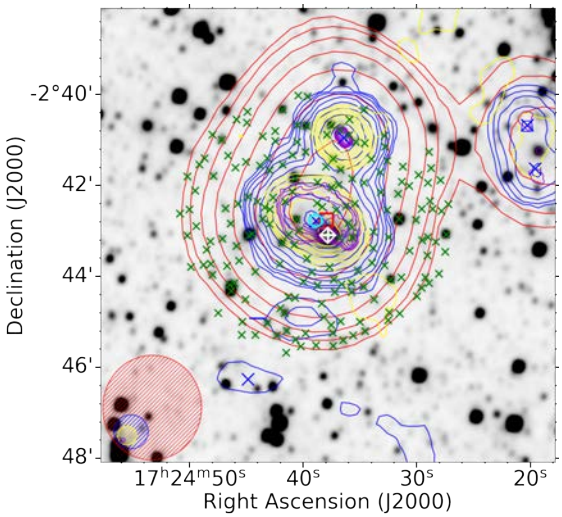

(E) G4Jy 1410

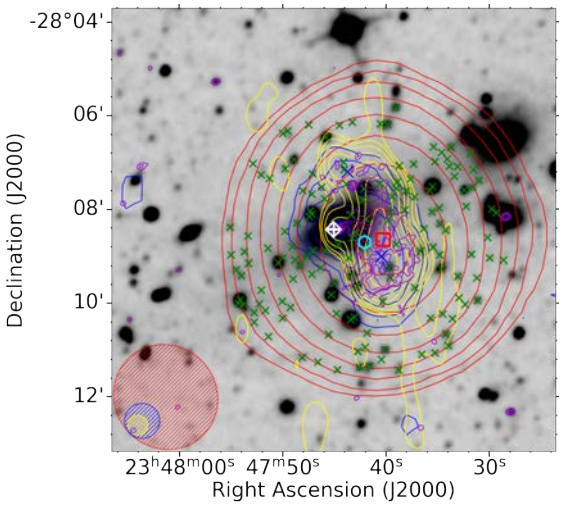

(F) G4Jy 1852

FIGURE 4.6: Radio sources with head tail morphology in the G4Jy subset. The datasets, symbols, beams and contours are the same as those described in Figure 4.1.

is a head-tail radio source with the spectral index, $\alpha^{151\ \mathrm{MHz}}_{1300\ \mathrm{MHz}} = -1.8$. We identify the host galaxy as the AllWISE source J010241.76−215254.2, detected in 6dFGS as g0102418−215256 ($z = 0.057$).

G4Jy 984 (GLEAM J121740+033940; Figure 4.6C): The MeerKAT contours reveal the precise structure of G4Jy 984, with the inner parts of the jet appearing distinct before combining into a tail towards the southeast. We identify the host galaxy as AllWISE J121738.77+033948.2 ($z = 0.0778$). The southwest radio source (not part of the G4Jy subset) appears in the G4Jy catalogue as G4Jy 983 (4C +04.41), previously assigned host flag 'm'. This radio source is in the cluster Z5029 (R.A. = 12:17:14, Dec. = 03:39:23). Head-tail radio morphology is evident in the MeerKAT contours, and we identify the host galaxy as the mid-infrared AllWISE source J121731.43+033656.4 ($z = 0.773$).

G4Jy 1297 (GLEAM J160237+154416; Figure 4.6D): MeerKAT image reveals a head-tail morphology. The host galaxy is AllWISE J160240.38+154521.1 at $z = 0.037$.

G4Jy 1410 (GLEAM J172437−024246; Figure 4.6E): Based on the compactness of the TGSS contours, it was unclear whether G4Jy 1410 (the southern source in the overlay) is a double or a head-tail galaxy, and as such, the host galaxy was not provided. MeerKAT contours reveal a head-tail radio galaxy (G4Jy 1410) and a double morphology radio galaxy (GLEAM J172436−024055) towards north-west, which has a flux density of 3.79 Jy at 151 MHz (White et al., 2020b; White et al., 2020a). Therefore, GLEAM J172436−024055 is not part of the GLEAM 4-Jy catalogue as it does not meet the criterion of flux density being above 4-Jy. We identify the host galaxy of G4Jy 1410 as AllWISE J172437.79−024305.6 detected in 2MRS as J17243782−0243062 ($z = 0.034$). This identification is in agreement with van Velzen et al. (2012).

G4Jy 1852 (GLEAM J234740−280839; Figure 4.6F): This radio source is in the cluster Abell 4035. A head-tail radio morphology with diffuse tail emission is evident in the MeerKAT contours. The mid-infrared source that coincides with the radio core is AllWISE J234745.06−280826.2. This identification corresponds to IC 5358, which is the brightest galaxy in a cluster.

G4Jy 47 (GLEAM J002530−330336; Figure 4.7A): WAT radio morphology is evident in the higher-resolution image from MeerKAT. This radio source appears in the Molonglo Southern 4-Jy Sample (MS4; Burgess and Hunstead 2006) as MRC B0023−33. The host galaxy is the mid-infrared AllWISE J002531.45−330246.2 at redshift $z = 0.050$, which agrees with the host galaxy identification of Burgess and Hunstead (2006) and

van Velzen et al. (2012). An optical counterpart is ESO 350-G-15, the brightest galaxy in cluster AS 41 (ACO89).

G4Jy 528 (GLEAM J051104−131645; Figure 4.7B): WAT morphology with diffuse tail emission is evident in MeerKAT contours. The host galaxy is AllWISE J051104.82−131730.3 at $z = 0.043$.

G4Jy 637 (GLEAM J070130+231313; Figure 4.7C): A radio source known as 4C +23.18 in the literature (Olsen, 1970). Based on the TGSS contours, White et al. (2020a) and White et al. (2020b) identified the morphology as WAT. However, it was unclear which AllWISE source was the host galaxy. With a higher resolution image from MeerKAT, we confirm that this is indeed a WAT radio source. We identify the host galaxy as AllWISE J070129.05+231325.6 at $z = 0.092$.

G4Jy 665 (GLEAM J073104−523710; Figure 4.7D): The radio morphology of G4Jy 665 is not quite clear in both SUMSS and TGSS contours, and as a result, this radio source was assigned a 'complex' morphology label, host flag 'u' and confusion flag '0'. The confusion flag indicates whether multiple sources detected above 6σ in NVSS/SUMSS contribute to the GLEAM component(s). The MeerKAT image reveals two unrelated radio sources, both having a WAT morphology and a detected host galaxy in the mid-infrared. The host galaxy of the southern source (indicated with a white '+' in the overlay) is AllWISE J073104.92−523808.6 at $z = 0.090$, and the host galaxy of the northern source is AllWISE J073103.39−523546.8 at $z = 0.077$. Given that the MeerKAT image reveals two unrelated sources with integrated flux densities of 0.836 Jy (southern source) and 0.314 Jy (northern source) at 1.3 GHz, this implies the integrated flux density at 151 MHz (5.12469 Jy) of G4Jy 665 is the sum of the integrated flux densities of the two sources. With this in mind, G4Jy 665 should be re-inspected in terms of the integrated flux density at 151 MHz, as this parameter is the G4Jy Sample's defining criterion ($S_{151\ \mathrm{MHz}} > 4$ Jy).

G4Jy 693 (GLEAM J081630−703925; Figure 4.7E): WAT radio morphology is evident in the MeerKAT contours, including detection of the radio core. The mid-infrared source that coincides with the radio core is AllWISE J081611.74−703945.3 at redshift $z = 0.033$. Therefore the ID by Jones and McAdam (1992) appears to be incorrect as it does not coincide with the radio's core position.

G4Jy 1067 (GLEAM J132606−272641 and GLEAM J132616−272632; Figure 4.7F): The radio contours from TGSS, NVSS and MeerKAT indicate WAT radio morphology, but the radio core is only detected in the MeerKAT image. The mid-infrared source that

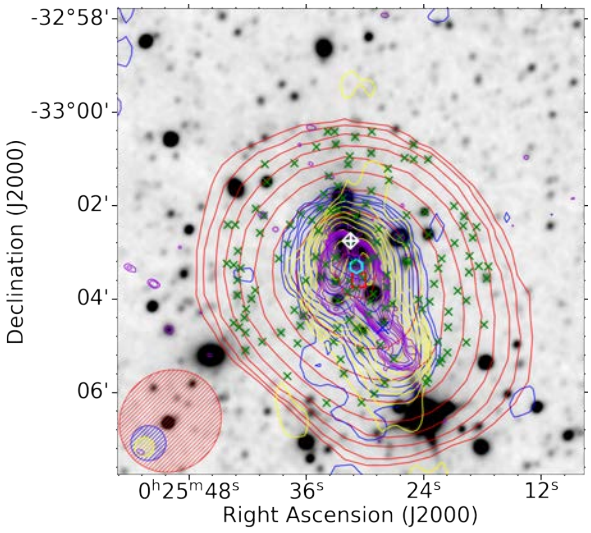

(A) G4Jy 47

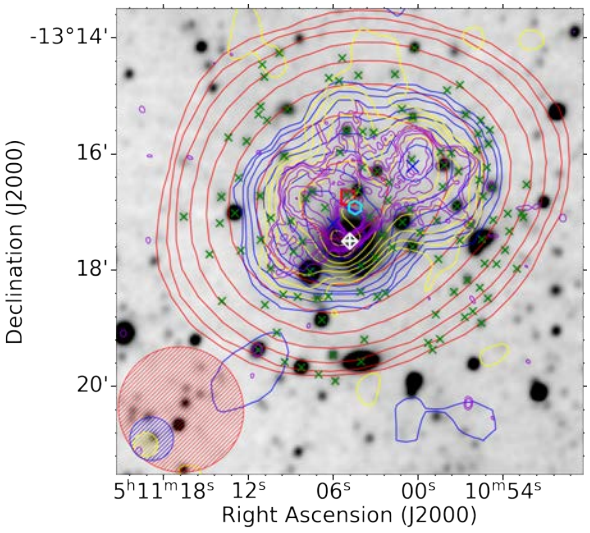

(B) G4Jy 528

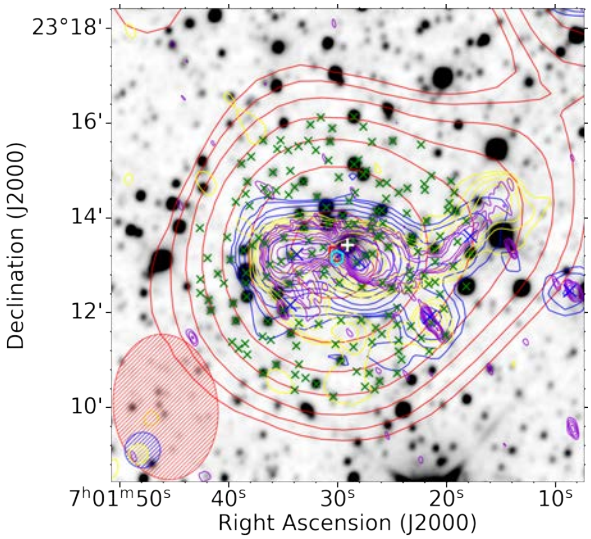

(C) G4Jy 637

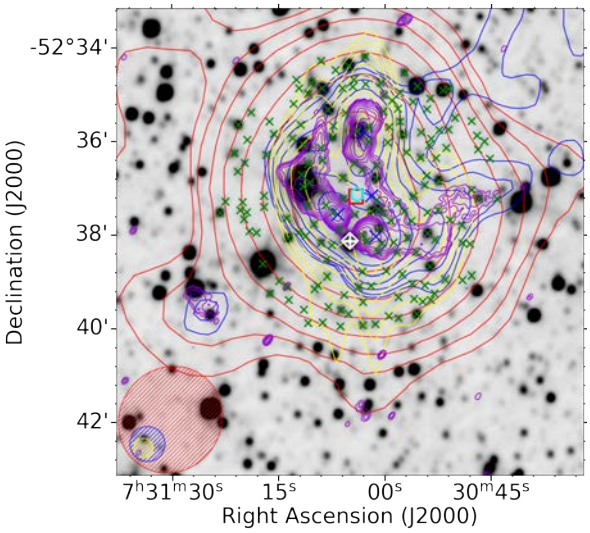

(D) G4Jy 665

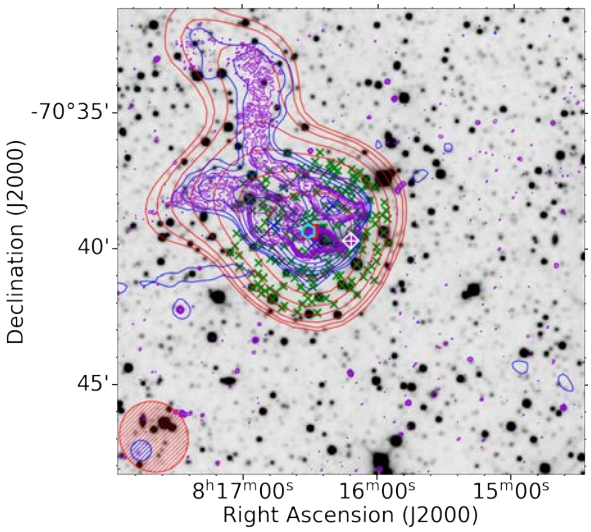

(E) G4Jy 693

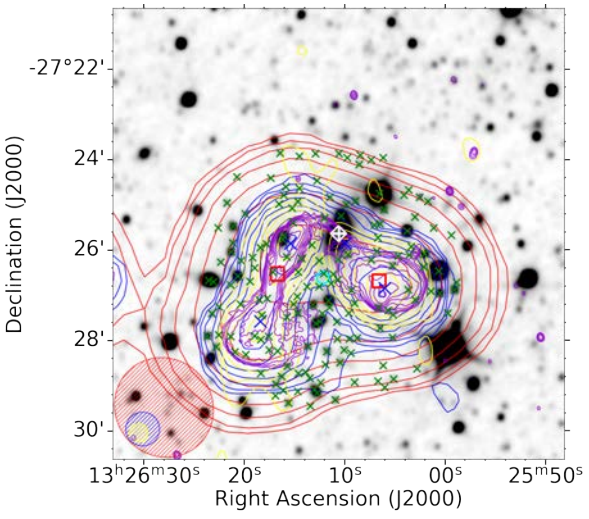

(F) G4Jy 1067

FIGURE 4.7: Radio sources with WAT radio morphology in the G4Jy subset. The datasets, symbols, beams and contours are the same as those described in Figure 4.1.

coincides with the radio core is AllWISE J132610.59−272538.6 at redshift $z = 0.044$. This radio source, known as PKS B1323-271, is in the cluster Abell 1736.

4.1.4 New identification via the spectral index map

G4Jy 1554 (GLEAM J193252−081739): White et al. (2020b) and White et al. (2020a) classified this source as 'double' morphology based on NVSS and TGSS contours. Complex morphology is evident in the MeerKAT contours (Figure 4.8A) with a slight indication of a radio core. The flatter spectral index evident in the map (Figure 4.8B) indicates the position of the radio core. We identify AllWISE J193252.79−081803.4 ($z = 0.101$) as the host galaxy.

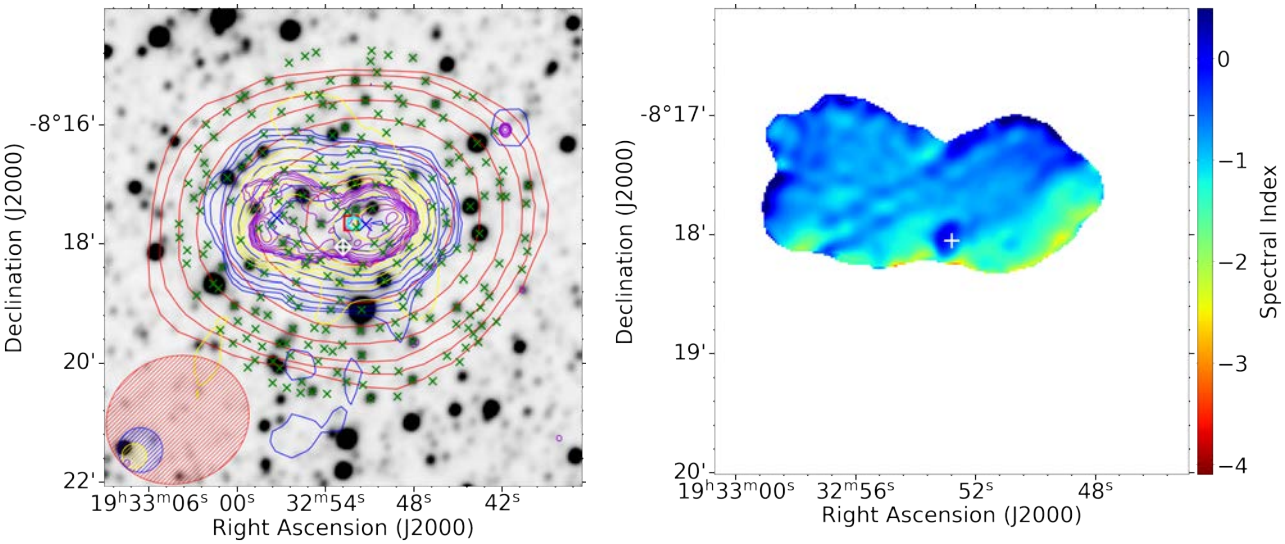

FIGURE 4.8: Left pane: Overlay of G4Jy 1554. The datasets, symbols, beams and contours are the same as those described in Figure 4.1. Right panel: the spectral index map.

4.1.5 Possible GRGs

G4Jy 641 (GLEAM J070525−451328 and GLEAM J070546−451158; PKS B0703−451): A possible GRG with radio emission that spans ∼8-arcmin from lobe to lobe in the 1.3 GHz image from MeerKAT (Figure 4.9A). 'Triple' morphology is evident in the MeerKAT contours, and there is a detection of a hotspot in the western lobe. However, there is an AllWISE position that is coincident with this hotspot, suggesting that this compact emission is not associated with G4Jy 641. The host galaxy that coincide

with the radio core is AllWISE J070532.94−451308.8. This identification is not consistent with the identification provided by Jones and McAdam (1992). We found no redshift information in the literature for the host galaxy.

G4Jy 680 (GLEAM J080225−095823 and GLEAM J080253−095822; Figure 4.9B): This radio source has several AllWISE positions that could be likely the host galaxy (White et al., 2020b). The MeerKAT image reveals the radio core coincided with AllWISE J080236.28−095739.9, detected in 6dFGS as g0802363−095740. This identification is consistent with the optical identification of Schilizzi (1975). The redshift of 0.070 and the angular extent of 9.13 arcmin at 1.4 GHz correspond to the linear size of 0.732 Mpc.

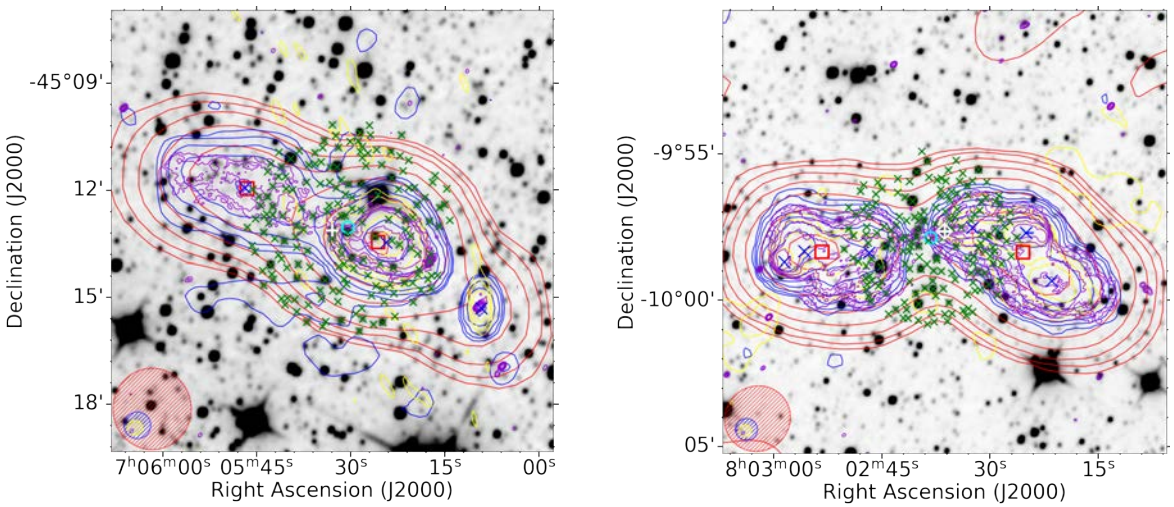

(A) G4Jy 641

(B) G4Jy 680

FIGURE 4.9: Possible GRGs in the G4Jy subset. The datasets, symbols, beams and contours are the same as those described in Figure 4.1.

4.1.6 Quasi-stellar radio source

G4Jy 1843 (GLEAM J233511−663702, PKS B2332−62; Figure 4.10): This radio source has a 'complex' morphology (likely artefects) evident in the SUMSS contours, and there is no coverage in TGSS. The diffraction spikes evident in the mid-infrared image and WISE colours suggest that AllWISE J233510.30−663655.7, close to the centroid position, is a star. However, the 'double' morphology evident in the MeerKAT contours strongly suggest that this AllWISE source is likely the host galaxy of the radio emission. We, therefore, regard AllWISE J233510.30−663655.7 as the host galaxy of this radio emission.

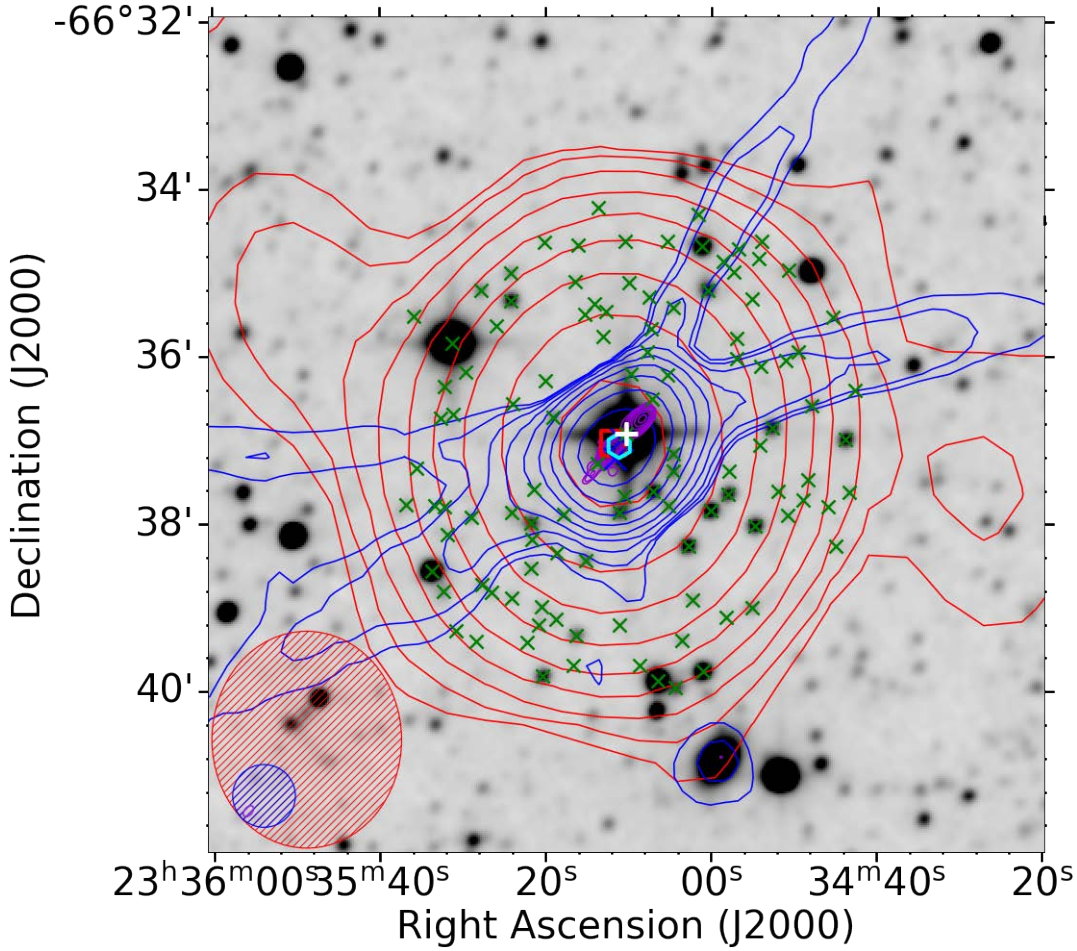

FIGURE 4.10: An overlay of a quasi stellar object (G4Jy 1843). The datasets, symbols, beams and contours are the same as those described in Figure 4.1.

4.2 Amorphous morphology

G4Jy 77 (GLEAM J004130−092221; Figure 4.11) is B0038−096 in the cluster Abell 85. This radio source is interpreted as a radio halo in the literature. The unusual morphology in the NVSS and TGSS contours is also evident in the MeerKAT image. We find that this radio source has the steepest spectral index ($\alpha^{151\ \mathrm{MHz}}_{1300\ \mathrm{MHz}} = -2.604$) in the G4Jy subset, followed by G4Jy 1117 (Figure H.1B).

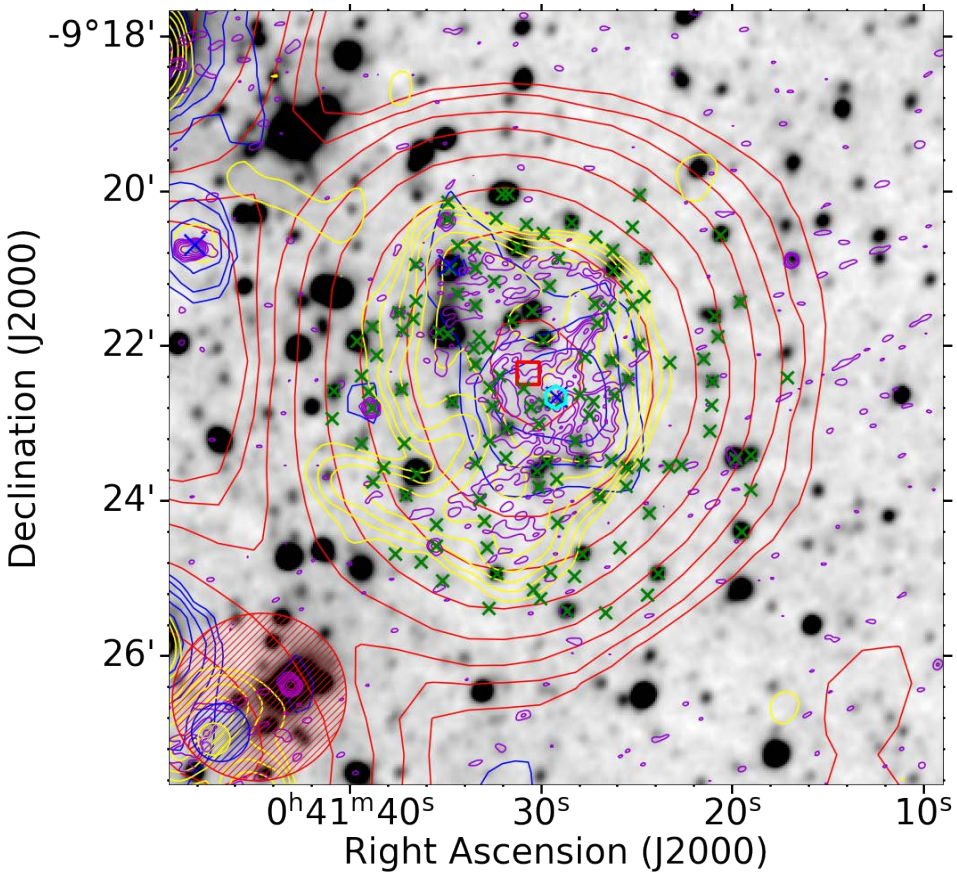

FIGURE 4.11: G4Jy 77 - Radio halo. The datasets, symbols, beams and contours are the same as those described in Figure 4.1.

G4Jy 513 (GLEAM J045826−300717, PKS 0456−30; Figure 4.12A): This radio source in cluster A3297 has a dense field of mid-infrared AllWISE sources. Jones and McAdam (1992) interpreted the radio morphology as cluster halo. The optical identification they provided coincide with the mid-infrared AllWISE source marked with the letter 'A' in our overlay. However, there is another galaxy near the centroid position marked with the letter 'B', which is at redshift 0.0518. The galaxy marked with the letter 'A' is at z = 0.131, which is consistent with the redshift of the cluster. We are unable to provide/confirm whether the provided optical identification by Jones and McAdam (1992) is the host galaxy for this radio emission due to the 'complex', amorphous morphology evident even in the higher-resolution image from MeerKAT. There is no detection of the radio core in both the MeerKAT image and spectral index map (Figure 4.12B).

G4Jy 700 (GLEAM J082231+055626; Figure 4.12C): A radio source with diffuse emission is known as 3C 198 in the 3C catalogue. Wyndham (1966) provided an optical identification corresponding to AllWISE J082231.95+055706.8 marked with the letter 'A' in our overlay. However, there is no core detection in the higher-resolution image

from MeerKAT nor in the spectral index map. MeerKAT images are 5-minute snapshot. A longer integration time may be needed. The spectral index map (Figure 4.12D) reveals old emission in the inner regions, indicating that there is no ongoing ejection of electrons. This is the typical distribution of spectral indices in radio galaxies. Often the plasma near the centre is a result of backflow from the jets and is therefore older with a steeper spectral index.

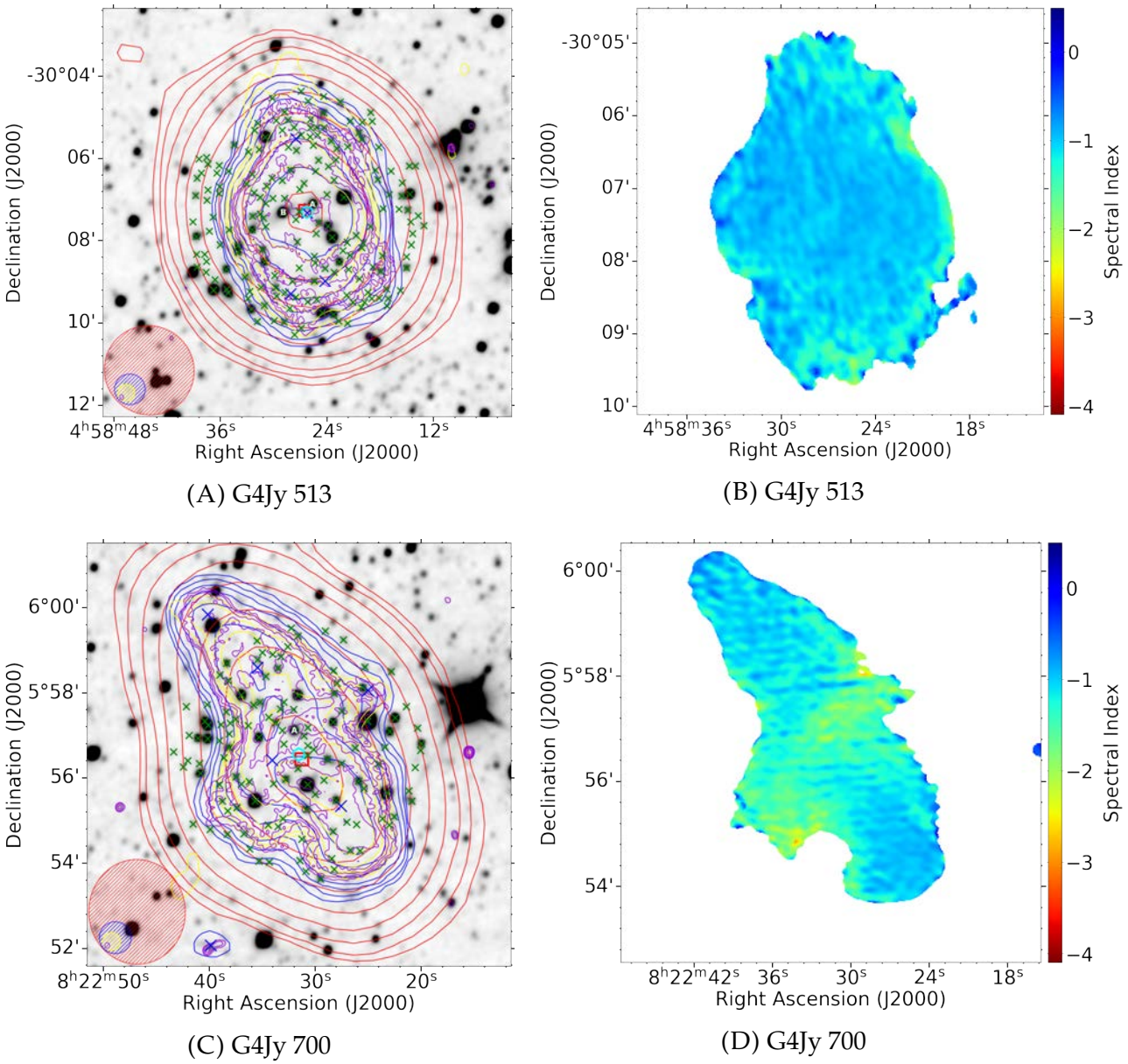

(A) G4Jy 513

(B) G4Jy 513

(C) G4Jy 700

(D) G4Jy 700

FIGURE 4.12: Overlays and spectral index maps of G4Jy 513 and G4Jy 700. The datasets, symbols, beams and contours are the same as those described in Figure 4.1.

4.3 Candidate remnant radio galaxy

Remnant radio galaxies represent a short-lived last phase of the radio galaxy's life cycle, and the cessation of AGN activity characterises them. The absence of compact structures (radio core, jets, and hotspots) signals the 'inactive' phase. The method of identifying remnant radio galaxies based on the absence of a radio core has recently been employed by Mahatma et al. (2018) and Quici et al. (2021). In the G4Jy subset, three radio galaxies (G4Jy 95, G4Jy 559 and G4Jy 1452) are candidate remnant radio sources as the radio core of these sources is not detected at 1.3 GHz. These three sources have two distinct radio lobes. A possible explanation of the radio core not being detected could be that the core is embedded in the strong emission of the lobes, which is the dominant limiting factor.

G4Jy 95 (Figure 4.13) has a 'double' morphology evident in NVSS, TGSS and MeerKAT. We set the host flag to 'u' as there are two AllWISE positions along the lobes axis that are likely the host galaxy. For G4Jy 559 (PKS 0534−61; Figure 4.14A and Figure 4.14B), three AllWISE positions are lying on the axis connecting the radio lobes. We set the host flag of this radio source to 'u'. It is clear from the overlay of G4Jy 1452 (Figure 4.14C and Figure 4.14D) that AllWISE J175851.11−673829.0 is the host galaxy as it is the only AllWISE source lying in the axis of the radio lobes.

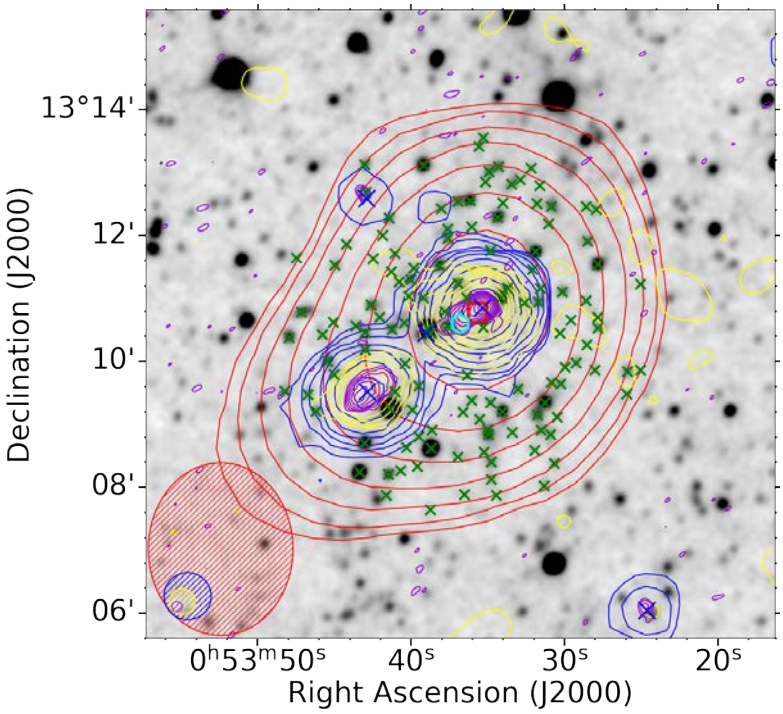

FIGURE 4.13: G4Jy 95: A candidate remnant radio galaxy in the G4Jy subset. Contours start at 3σ, where $\sigma = 0.5160$ mJy/beam

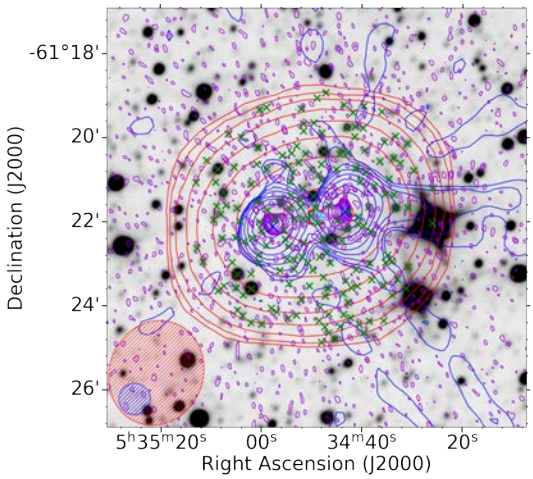

(A) G4Jy 559: Contours start at 3σ.

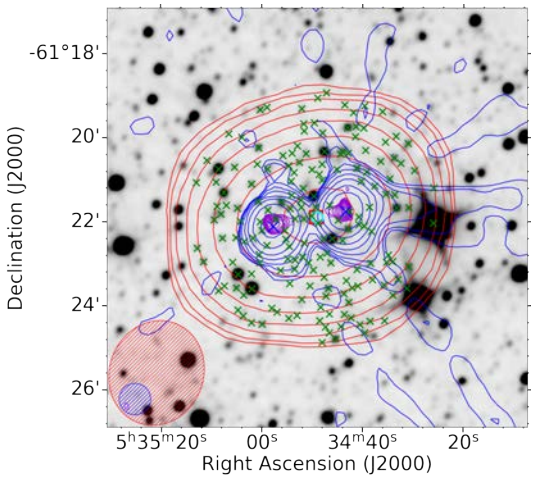

(B) G4Jy 559: Contours start at 12σ.

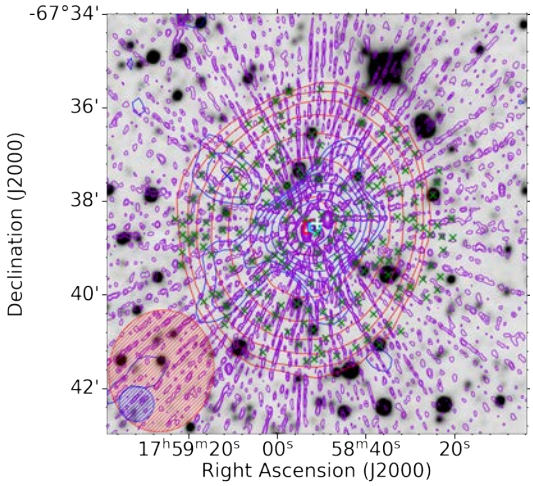

(C) G4Jy 1452: Contours start at 3σ.

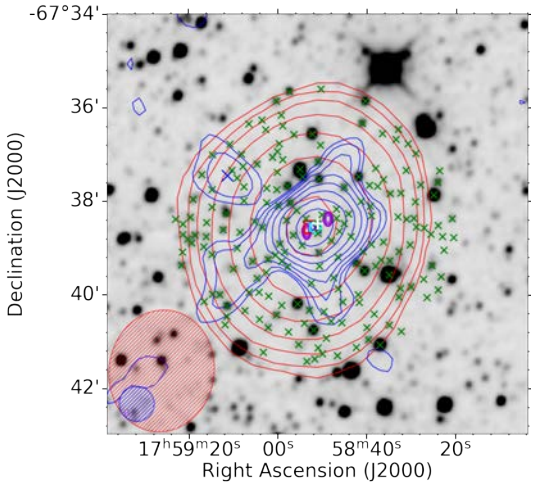

(D) G4Jy 1452: Contours start at 96σ.

FIGURE 4.14: Candidate remnant radio sources in the G4Jy subset. For G4Jy 559, $\sigma = 0.096$ mJy/beam and for G4Jy 1452, $\sigma = 0.069$ mJy/beam. The datasets, symbols, beams and contours are the same as those described in Figure 4.1.

4.4 Infrared Faint Radio Sources (IFRS)

The angular resolution and sensitivity of a survey plays a vital role in morphological classification and host galaxy identification. However, even with deep infrared surveys, the host galaxy of some radio sources is not detected. These galaxies are likely at high redshift. Radio sources whose host galaxy is not detected in the infrared are classed IFRSs (Norris et al., 2006; Zinn, Middelberg, and Ibar, 2011). In the G4Jy subset, 13 sources (Figures 4.15, G.1 and G.2) have a faint host galaxy in the infrared.

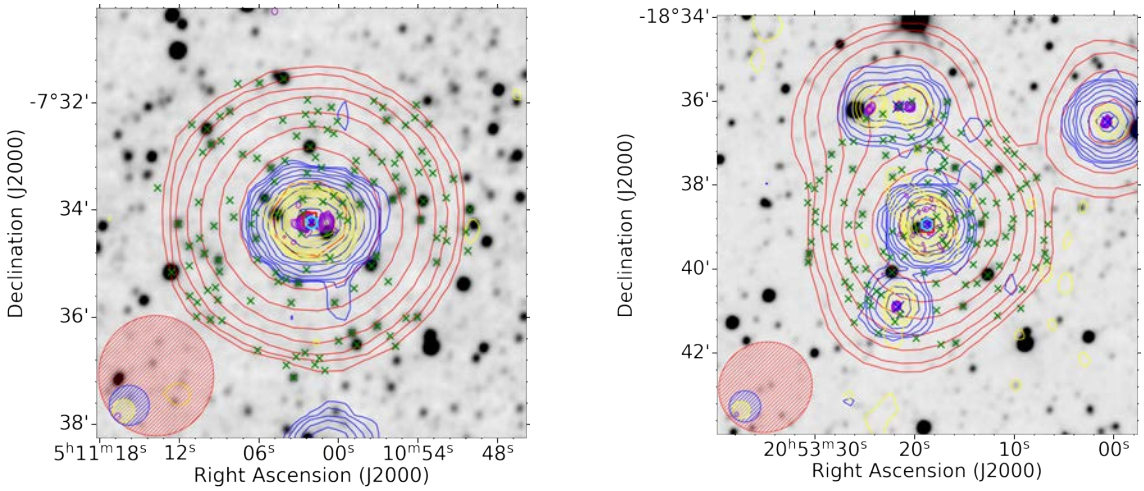

(A) G4Jy 527.

(B) G4Jy 1663.

FIGURE 4.15: Candidate IFRS in the G4Jy subset. The datasets, symbols, beams and contours are the same as those described in Figure 4.1.

4.5 Unrelated sources

Radio sources whose radio emission is blended together by NVSS/SUMSS (45 arcsec resolution) and TGSS (25 arcsec resolution) but MeerKAT images ($\sim$ 7 arcsec resolution) reveal two resolved sources.

G4Jy 456 (Figure 4.16A): The extended, 'double' morphology is evident in the NVSS and TGSS contours. To resolve the ambiguity of the host galaxy for this source, we obtained a higher-resolution radio image from archival VLASS (VLA Sky Survey [3 GHz and 2.5 arcsec resolution]; Lacy et al. 2020) as the MeerKAT visibilities for this particular source, and G4Jy 453 are entirely flagged. The VLASS contours (orange contours in Figure 4.16A) reveals two unrelated sources with 'single' and 'double' morphologies, respectively. The radio source with 'single' morphology has a faint mid-infrared host, while the mid-infrared counterpart of the 'double' morphology source is AllWISE J042536.76+083217.7 at $z = 1.1$.

G4Jy 671: In both SUMSS and TGSS contours, the radio morphology of G4Jy 671 is not clear. The radio morphology could either be a head-tail, core-jet or double morphology with asymmetric jets. Hence this radio source was given the morphology label 'complex', host flag 'u' and confusion flag '0'. The 1.3 GHz radio map from MeerKAT shows two unrelated radio sources with triple (northern source, $S_{1.3\ \mathrm{GHz}} = 1.062\ Jy$) and single (southern source; $S_{1.3\ \mathrm{GHz}} = 0.237$ Jy) morphology, both having a detected

host galaxy in mid-infrared. The host galaxy of the triple morphology source is AllWISE J074146.64−523415.9, and AllWISE J074151.46−523524.4 is the host galaxy of the radio source with single morphology. Given that there are two unrelated sources resolved by MeerKAT, the confusion flag of G4Jy 671 needs to be updated to '1'.

G4Jy 1491 (GLEAM J183356−394023, Figure 4.16C): Based on the SUMSS and TGSS contours, it was unclear whether this radio source has a head-tail, double or core-jet morphology (White et al., 2020a; White et al., 2020b), and as such, it was assigned a 'complex' morphology label. The MeerKAT image indicates that there are two unrelated sources having single and triple morphology, respectively. The radio source with single morphology towards the north has no detected host galaxy in the mid-infrared, while the host galaxy of the southern source with triple morphology is AllWISE J183359.36-394158.3. The integrated flux density of G4Jy 1491 at 151 MHz is 4.24799 Jy. Given that the MeerKAT image reveals two unrelated sources, this implies the integrated flux density at 151 MHz for G4Jy 1491 is the sum of the integrated flux densities of the two sources resolved by MeerKAT. With this in mind, the integrated flux density at 151 MHz of G4Jy 1491 needs to be recalculated and the confusion flag updated to '1'.

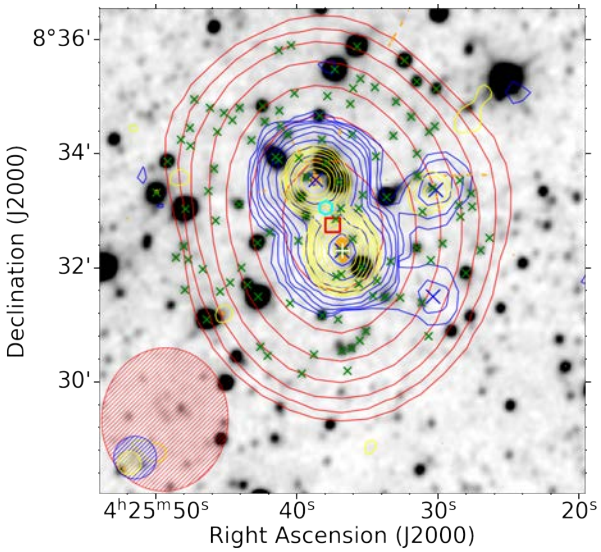

(A) G4Jy 456

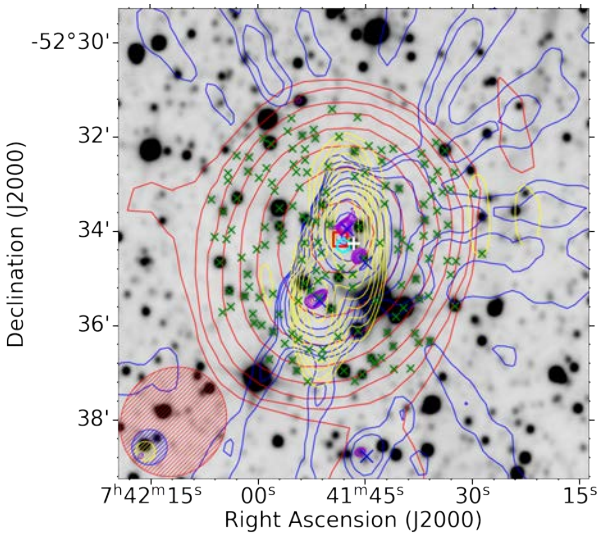

(B) G4Jy 671

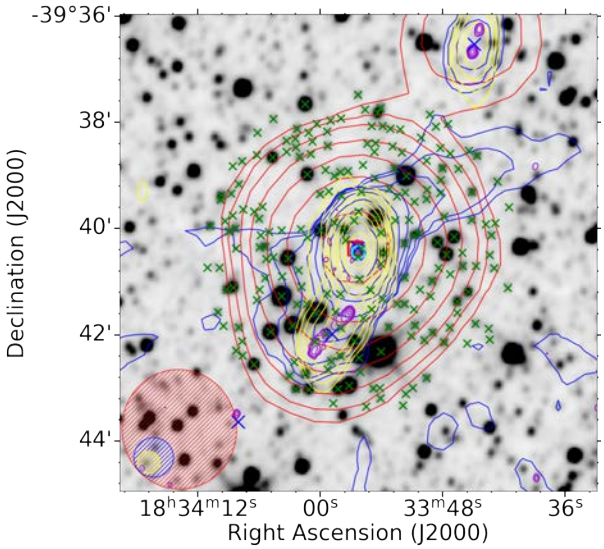

(C) G4Jy 1491

FIGURE 4.16: Radio sources in the G4Jy subset whose radio emission is blended together by NVSS/SUMSS and TGSS. The VLASS contours (orange) in the overlay of G4Jy 456 shows two unrelated sources. The datasets, symbols, beams and contours are the same as those described in Figure 4.1.

Chapter 5

Discussion

5.1 Host-galaxy identification

An initial objective of this study was to identify the host galaxy of the radio emission of 140 G4Jy sources (referred to as the G4Jy subset) through the visual inspection of overlays. The host-galaxy identification is essential if we are to combine the low-frequency radio data with other datasets, thereby enabling us to construct a comprehensive, multi-wavelength perspective of the various processes occurring within these radio sources. Our morphological classification and host-galaxy identification are based on visually inspecting the overlays, focusing on the MeerKAT contours and the distribution of mid-infrared sources. Of the 98 sources with an identified host galaxy, the host galaxy of G4Jy 456 was identified using the contours from archival VLASS data. G4Jy 453 and G4Jy 456 both have no MeerKAT data. This could result from the visibilities being entirely flagged due to strong RFI.

The spectral index maps were used for radio sources where the host galaxy could not be identified through the visual inspection of the overlays. The components of a radio galaxy, the radio core and lobes, are expected to have different spectral indices. It is expected that the radio core will have a flat spectral index; $\alpha \sim -0.4$, and the radio lobes will have steep spectral index; $\alpha \sim -0.7$ (Eckart et al., 1986), where $S_\nu \propto \nu^\alpha$. Through the visual inspection of the spectral index maps of G4Jy subset sources, only one G4Jy source (G4Jy 1554) was found to have a distinguishable spectral index map where the radio core is visible. The host galaxy identification of this radio source brings the total number of radio sources with an identified host galaxy to 98. These radio sources are therefore assigned host flag 'i'. Of the remaining 42 sources, 27 are assigned host flag 'u', 14 have a faint mid-infrared host and they are assigned host flag 'm', and one radio source (G4Jy 77) was assigned host flag 'n'. The host flag 'i' indicates that the radio source has an identified host galaxy, host flag 'u' indicates that the radio source has ambiguous host galaxy identification, host flag 'm' characterize a faint mid-infrared host and sources with host flag 'n' are those whose host galaxy

should not be provided given the type of radio morphology (i.e., the radio source is a radio halo).

5.1.1 Plot of centroid-to-host-galaxy separation.

Figure 5.1 shows the separation between the host galaxy position and the brightness-weighted centroid position for all the sources with an identified host galaxy in the G4Jy subset and G4Jy Sample. The brightness-weighted centroid position is the weighted average of the NVSS or SUMSS components, where the flux densities of these components are taken as weights. The brightness-weighted centroid position is subject to error, if, for instance, the G4Jy source has two components in NVSS/SUMSS, and one component is two times brighter than the other component. Then the brightness-weighted centroid position will be shifted to the brighter component. This centroid position will then have a significant offset from the radio core and the host galaxy position. The median offset in R.A. and Dec. for the G4Jy subset are 0.108 arcsec and 2.322 arcsec, -0.144 arcsec and -0.040 arcsec for the G4Jy Sample.

While most the G4Jy Sample sources have positional offset in the range $|\text{R.A.}| < 10''$, and $|\text{Dec.}| < 10''$, most of the G4Jy subset sources have positional offset in the range $|\text{R.A.}| > 10''$, and $|\text{Dec.}| > 10''$. We expect to have this larger positional offset for the G4Jy subset sources as the brightness-weighted centroid position in most cases does not coincide with the position of the radio core. Moreover, the G4Jy subset sources have very unusual morphologies at 25 and/or 45 arcsec resolutions.

Furthermore, some radio sources have complex morphologies, including head-tail and WAT morphologies evident in the MeerKAT contours. The resolution of NVSS and SUMSS is not sufficient to distinguish the components of the associated G4Jy source. Moreover, we found three sources in the G4Jy subset that had double morphology in NVSS/SUMSS and TGSS. However, MeerKAT images reveal that they are unrelated.

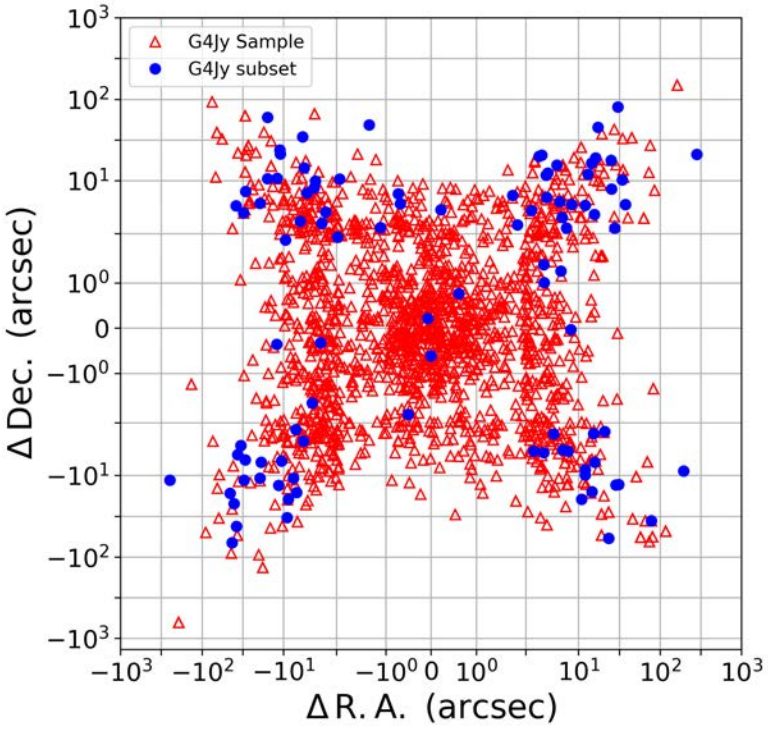

FIGURE 5.1: This figure shows the positional offset in R.A. and Dec. between the brightness-weighted centroid position and the host galaxy position for radio sources with an identified host galaxy in the G4Jy subset and the G4Jy Sample. The median offset in R.A. and Dec. for G4Jy subset are 0.108 arcsec and 2.322 arcsec.

5.1.2 WISE color-color plot

Figure 5.2 shows the WISE colour-colour plot (W1 − W2 versus W2 − W3) for the G4Jy subset (blue data points) and G4Jy Sample (red data points). The two WISE photometric colours have been used in several studies to distinguish different types of astronomical objects.

In this study, the WISE colour-colour diagram is plotted to see where the G4Jy Sample and G4Jy subset lie in this plot. Sources in both the G4Jy Sample and G4Jy subset occupy all the defined regions in this plot, with a handful of sources in the AGN wedge (solid black box) defined by Mateos et al. (2012). 31 sources in the G4Jy subset are in the elliptical region, 18 occupy the spiral region, 4 sources are in the star-formation region, 37 are in the AGN region, and 2 are in the ULIRG (Ultra-luminous Infrared Galaxies)/obscured AGN region. The elliptical and spiral regions are known to be dominated by low-excitation radio galaxies (LERGs) as these sources lack a dusty torus. High-excitation radio galaxies (HERGs) dominate the AGN region (W2 − W1

> 0.5). Moreover, LERGs are believed to be associated with FR-I and HERGs with FRII. However, some studies showed that there is an overlap between these classes where HERGs are associated with FR-I (e.g., Hardcastle, Evans, and Croston 2009; Whittam et al. 2018; Best and Heckman 2012. Classifying the G4Jy subset sources into LERGs and HERGs or FR-I and FR-II was beyond the scope of this study.

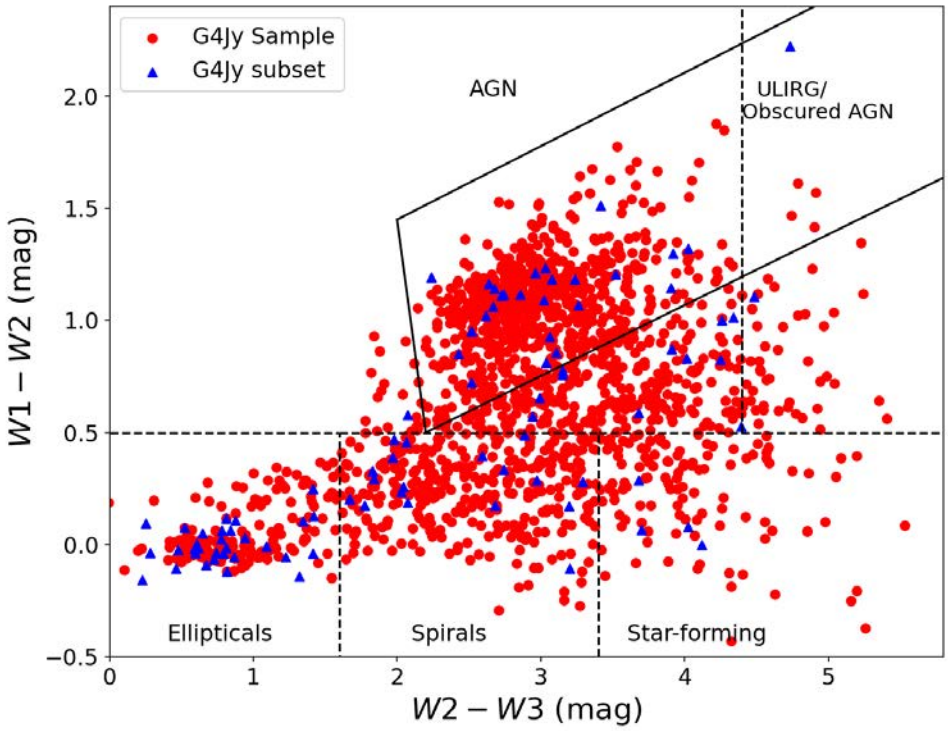

FIGURE 5.2: WISE colour-colour plot. W1, W2 and W3 correspond to wavelengths 3.4 μm, 4.6 μm and 12 μm.

5.2 Radio properties of the host galaxy

5.2.1 Spectral indices

The two point spectral index (α) between two radio frequencies (151 MHz and 1300 MHz) was calculated for 138 sources in the G4Jy subset assuming $S \propto \nu^{\alpha}$, where S is the integrated flux density at frequency ν. The left panel of Figure 5.3 shows the overall distribution of the two-point spectral index between 151 MHz and 1300 MHz for the G4Jy subset and the distribution of the two-point spectral index between 151 MHz and 1400 MHz for G4Jy Sample (obtained from the G4Jy catalogue). Both samples have a Gaussian distribution. The median spectral index of the G4Jy Sample

and G4Jy subset are -0.781 and -0.819, close to -0.7 value, which is the expected value of radio sources dominated by radio lobes. The majority of the sources in the G4Jy subset have double morphology with steep spectral index in the range $-1.2 < \alpha^{151\ \mathrm{MHz}}_{1300\ \mathrm{MHz}} < -0.5$ (right panel of Figure 5.3).

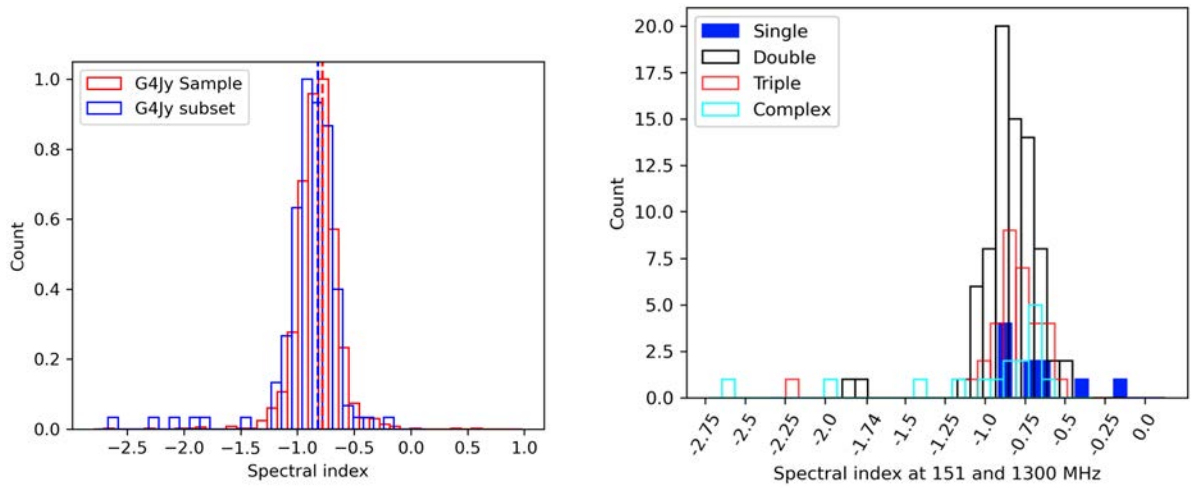

FIGURE 5.3: Histogram of the spectral index for the G4Jy subset

5.2.2 Radio luminosity

After identifying the host galaxy of the G4Jy subset sources, the next step was to obtain redshifts from existing catalogues/databases. Obtaining redshifts means that we can calculate the radio luminosity at 1.3 GHz and the linear size of the G4Jy subset. Of 98 radio sources with an identified host galaxy, 51 sources have redshift available from the literature. The 1.3 GHz radio luminosity ($L_{1.3\ GHz}$) was calculated using the equation:

$$L_{1.3\ \mathrm{GHz}} = \frac{4\pi D_L^2 S_{1.3\ \mathrm{GHz}}}{(1+z)^{1+\alpha}} \tag{5.1}$$

D_L is the luminosity distance, $S_{1.3\ GHz}$ is the integrated flux density at 1.3 GHz, z is the redshift, and α is the spectral index at 151 MHz and 1300 MHz. The luminosity distance was calculated using Ned Wright's cosmology calculator[1], assuming a flat Lambda CDM model ($H_0 = 70$ km/s/Mpc, $\Omega_m = 0.3$ and $\Omega_\Lambda = 0.7$). Figure 5.4 shows the distribution of the 1.3 GHz radio luminosity of the sources in the G4Jy subset where redshift is available. The majority of the sources have radio luminosities in the order of 10^{25} W/Hz to 10^{27} W/Hz. These radio sources have a typical spectral index in the range $-1.2 < \alpha^{151\ \mathrm{MHz}}_{1300\ \mathrm{MHz}} < -0.5$ (Figure 5.5). The radio sources with radio luminosity of the order 10^{28}W/Hz have a flat spectral index ($\alpha^{151\ \mathrm{MHz}}_{1300\ \mathrm{MHz}} > -0.5$).

[1]http://www.astro.ucla.edu/ wright/CosmoCalc.html

In contrast, radio sources with a steep spectral index ($\alpha_{1300\ \mathrm{MHz}}^{151\ \mathrm{MHz}} \leq -1.2$) have radio luminosities of the order 10^{23} W/Hz to 10^{24} W/Hz.

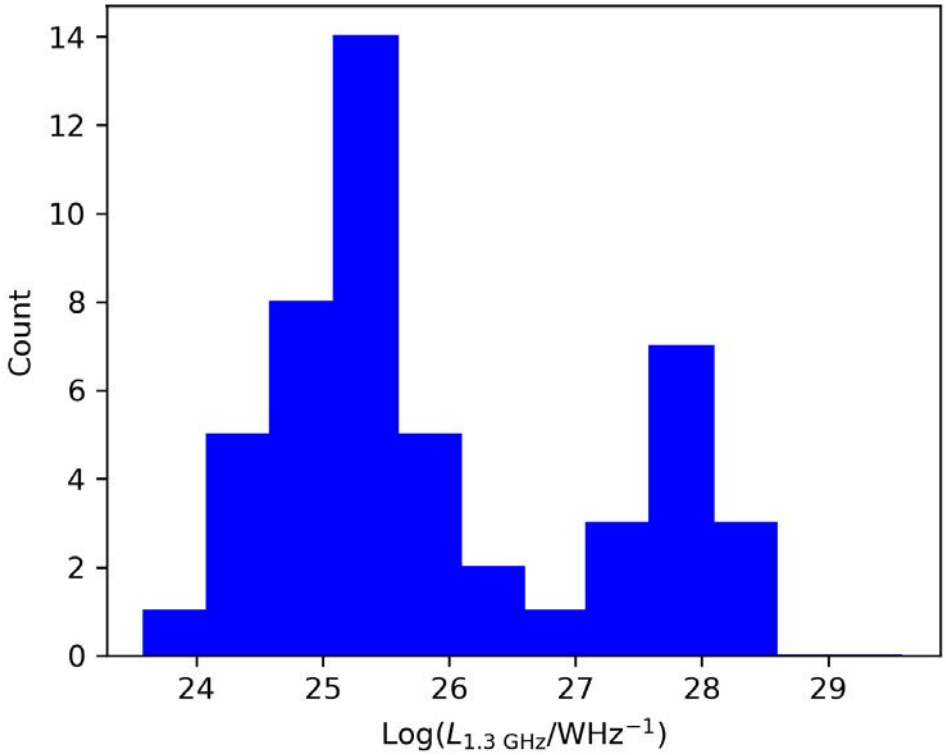

FIGURE 5.4: The distribution of the 1.3 GHz radio luminosity

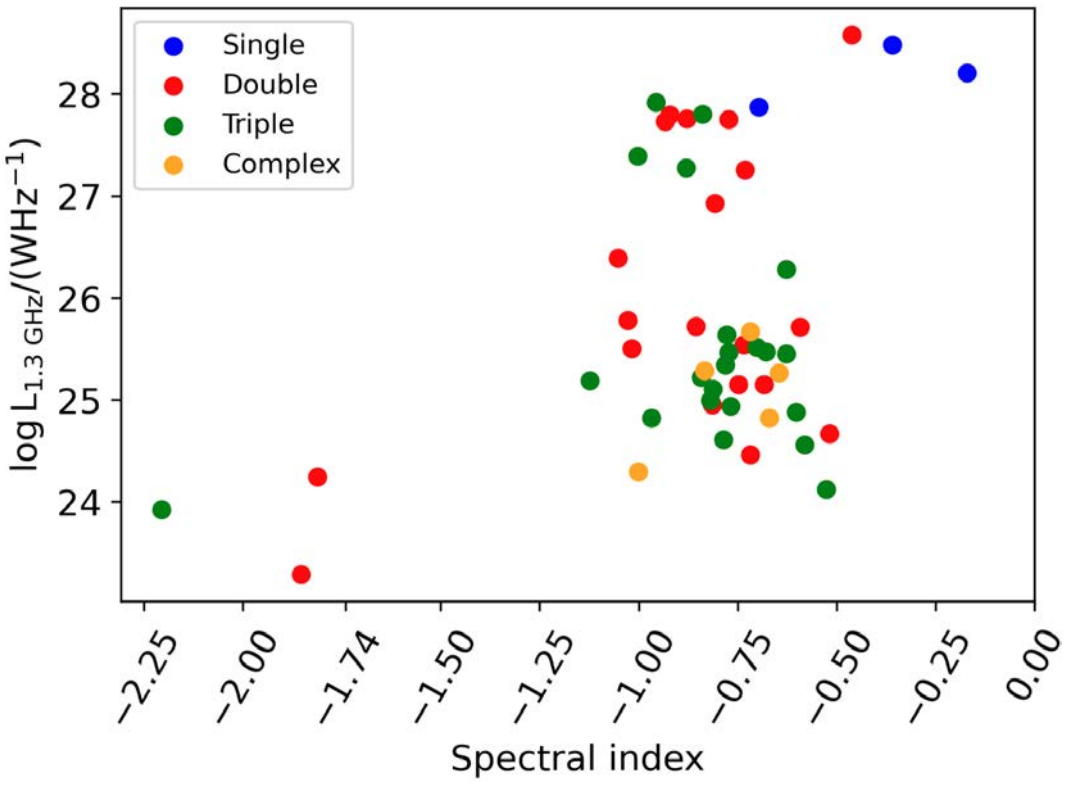

FIGURE 5.5: Plot of the two-point spectral index between 151 MHz and 1300 MHz vs. radio luminosity at 1300 MHz.

Chapter 6

Conclusion

6.1 Summary

The main aim of this study was to identify the host galaxy of 140 sources referred to as the G4Jy subset. Here, I summarise the work done in this study.

- I visually inspected 140 sources referred to as the G4Jy subset by overlaying radio contours from GLEAM (200 MHz), NVSS (1400 MHz)/SUMSS (843 MHz), TGSS (150 MHz) and MeerKAT (1300 MHz) onto mid-infrared WISE (3.4μm) images, supplemented by AllWISE positions.

- The G4Jy subset sources are classified into 'single', 'double', 'triple' or 'complex' morphology based on the MeerKAT contours. Eleven sources have 'single' morphology label, 78 have 'double', 33 have 'triple', and 16 have 'complex' morphology.

- Through the visual inspection of the overlays, the MeerKAT images revealed various sources with various radio morphologies. While the G4Jy subset is dominated by radio sources with typical symmetric lobes evident in the MeerKAT images of $\sim$ 7 arcsec resolution, 10 radio sources are head-tail, 14 are WAT and 5 are S-/Z-/X-shaped sources.

- Out of 140 sources, 98 radio sources have an identified host galaxy and are assigned host flag 'i'. Of the remaining sources, 27 have uncertain host galaxy and are assigned host flag 'u', 14 sources have a host galaxy that is too faint to be detected in the mid-infrared and are labeled 'm', and one radio source (G4Jy 77) is labelled 'n' as this radio source is interpreted as a cluster relic in the literature.

- Based on the host to centroid position separation plot, the G4Jy subset have larger positional offset compared to the G4Jy Sample. This is expected as the brightness weighted centroid position in most cases does not coincide with the host galaxy position.

- We obtained redshift for radio sources with an identified host galaxy in the G4Jy subset and calculated their radio luminosity at 1.3 GHz. Radio sources with the steepest spectral index ($\alpha^{151\ \mathrm{MHz}}_{1300\ \mathrm{MHz}} < -1.2$) have low radio luminosities. In contrast, those with flat spectral index ($\alpha^{151\ \mathrm{MHz}}_{1300\ \mathrm{MHz}} > -0.5$) have higher radio luminosities and redshifts above 1.

This study has demonstrated the significance of a telescope's angular resolution and sensitivity in morphological classification and host-galaxy cross-identification of radio sources at low frequencies. The sensitivity and angular resolution ($\sim$ 7 arcsec) of MeerKAT has allowed us to resolve the ambiguous host-galaxy identification and enigmatic radio morphologies of the G4Jy subset evident in NVSS/SUMSS (45 arcsec) and/or TGSS (25 arcsec) images.

We have classified three radio sources in the G4Jy subset as candidate remnant radio galaxies. These three sources have distinct radio lobes in MeerKAT images, but MeerKAT does not detect their radio cores. In order to confirm whether these radio sources have reached their "inactive phase", they need to be observed at higher radio frequencies with better sensitivity.

6.2 Future work

- Observe the candidate remnant radio sources with the MeerKAT S-band.
- Obtain images from ASKAP (Australian Square Kilometre Array Pathfinder; Hotan et al. 2021) and re-inspect the 42 G4Jy subset sources with no identified host galaxy.
- Obtain the redshifts of sources with an identified host galaxy. Some of these G4Jy subset sources have already been observed with SALT (Southern African Large Telescope; Buckley, Swart, and Meiring 2006).

Appendix A

Appendix: MeerKAT intensity maps of X-,S-/Z-shaped radio sources

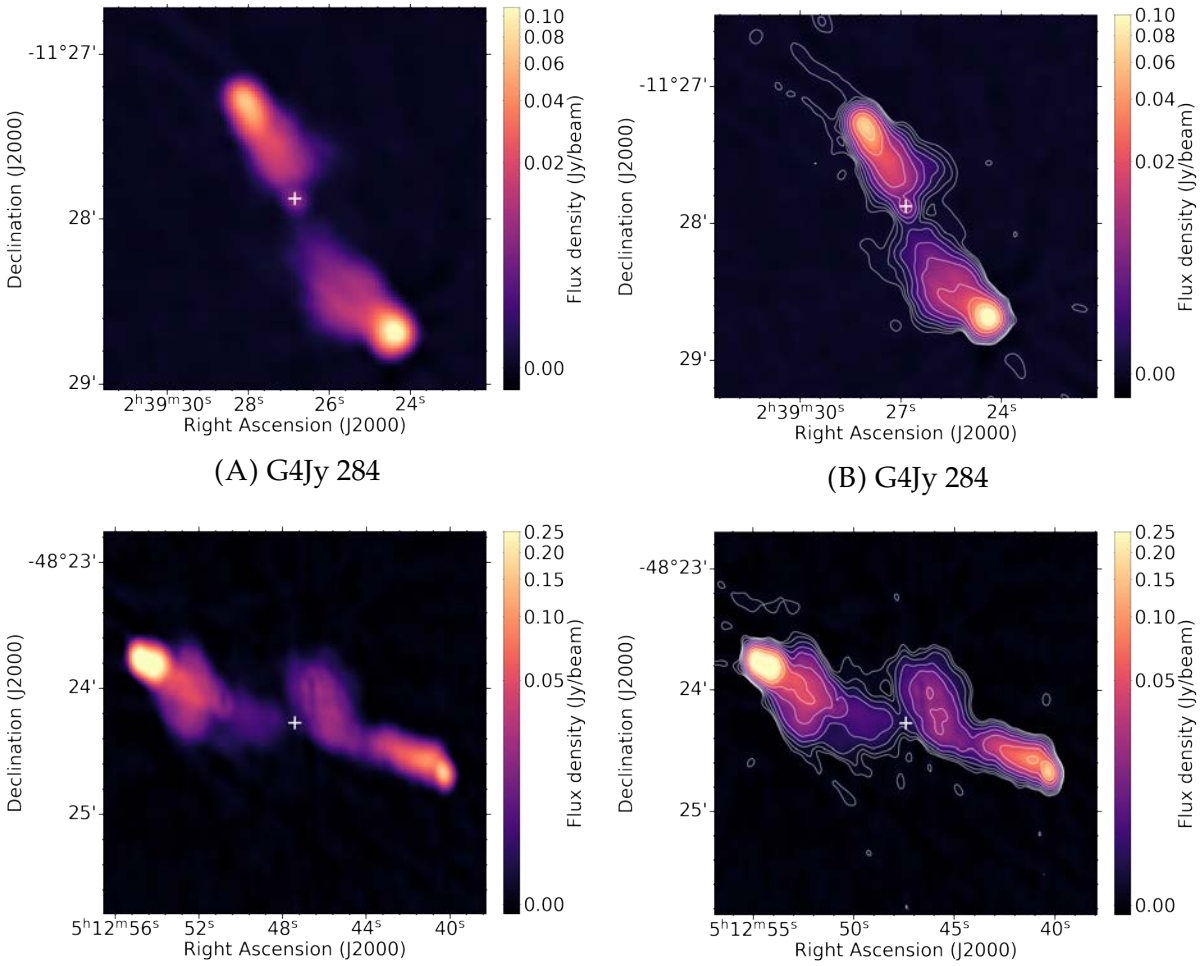

(A) G4Jy 284

(B) G4Jy 284

(C) G4Jy 530

(D) G4Jy 530

FIGURE A.1: Left panel: MeerKAT Intensity maps (1.3 GHz, $\sim$ 7 arcsec resolution) of two radio sources with X-shape morphology. The '+' sign is the mid-infrared host galaxy position. Right panel: MeerKAT contours overlaid on the intensity maps.

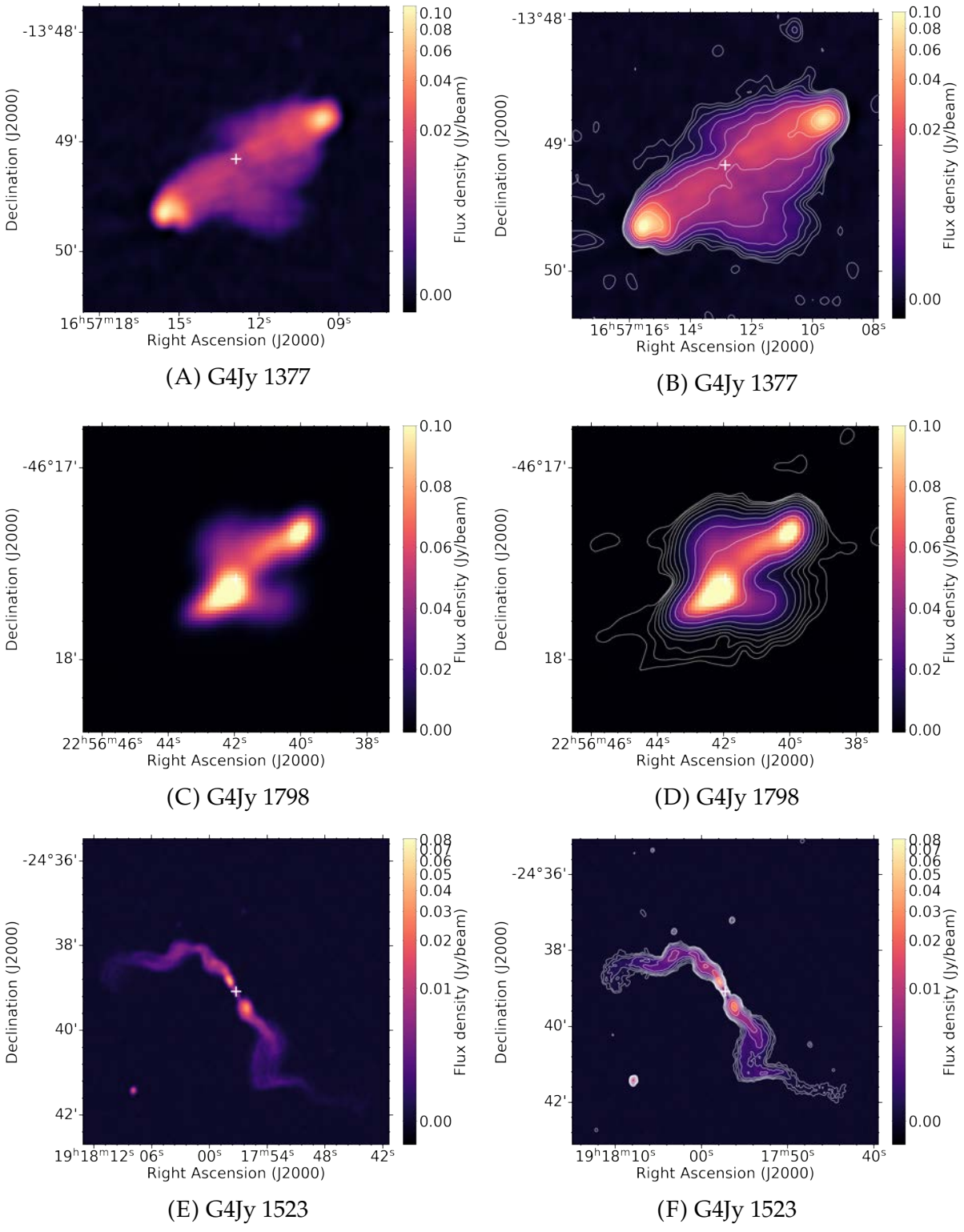

(A) G4Jy 1377

(B) G4Jy 1377

(C) G4Jy 1798

(D) G4Jy 1798

(E) G4Jy 1523

(F) G4Jy 1523

FIGURE A.2: Left panel: MeerKAT Intensity maps (1.3 GHz, $\sim$ 7 arcsec resolution) of two radio sources with X-shape morphology and one (G4Jy 1523) with S-/Z-shaped morphology. The '+' sign is the mid-infrared host galaxy position. Right panel: MeerKAT contours overlaid on the intensity maps.

Appendix B

Appendix: Radio sources with Head-tail and WAT morphology

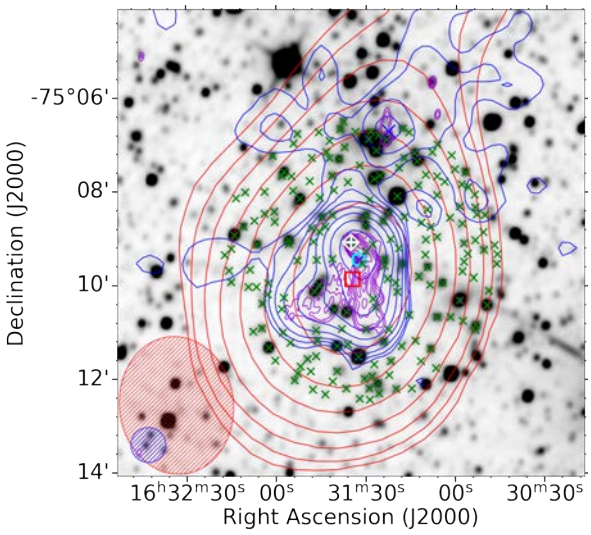

(A) G4Jy 1342

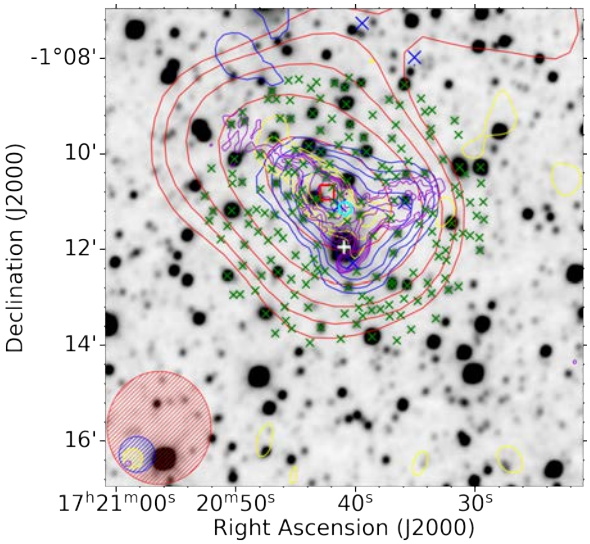

(B) G4Jy 1403

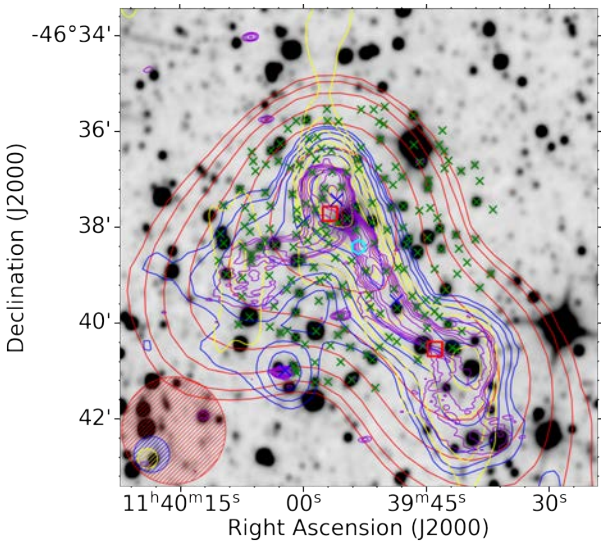

(C) G4Jy 935

FIGURE B.1: Radio sources with head tail morphology in the G4Jy subset.The radio contours are from GLEAM (170 - 231 MHz; red), NVSS (1.4 GHz; blue), TGSS (150 MHz; yellow) and MeerKAT (1.3 GHz; purple), overlaid on the inverted grayscale WISE (3.4 μm) image. The contour levels are $[3, 6, 12, 24, ..] \times \sigma$, where σ is the local rms. Shown in the bottom left corner is the beam size for each survey; GLEAM (red), NVSS(blue), TGSS (yellow) and MeerKAT (purple). The green crosses ('x') are the positions from AllWISE within 3 arcmin of the brightness-weighted centroid position (cyan hexagon), and the white '+' sign is the AllWISE position of the identified host galaxy. The white diamond is the 6dFGS position, the red square is the GLEAM component position, and the blue crosses are positions of NVSS components.

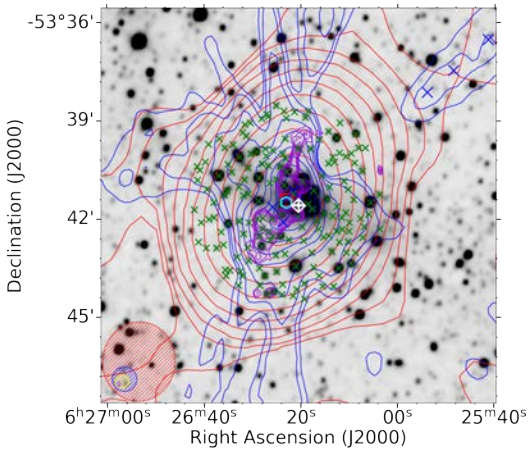

(A) G4Jy 611

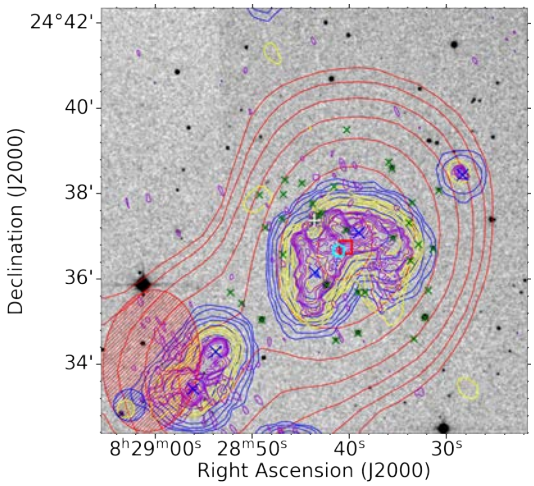

(B) G4Jy 708

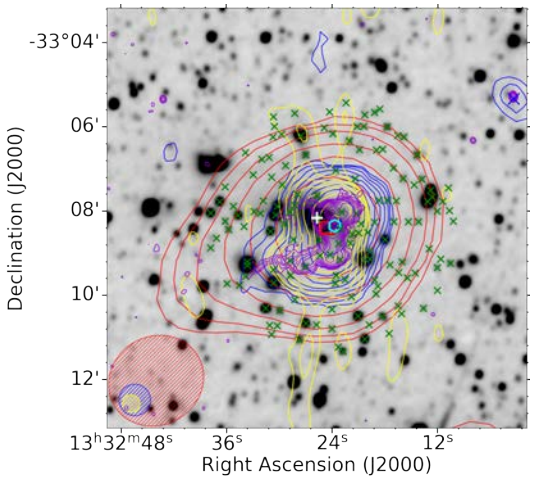

(C) G4Jy 1073

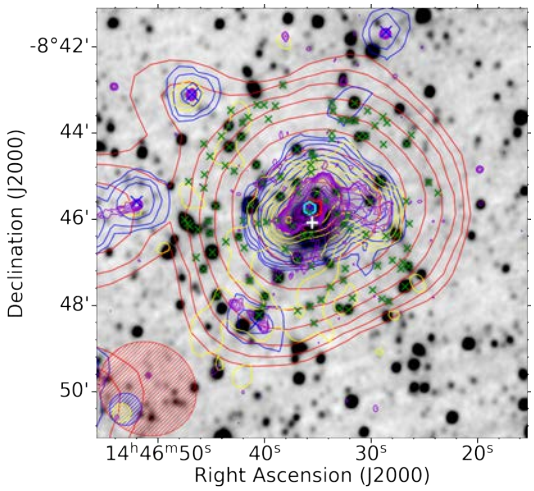

(D) G4Jy 1190

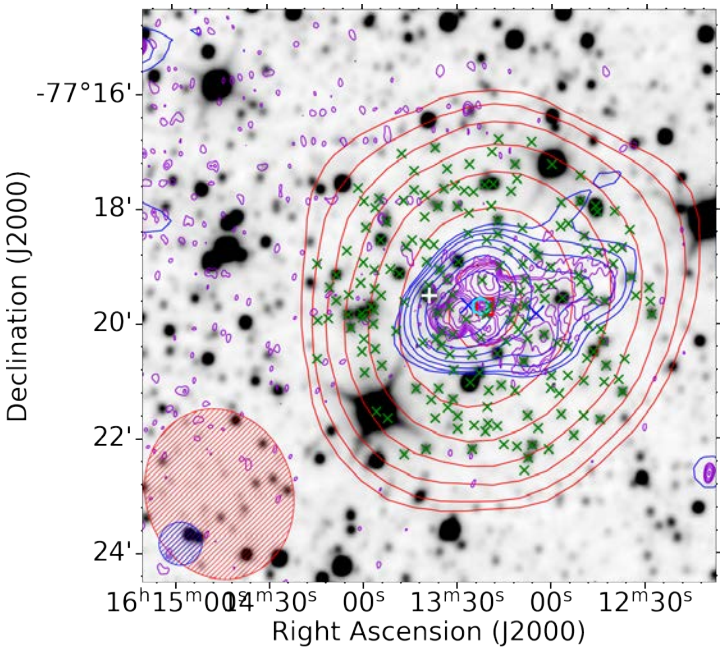

(E) G4Jy 1311

FIGURE B.2: Overlays for radio sources in the G4Jy subset with WAT morphology evident in MeerKAT images. The datasets, symbols, beams and contours are the same as those described in Figure 4.1.

Appendix C

Appendix: Radio sources with single morphology and an identified host galaxy

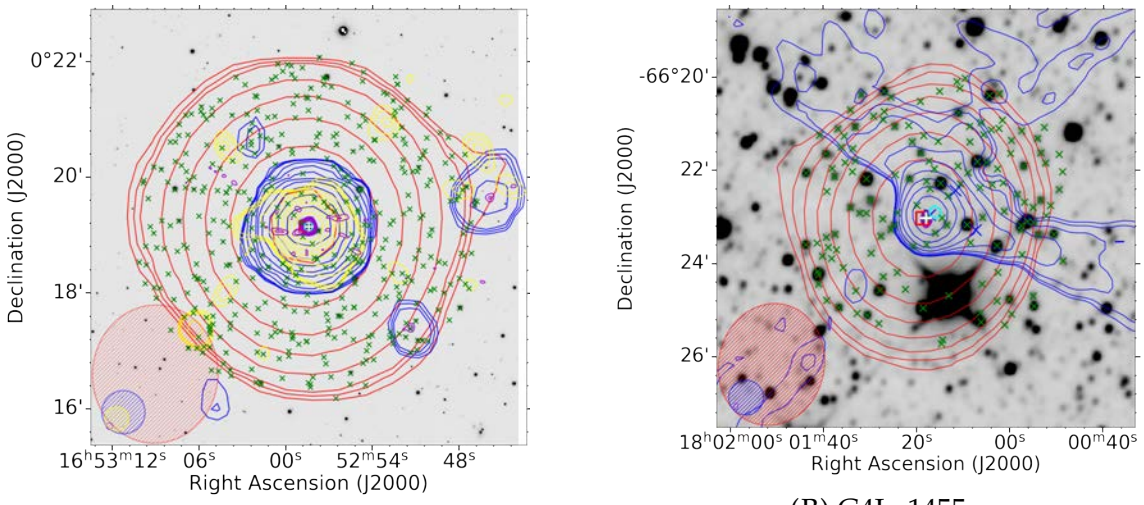

(A) G4Jy 1371

(B) G4Jy 1455

FIGURE C.1: Overlays for radio sources in the G4Jy subset that have 'single' morphology evident in the MeerKAT image and have an identified host galaxy. The datasets, symbols, beams and contours are the same as those described in Figure 4.1.

Appendix D

Appendix: Radio sources with triple morphology and an identified host galaxy

Overlays for radio sources with typical symmetric lobes and have an identified host galaxy

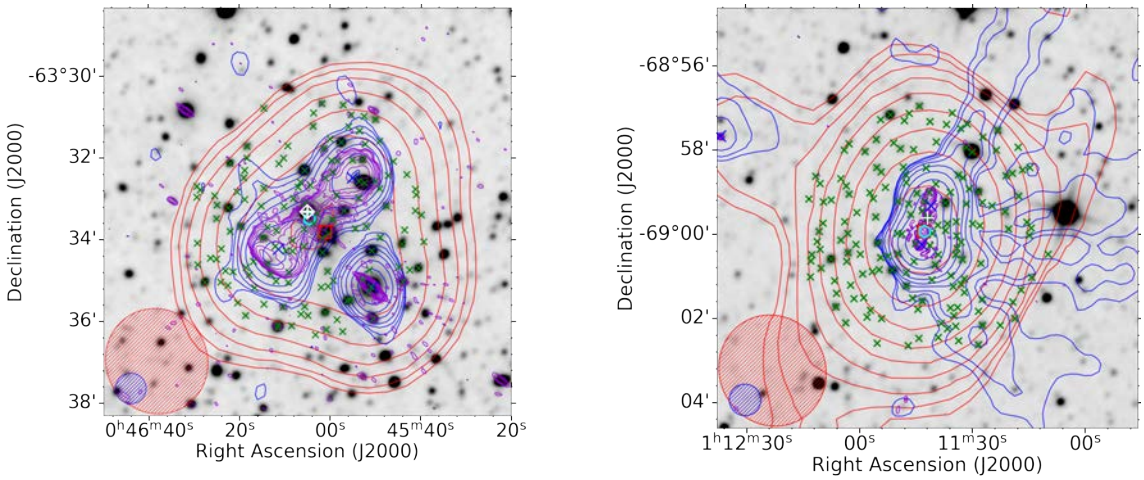

(A) G4Jy 84

(B) G4Jy 129

FIGURE D.1: Overlays of radio sources in the G4Jy subset that have a 'triple' morphology evident in the MeerKAT image and have an identified host galaxy. The datasets, symbols, beams and contours are the same as those described in Figure 4.1.

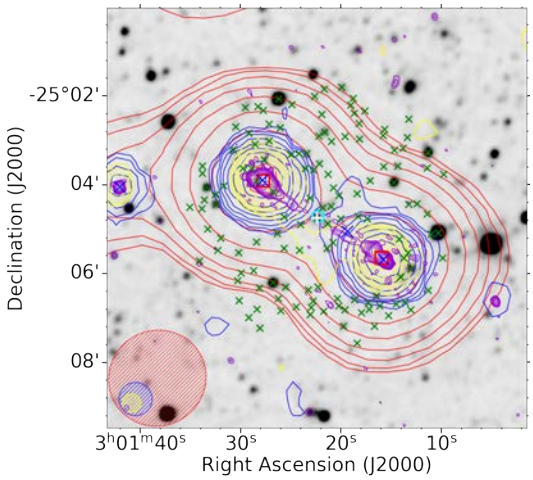

(A) G4Jy 318

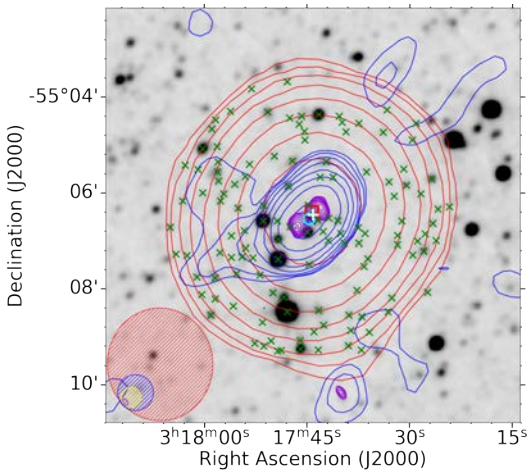

(B) G4Jy 343

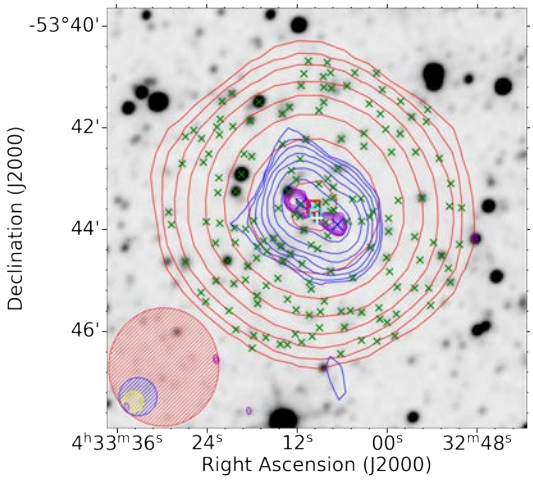

(C) G4Jy 472

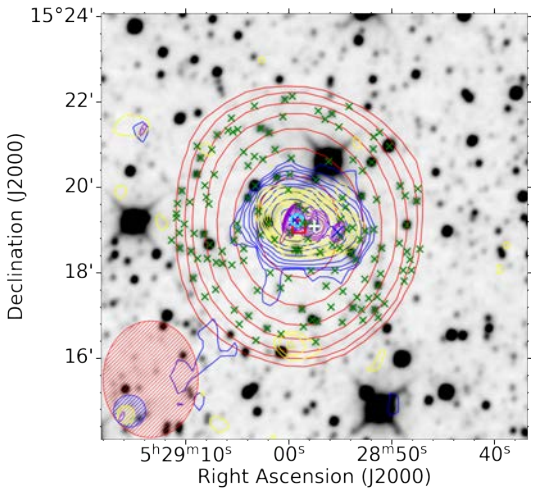

(D) G4Jy 548

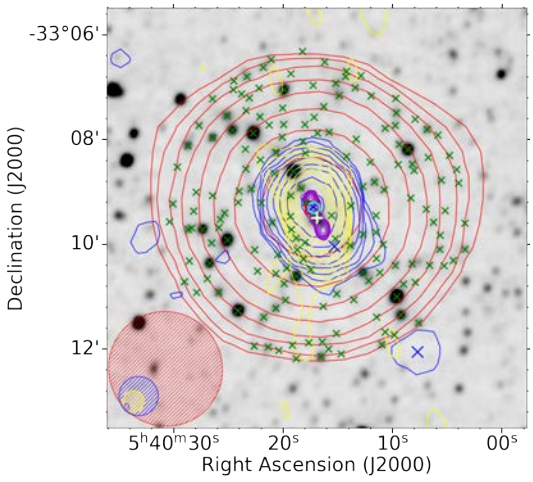

(E) G4Jy 568

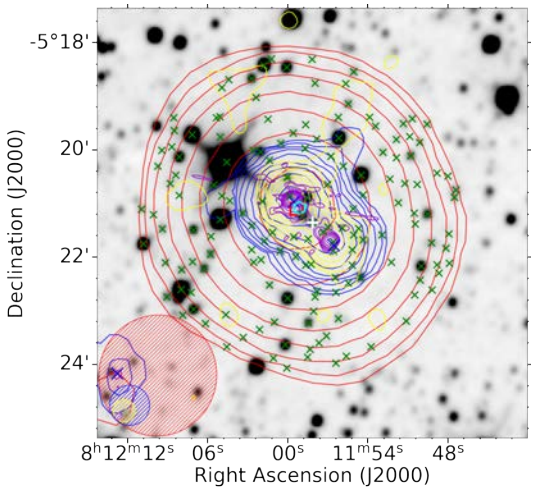

(F) G4Jy 687

FIGURE D.2: Overlays of radio sources in the G4Jy subset that have a 'triple' morphology evident in the MeerKAT image and have an identified host galaxy. The datasets, symbols, beams and contours are the same as those described in Figure 4.1.

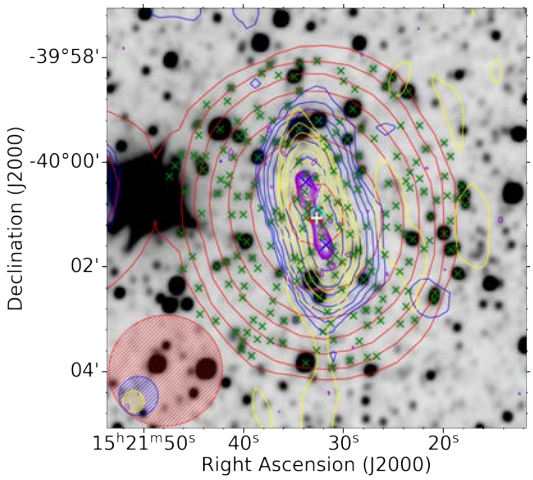

(A) G4Jy 1247

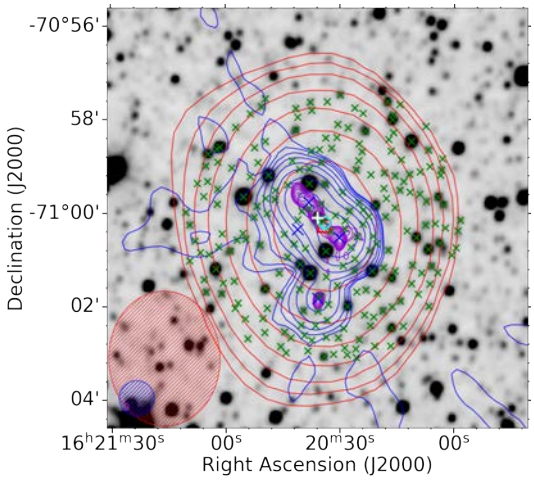

(B) G4Jy 1324

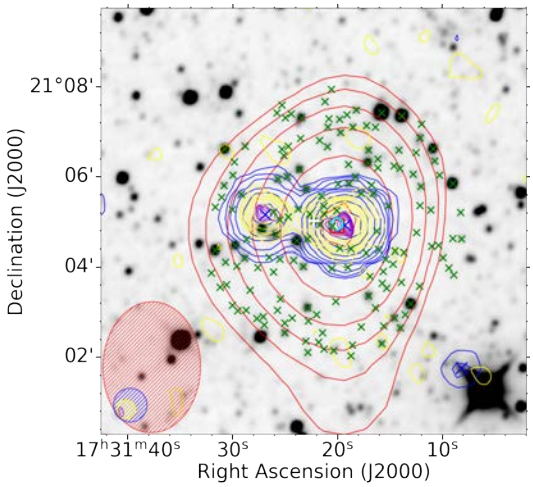

(C) G4Jy 1415

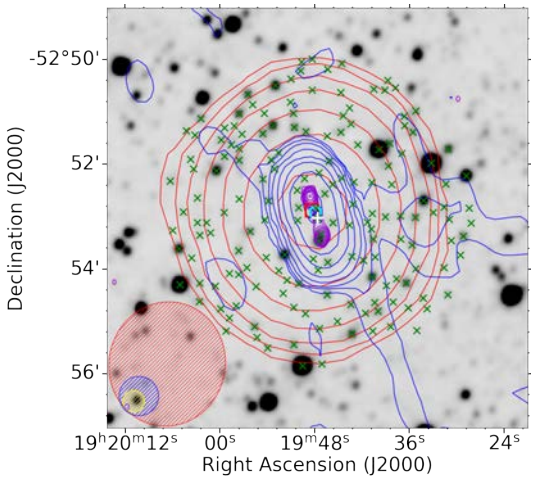

(D) G4Jy 1527

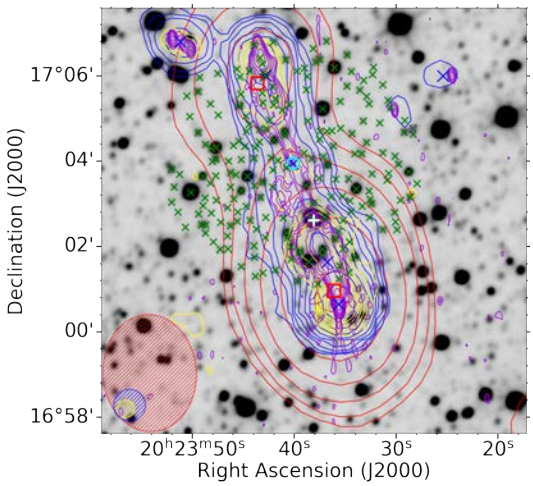

(E) G4Jy 1617

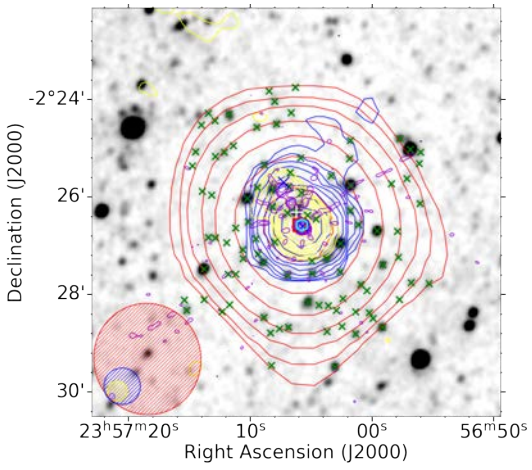

(F) G4Jy 1859

FIGURE D.3: Overlays of radio sources in the G4Jy subset that have a 'triple' morphology evident in the MeerKAT image and have an identified host galaxy. The datasets, symbols, beams and contours are the same as those described in Figure 4.1.

Appendix E

Appendix: Radio sources with double morphology and an identified host galaxy

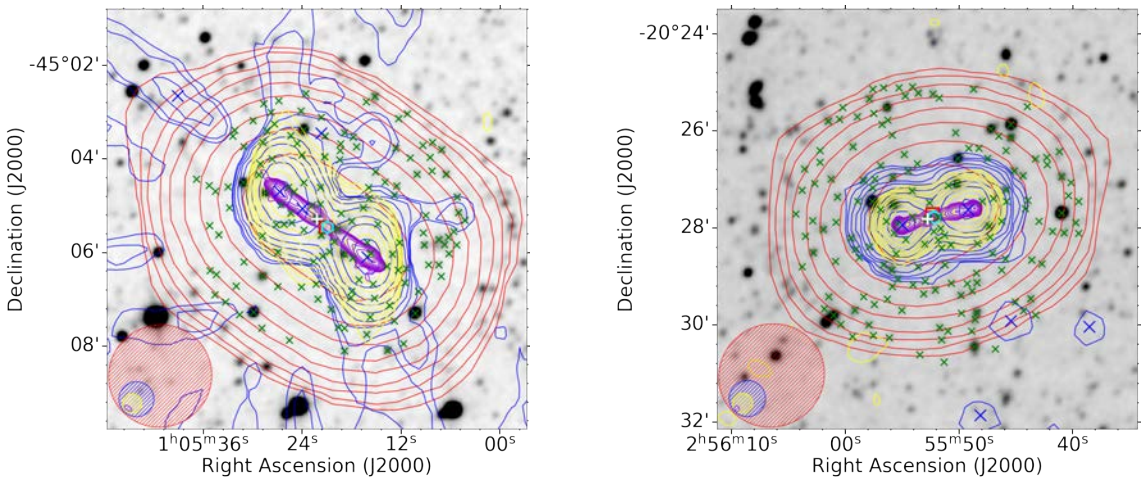

(A) G4Jy 120 (B) G4Jy 311

FIGURE E.1: Overlays of radio sources in the G4Jy subset that have a 'double', extended morphology evident in the MeerKAT image and have an identified host galaxy. The datasets, symbols, beams and contours are the same as those described in Figure 4.1.

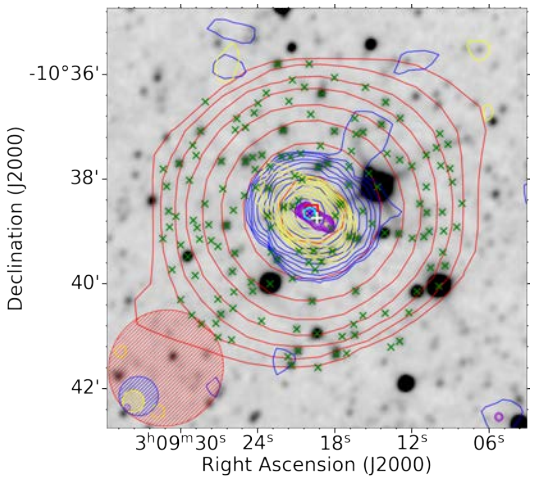

(A) G4Jy 328

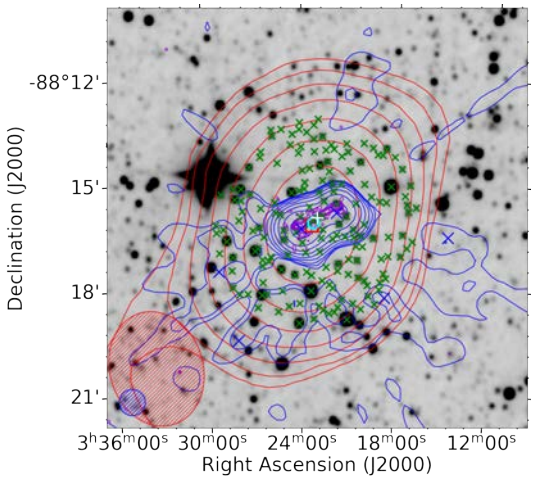

(B) G4Jy 350

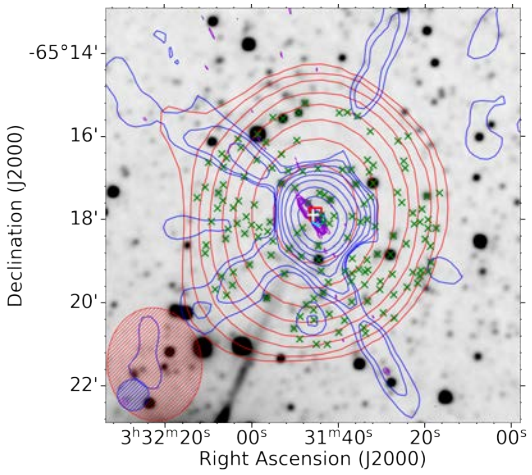

(C) G4Jy 365

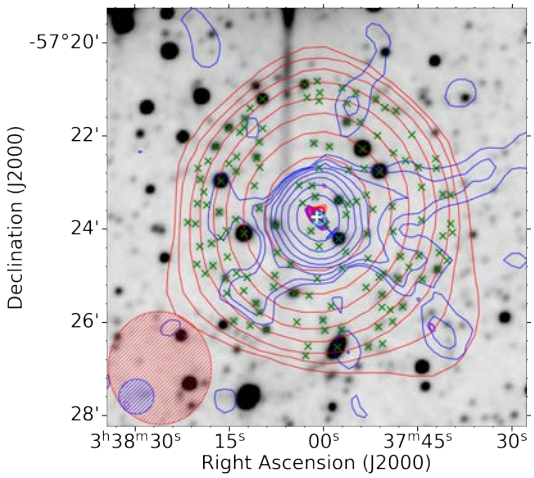

(D) G4Jy 372

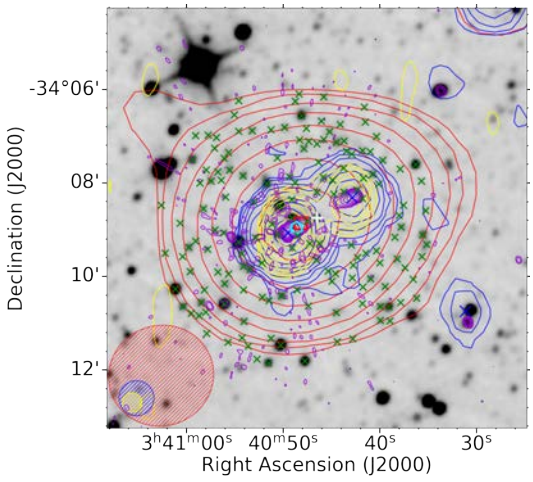

(E) G4Jy 376

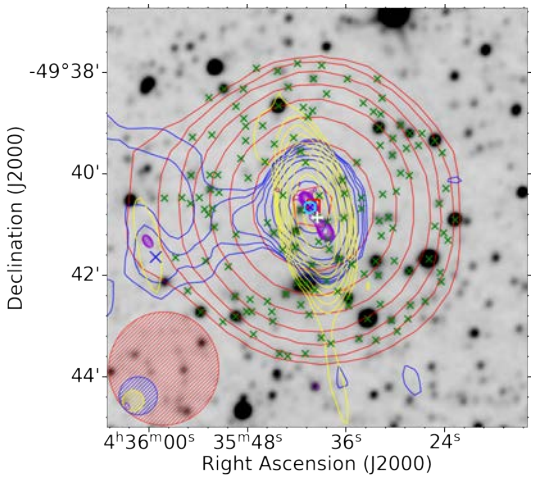

(F) G4Jy 478

FIGURE E.2: Overlays for radio sources in the G4Jy subset that have 'double' morphology evident in the MeerKAT image and have an identified host galaxy. The datasets, symbols, beams and contours are the same as those described in Figure 4.1.

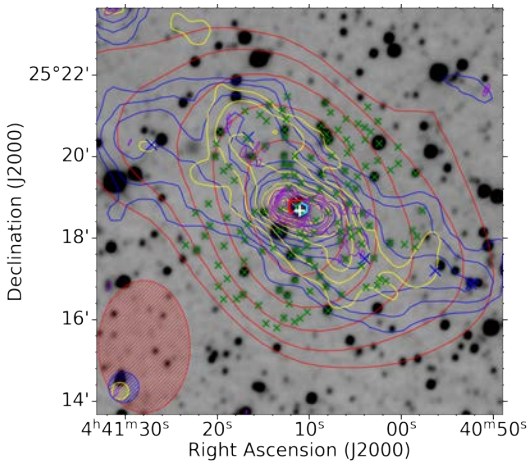

(A) G4Jy 488

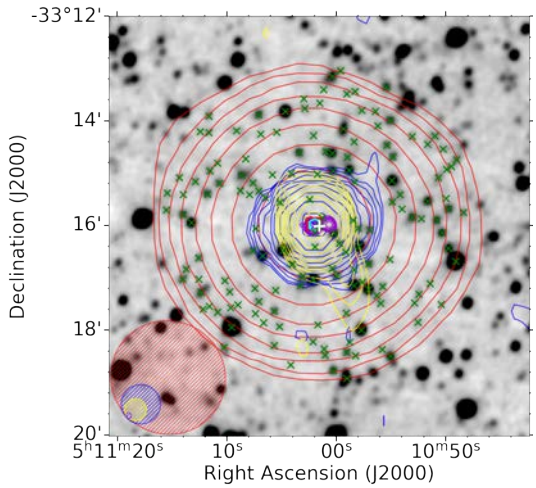

(B) G4Jy 526

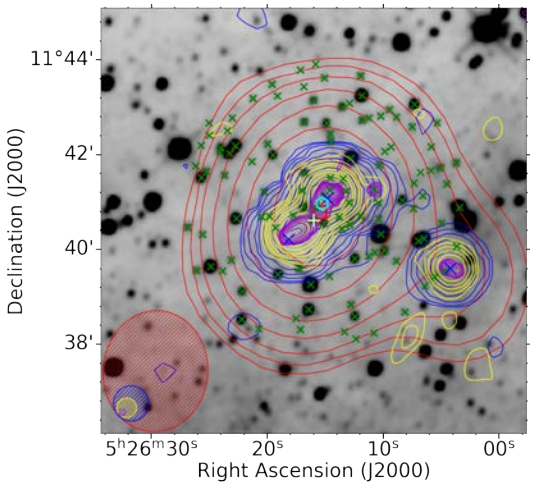

(C) G4Jy 545

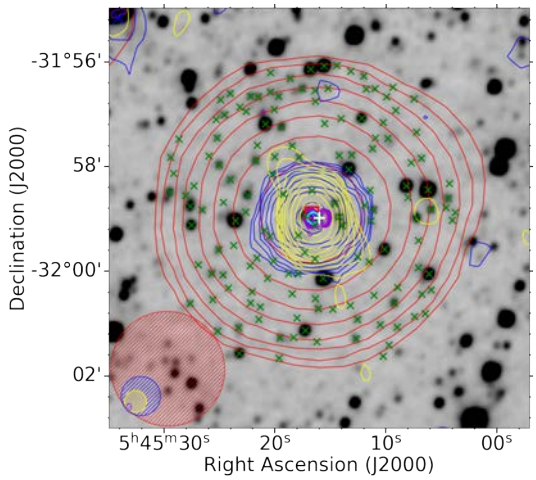

(D) G4Jy 573

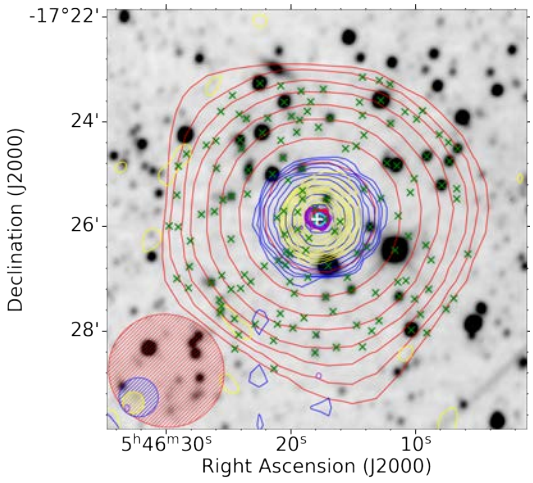

(E) G4Jy 575

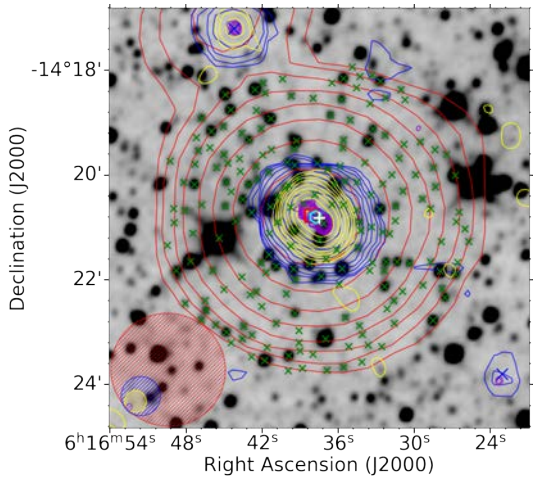

(F) G4Jy 601

FIGURE E.3: Overlays for radio sources in the G4Jy subset that have 'double' morphology evident in the MeerKAT image and have an identified host galaxy. The datasets, symbols, beams and contours are the same as those described in Figure 4.1.

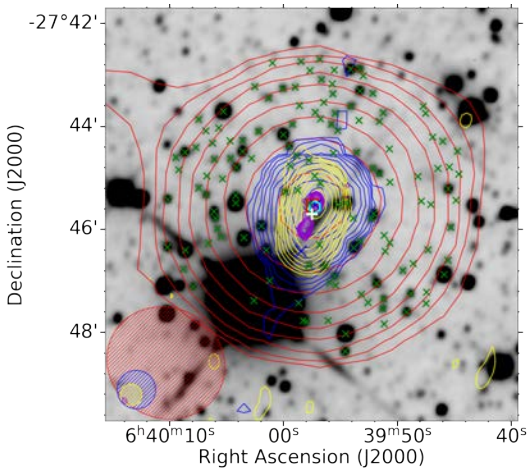

(A) G4Jy 623

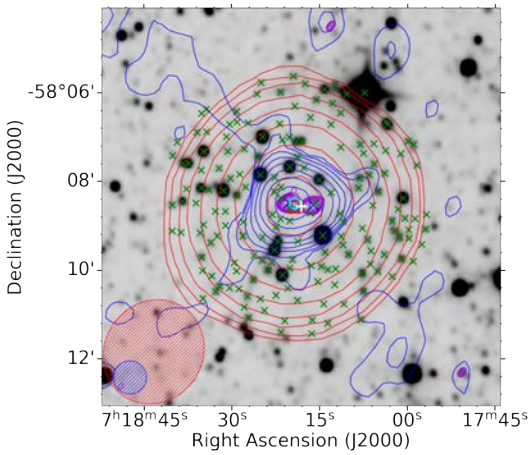

(B) G4Jy 652

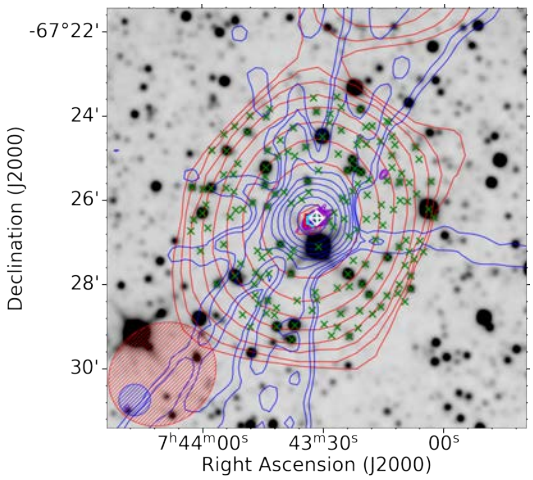

(C) G4Jy 672

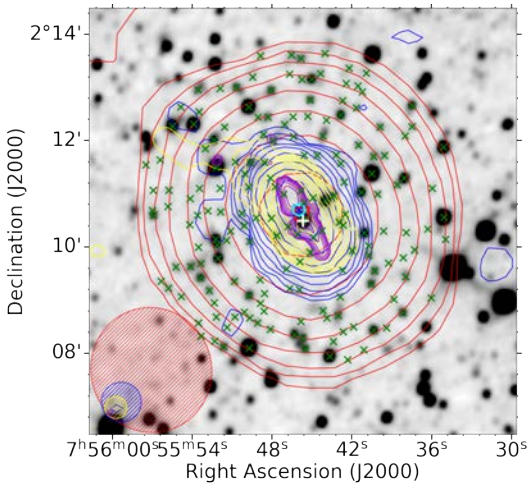

(D) G4Jy 677

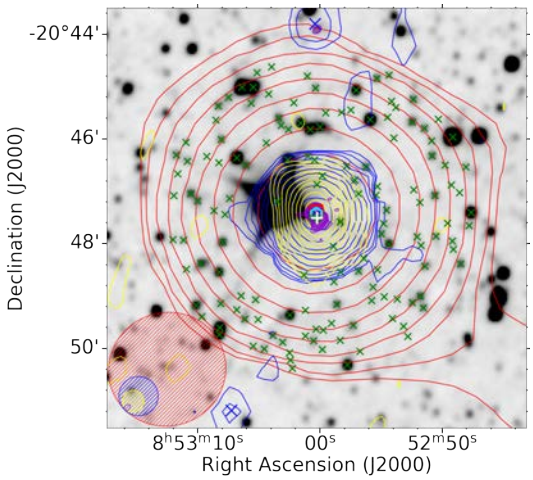

(E) G4Jy 730

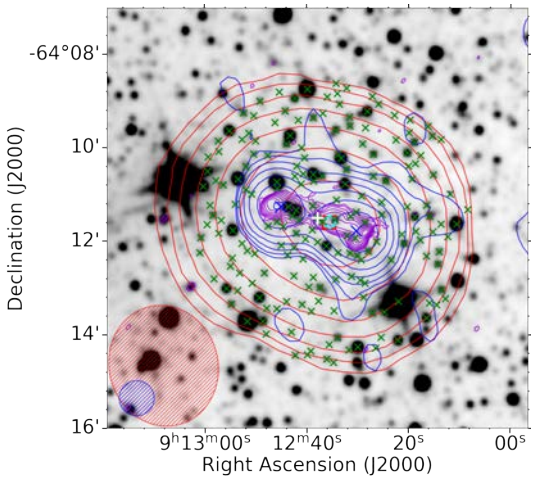

(F) G4Jy 758

FIGURE E.4: Overlays for radio sources in the G4Jy subset that have 'double' morphology evident in the MeerKAT image and have an identified host galaxy. The datasets, symbols, beams and contours are the same as those described in Figure 4.1.

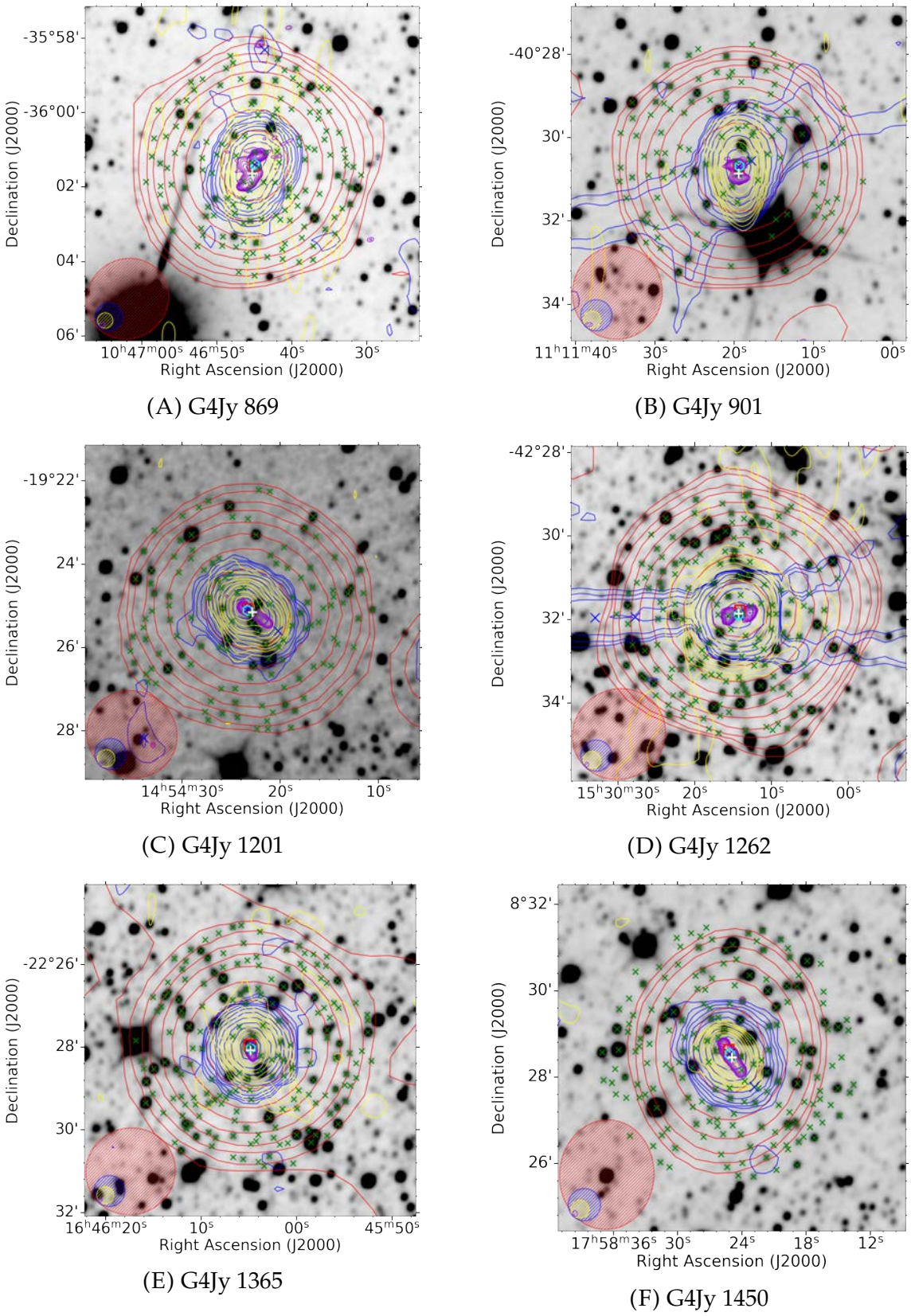

(A) G4Jy 869

(B) G4Jy 901

(C) G4Jy 1201

(D) G4Jy 1262

(E) G4Jy 1365

(F) G4Jy 1450

FIGURE E.5: Overlays for radio sources in the G4Jy subset that have 'double' morphology evident in the MeerKAT image and have an identified host galaxy. The datasets, symbols, beams and contours are the same as those described in Figure 4.1.

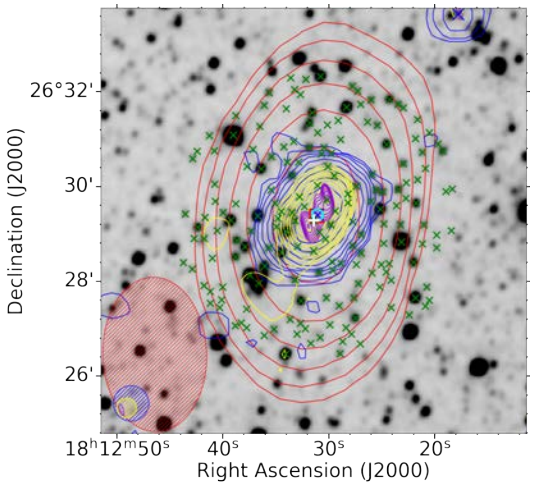

(A) G4Jy 1468

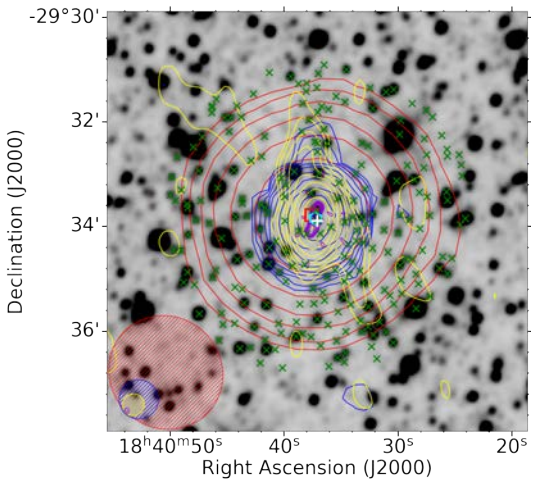

(B) G4Jy 1501

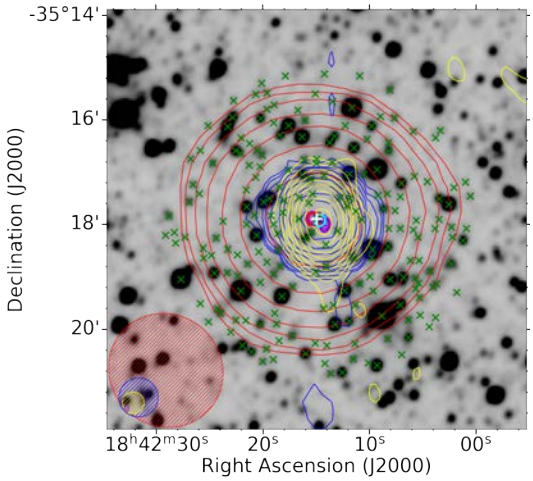

(C) G4Jy 1503

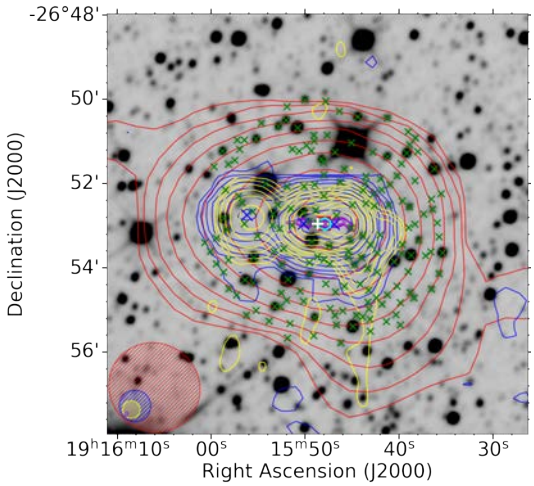

(D) G4Jy 1518

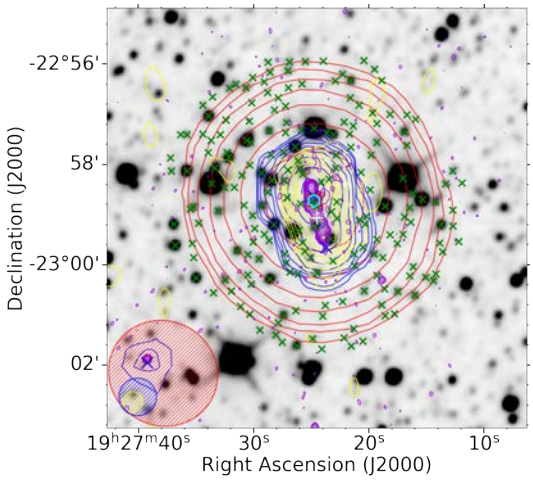

(E) G4Jy 1540

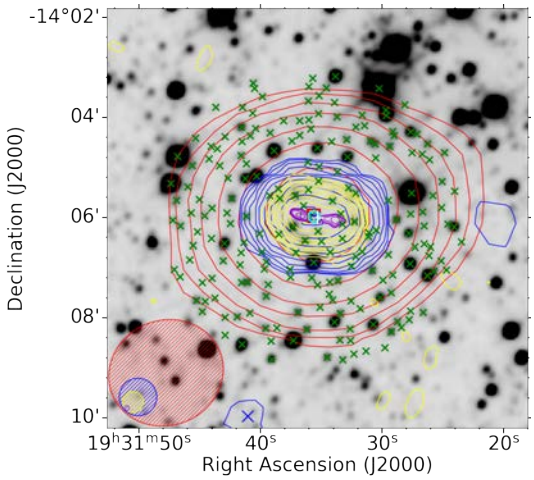

(F) G4Jy 1548

FIGURE E.6: Overlays for radio sources in the G4Jy subset that have 'double' morphology evident in the MeerKAT image and have an identified host galaxy. The datasets, symbols, beams and contours are the same as those described in Figure 4.1.

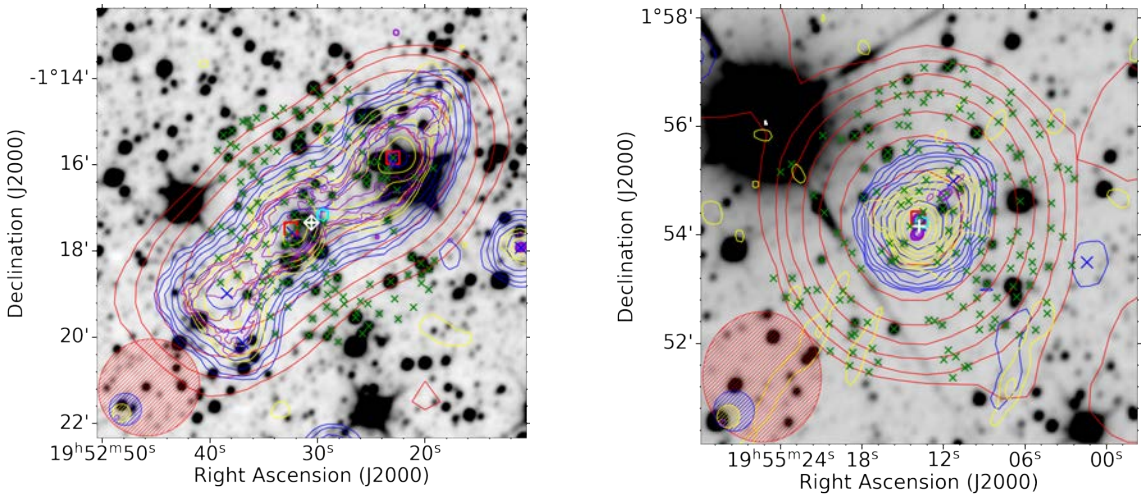

(A) G4Jy 1582

(B) G4Jy 1585

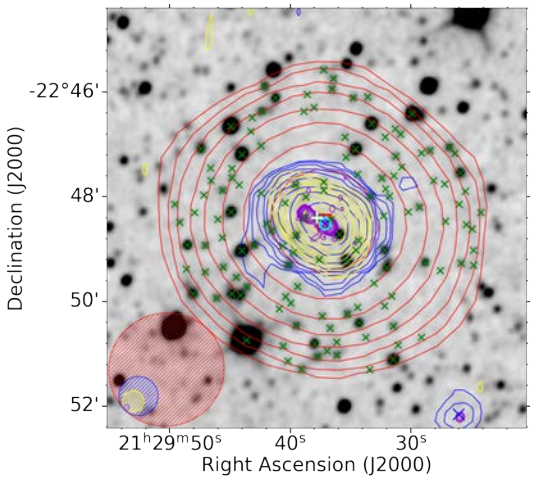

(C) G4Jy 1697

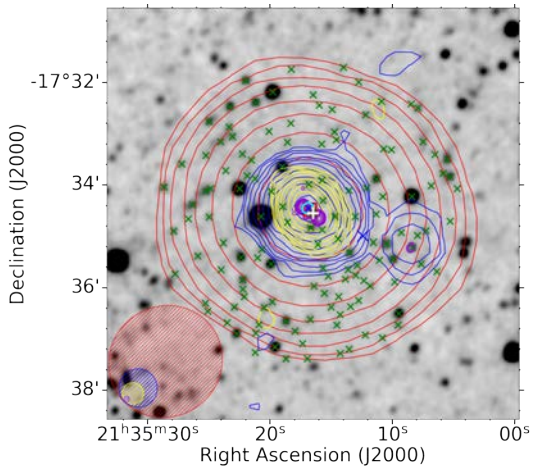

(D) G4Jy 1706

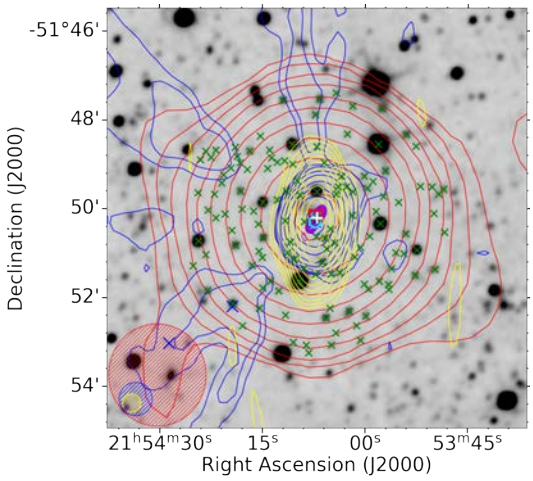

(E) G4Jy 1740

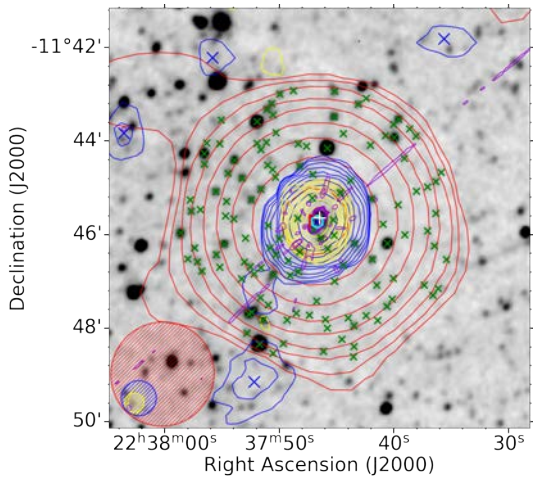

(F) G4Jy 1784

FIGURE E.7: Overlays for radio sources in the G4Jy subset that have 'double' morphology evident in the MeerKAT image and have an identified host galaxy. The datasets, symbols, beams and contours are the same as those described in Figure 4.1.

Appendix F

Appendix: Sources with double morphology and no identified host galaxy

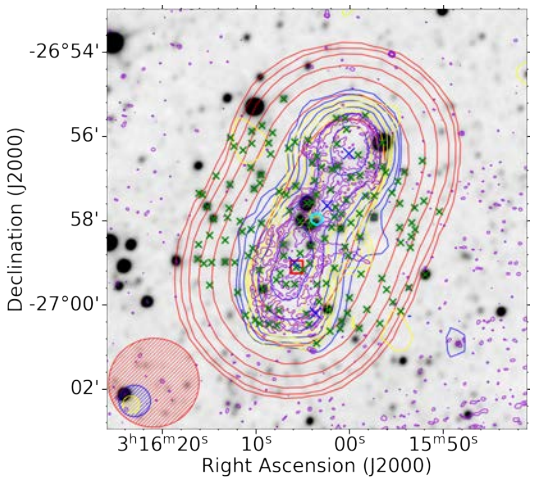

(A) G4Jy 338

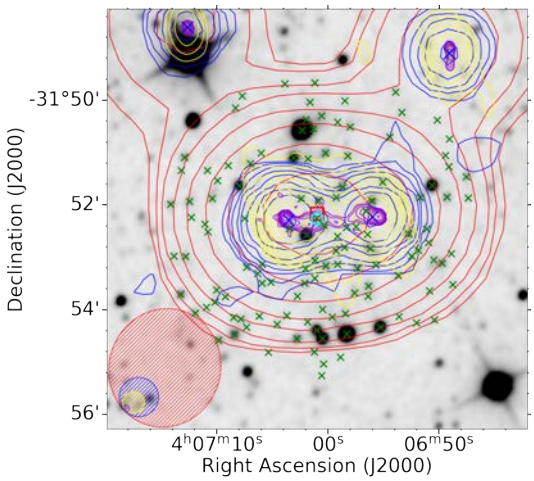

(B) G4Jy 413

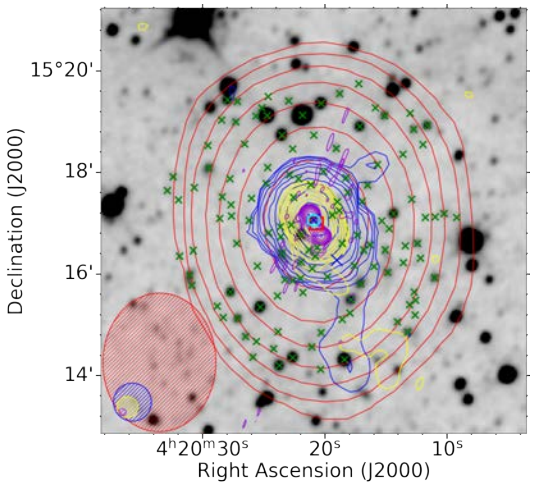

(C) G4Jy 441

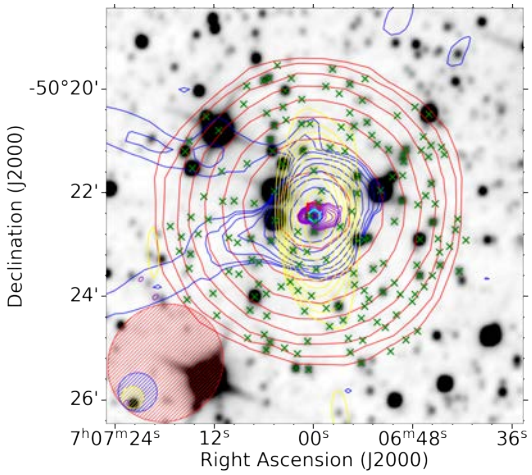

(D) G4Jy 643

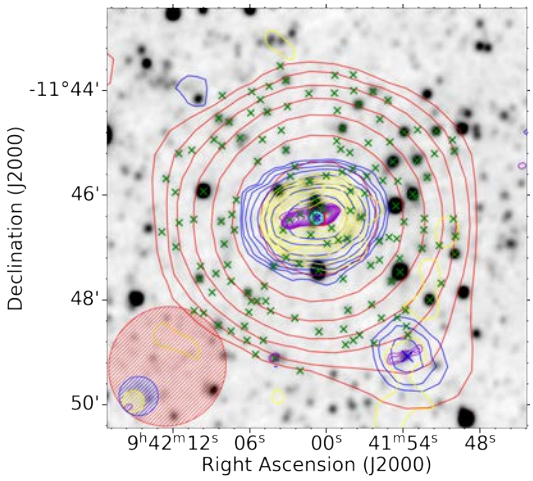

(E) G4Jy 781

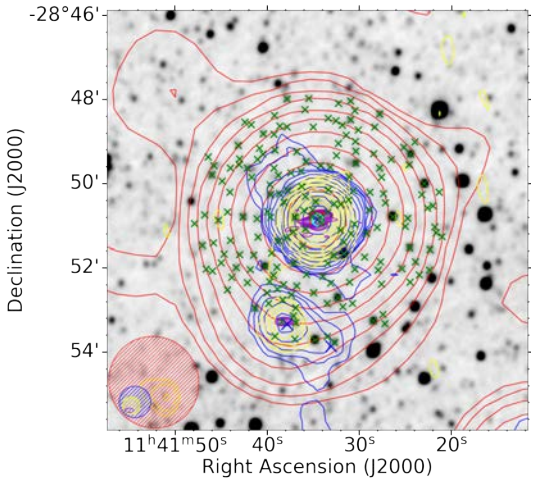

(F) G4Jy 939

FIGURE F.1: Overlays for radio sources in the G4Jy subset with 'double' morphology evident in the MeerKAT images and have no identified host galaxy. The datasets, symbols, beams and contours are the same as those described in Figure 4.1.

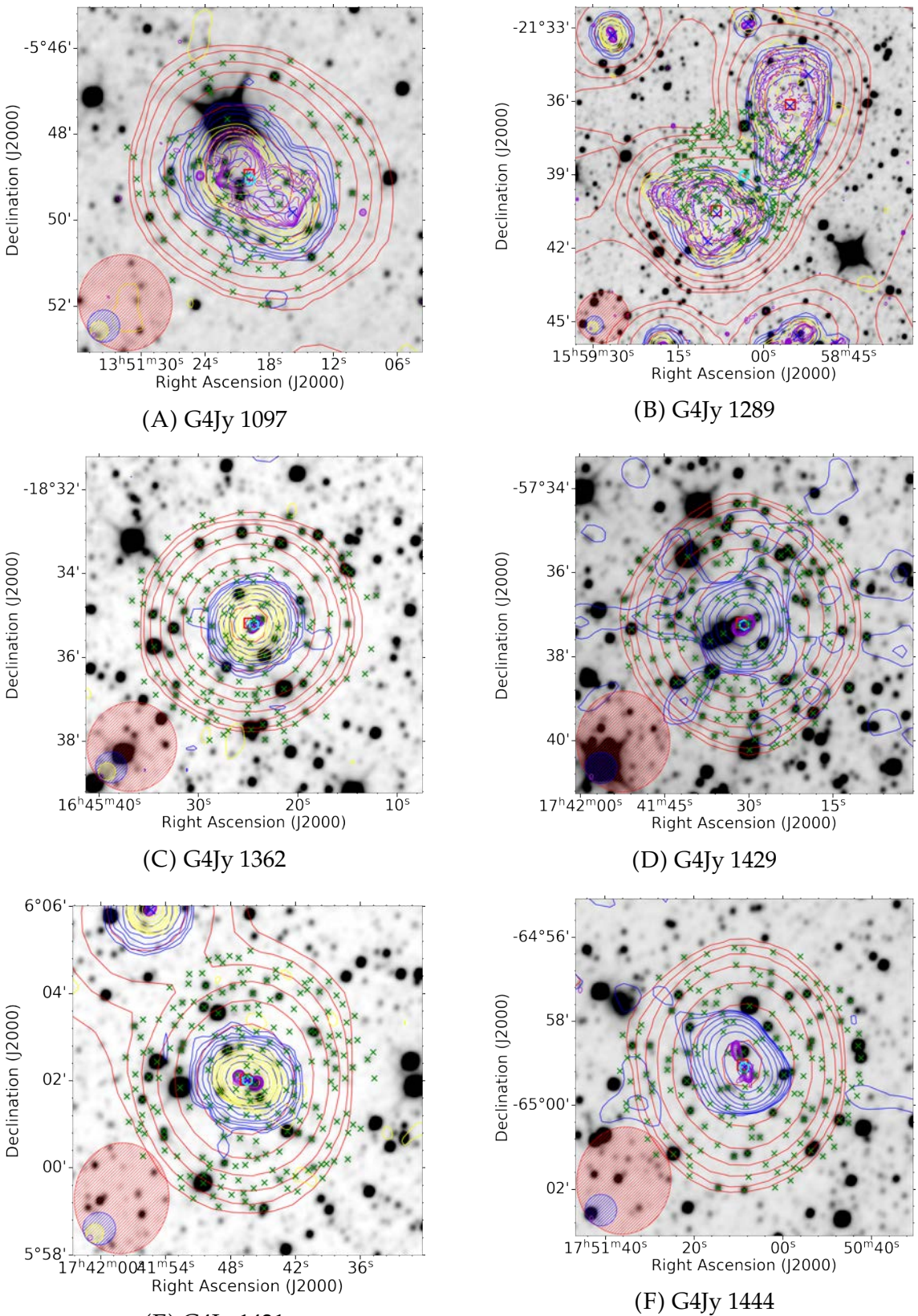

(A) G4Jy 1097

(B) G4Jy 1289

(C) G4Jy 1362

(D) G4Jy 1429

(E) G4Jy 1431

(F) G4Jy 1444

FIGURE F.2: Overlays of radio sources in the G4Jy subset with 'double' morphology evident in the MeerKAT images and have no identified host galaxy. The datasets, symbols, beams and contours are the same as those described in Figure 4.1.

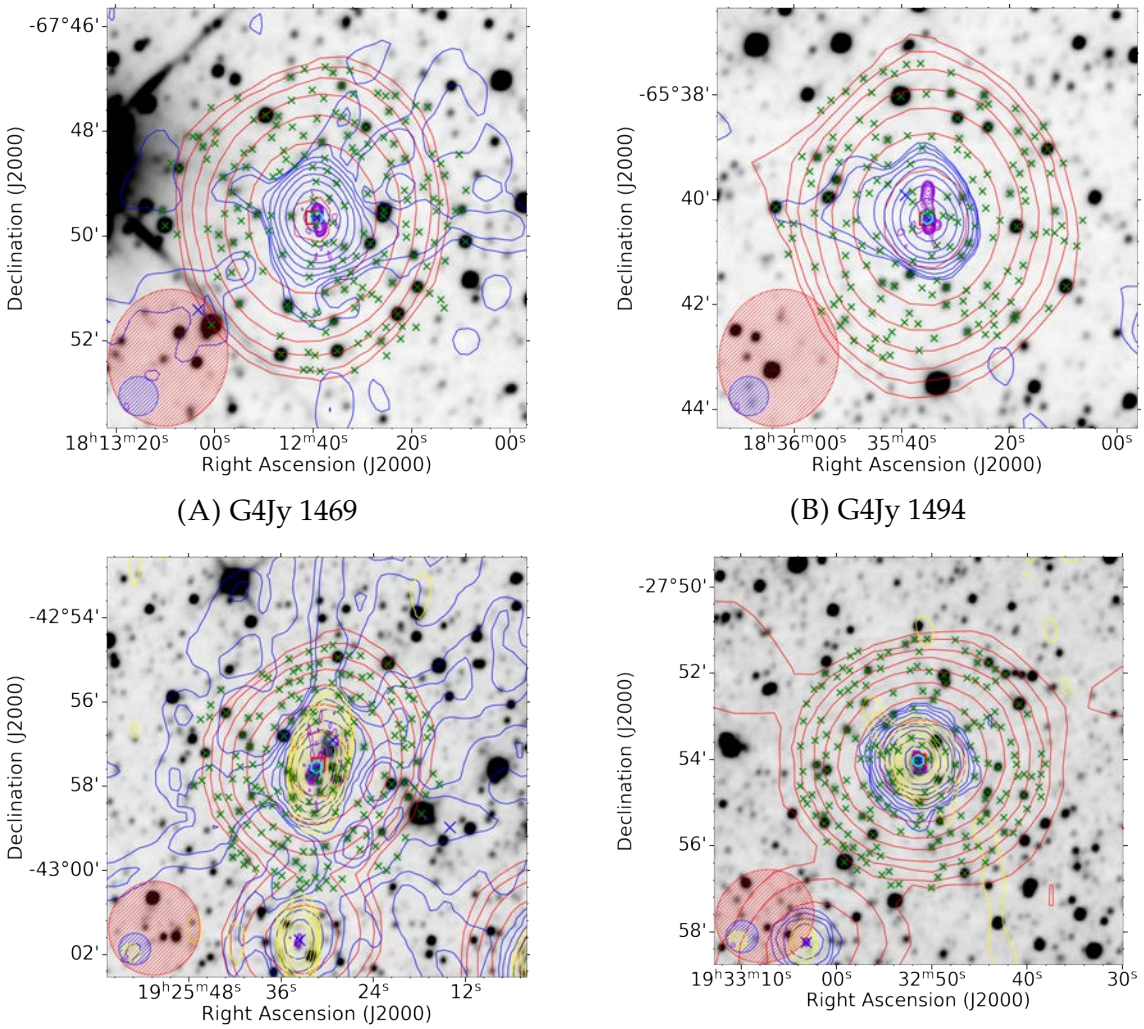

(A) G4Jy 1469

(B) G4Jy 1494

(C) G4Jy 1534

(D) G4Jy 1553

FIGURE F.3: Overlays of radio sources in the G4Jy subset with 'double' morphology evident in the MeerKAT images and have no identified host galaxy. The datasets, symbols, beams and contours are the same as those described in Figure 4.1.

Appendix G

Appendix: Sources with faint mid-infrared host

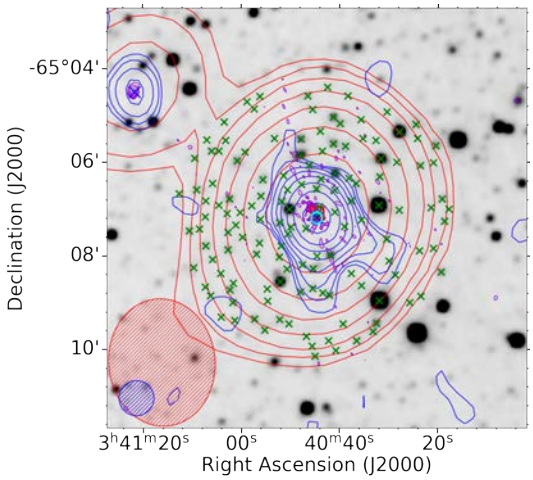

(A) G4Jy 375

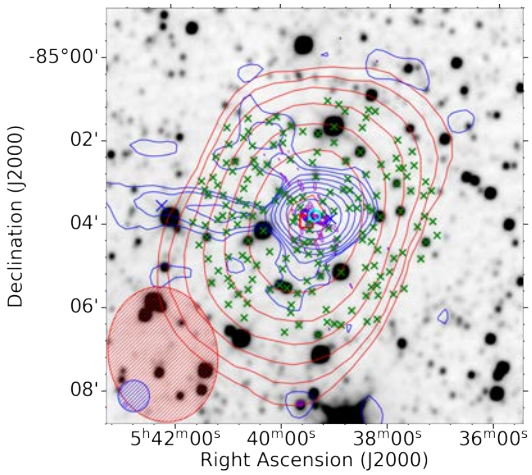

(B) G4Jy 566

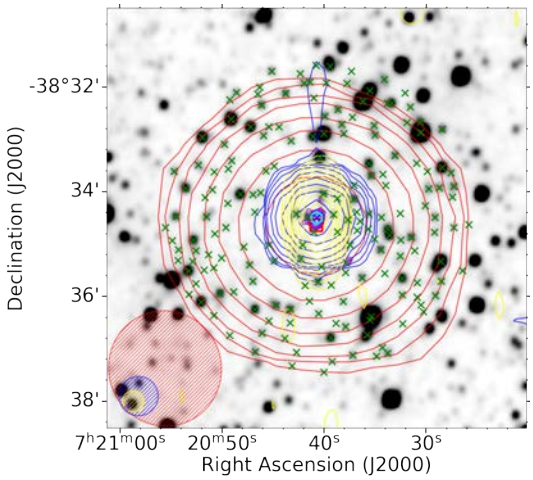

(C) G4Jy 654

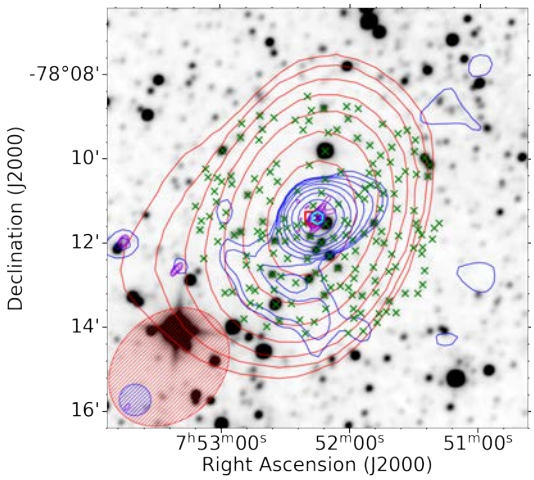

(D) G4Jy 676

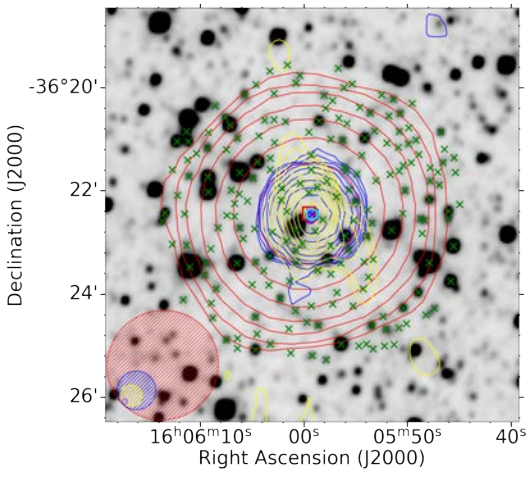

(E) G4Jy 1305

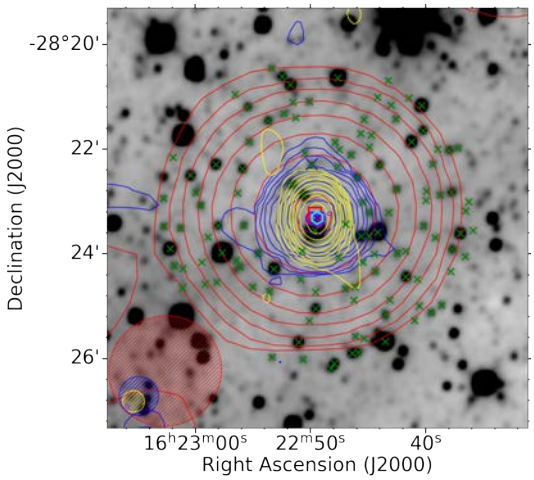

(F) G4Jy 1329

FIGURE G.1: Overlays of candidate IFRS in the G4Jy subset. The datasets, symbols, beams and contours are the same as those described in Figure 4.1.

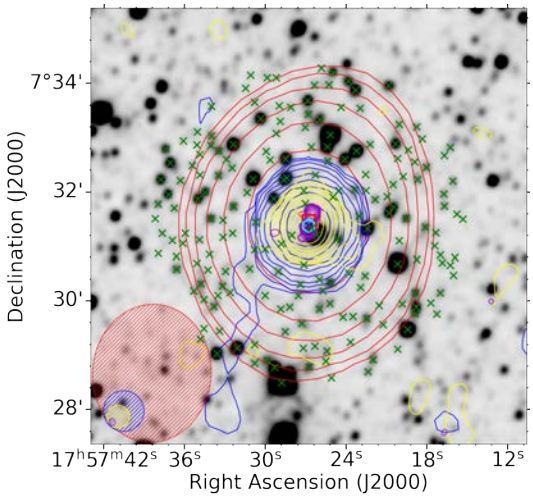

(A) G4Jy 1449

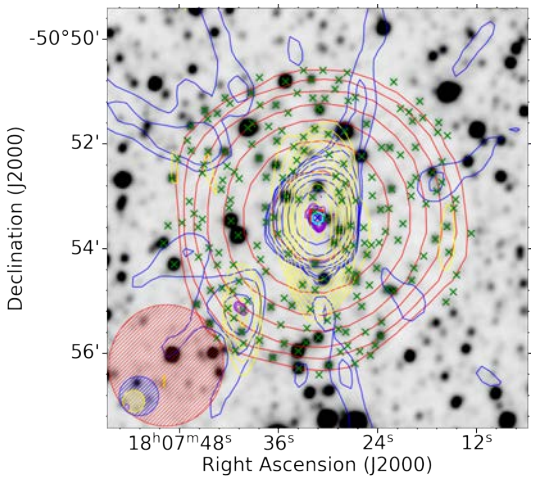

(B) G4Jy 1464

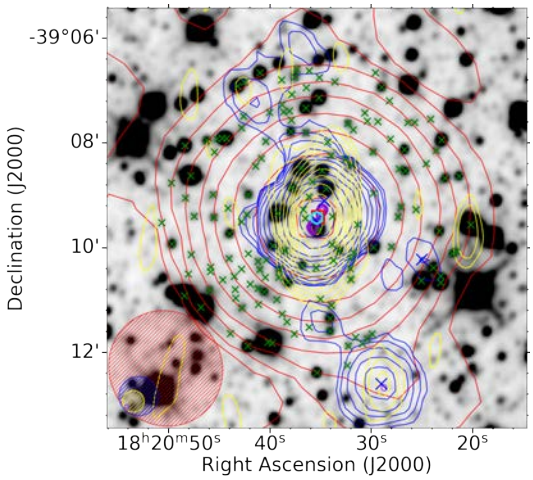

(C) G4Jy 1474

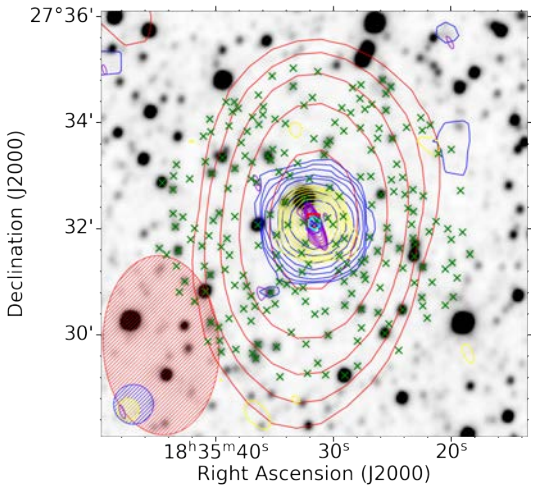

(D) G4Jy 1493

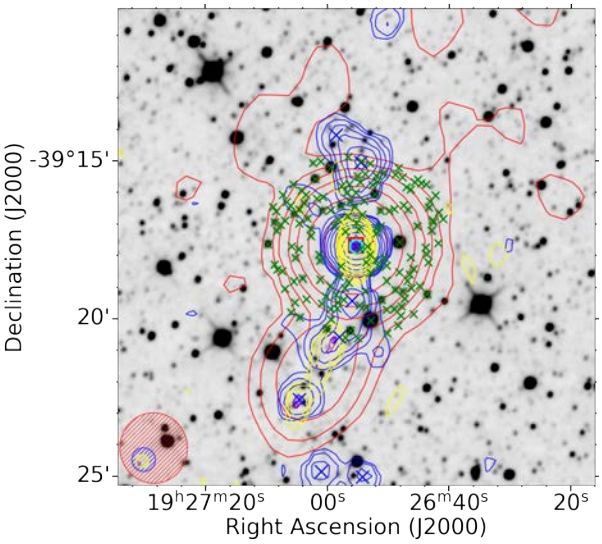

(E) G4Jy 1539

FIGURE G.2: Candidate IFRS in the G4Jy subset. The datasets, symbols, beams and contours are the same as those described in Figure 4.1.

Appendix H

Appendix: Sources with complex morphology

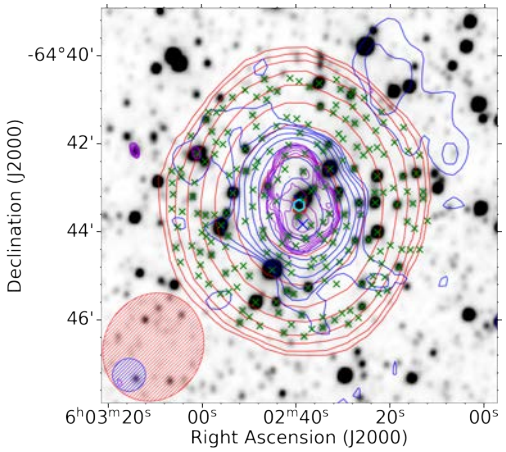

(A) G4Jy 587

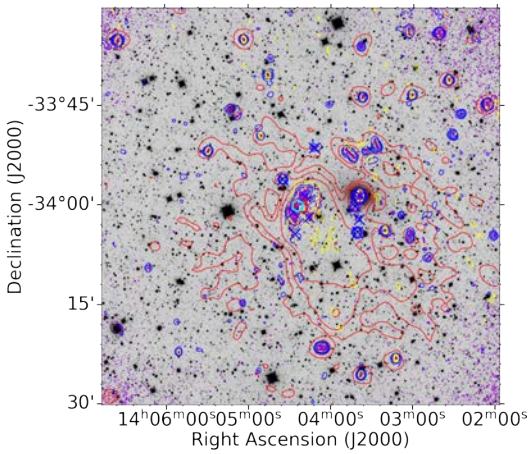

(B) G4Jy 1117

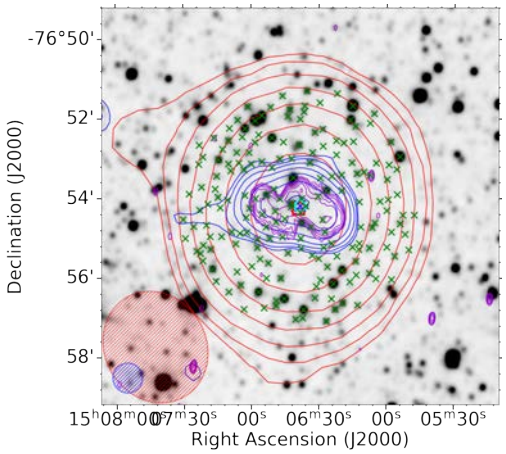

(C) G4Jy 1220

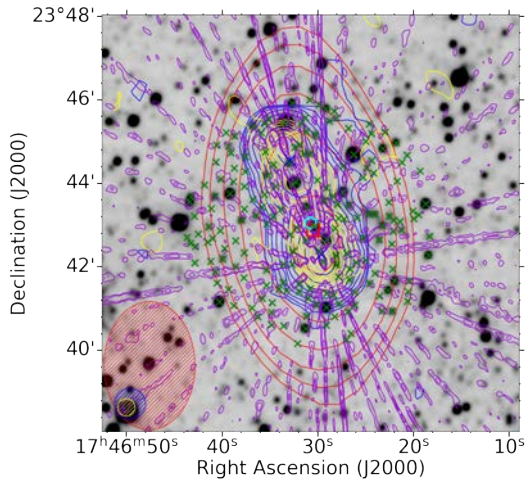

(D) G4Jy 1438

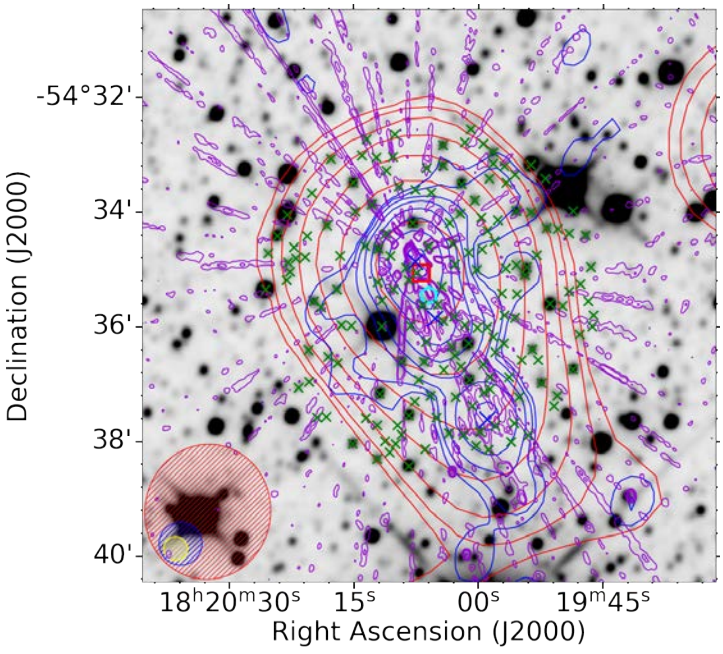

(E) G4Jy 1473

FIGURE H.1: Overlays of radio sources in the G4Jy subset with 'complex' morphology. The datasets, symbols, beams and contours are the same as those described in Figure 4.1.

Bibliography

Abazajian, Kevork N. et al. (June 2009). "The Seventh Data Release of the Sloan Digital Sky Survey". In: *ApJS* 182.2, pp. 543–558. DOI: 10.1088/0067-0049/182/2/543. arXiv: 0812.0649 [astro-ph].

Aird, J. et al. (Feb. 2010). "The evolution of the hard X-ray luminosity function of AGN". In: *MNRAS* 401.4, pp. 2531–2551. DOI: 10.1111/j.1365-2966.2009.15829.x. arXiv: 0910.1141 [astro-ph.CO].

Alam, Shadab et al. (July 2015). "The Eleventh and Twelfth Data Releases of the Sloan Digital Sky Survey: Final Data from SDSS-III". In: *ApJS* 219.1, 12, p. 12. DOI: 10.1088/0067-0049/219/1/12. arXiv: 1501.00963 [astro-ph.IM].

Alhassan, Wathela, A. R. Taylor, and Mattia Vaccari (Oct. 2018). "The FIRST Classifier: compact and extended radio galaxy classification using deep Convolutional Neural Networks". In: *MNRAS* 480.2, pp. 2085–2093. DOI: 10.1093/mnras/sty2038. arXiv: 1807.10380 [astro-ph.GA].

Aniyan, Arun and Kshitij Thorat (May 2017). "Classifying Radio Galaxies with Convolutional Neural Network". In: *ApJS* 230. DOI: 10.3847/1538-4365/aa7333.

Asad, K. M. B. et al. (Apr. 2021). "Primary beam effects of radio astronomy antennas - II. Modelling MeerKAT L-band beams". In: *MNRAS* 502.2, pp. 2970–2983. DOI: 10.1093/mnras/stab104. arXiv: 1904.07155 [astro-ph.IM].

Bahcall, John N. et al. (Apr. 1997). "Hubble Space Telescope Images of a Sample of 20 Nearby Luminous Quasars". In: *ApJ* 479.2, pp. 642–658. DOI: 10.1086/303926. arXiv: astro-ph/9611163 [astro-ph].

Banfield, J. K. et al. (2015). "Radio Galaxy Zoo: Host galaxies and radio morphologies derived from visual inspection". In: *MNRAS* 453.3, pp. 2326–2340. ISSN: 13652966. DOI: 10.1093/mnras/stv1688. arXiv: 1507.07272.

Barkus, B. et al. (Jan. 2022). "The application of ridgelines in extended radio source cross-identification". In: *MNRAS* 509.1, pp. 1–15. DOI: 10.1093/mnras/stab2952. arXiv: 2110.05254 [astro-ph.GA].

Becker, Burger et al. (May 2021). "CNN architecture comparison for radio galaxy classification". In: *MNRAS* 503.2, pp. 1828–1846. DOI: 10.1093/mnras/stab325. arXiv: 2102.03780 [astro-ph.GA].

Best, P. N. and T. M. Heckman (Apr. 2012). "On the fundamental dichotomy in the local radio-AGN population: accretion, evolution and host galaxy properties". In:

MNRAS 421.2, pp. 1569–1582. DOI: 10.1111/j.1365-2966.2012.20414.x. arXiv: 1201.2397 [astro-ph.CO].

Blandford, R. D. and A. Königl (Aug. 1979). "Relativistic jets as compact radio sources." In: *ApJ* 232, pp. 34–48. DOI: 10.1086/157262.

Bliton, M. et al. (Dec. 1998). "Cluster-subcluster mergers and the formation of narrow-angle tailed radio sources". In: *MNRAS* 301.3, pp. 609–625. ISSN: 0035-8711. DOI: 10.1111/j.1365-8711.1998.01973.x. eprint: https://academic.oup.com/mnras/article-pdf/301/3/609/3498816/301-3-609.pdf. URL: https://doi.org/10.1111/j.1365-8711.1998.01973.x.

Bock, D. C. J., M. I. Large, and Elaine M. Sadler (Mar. 1999). "SUMSS: A Wide-Field Radio Imaging Survey of the Southern Sky. I. Science Goals, Survey Design, and Instrumentation". In: *AJ* 117.3, pp. 1578–1593. DOI: 10.1086/300786. arXiv: astro-ph/9812083 [astro-ph].

Boué, G. et al. (Feb. 2008). "The galaxy luminosity function of the Abell 496 cluster and its spatial variations". In: *A&A* 479.2, pp. 335–346. DOI: 10.1051/0004-6361:20077723. arXiv: 0711.4951 [astro-ph].

Briggs, D. S. (Dec. 1995). "High Fidelity Interferometric Imaging: Robust Weighting and NNLS Deconvolution". In: *American Astronomical Society Meeting Abstracts*. Vol. 187. American Astronomical Society Meeting Abstracts, p. 112.02.

Buckley, David A. H., Gerhard P. Swart, and Jacobus G. Meiring (June 2006). "Completion and commissioning of the Southern African Large Telescope". In: *Society of Photo-Optical Instrumentation Engineers (SPIE) Conference Series*. Ed. by Larry M. Stepp. Vol. 6267. Society of Photo-Optical Instrumentation Engineers (SPIE) Conference Series, 62670Z. DOI: 10.1117/12.673750.

Burgess, A. M. and R. W. Hunstead (Jan. 2006). "The Molonglo Southern 4 Jy Sample (MS4). II. ATCA Imaging and Optical Identification". In: *AJ* 131.1, pp. 114–132. DOI: 10.1086/498679. URL: https://doi.org/10.1086/498679.

Capetti, A. et al. (Oct. 2002). "On the origin of X-shaped radio-sources: New insights from the properties of their host galaxies". In: *A&A* 394, pp. 39–45. DOI: 10.1051/0004-6361:20021070. arXiv: astro-ph/0207333 [astro-ph].

Carilli, C. L. and P. D. Barthel (Jan. 1996). "Cygnus A". In: *A&ARv* 7.1, pp. 1–54. DOI: 10.1007/s001590050001.

Chambers, K. C. et al. (2019). *The Pan-STARRS1 Surveys*. arXiv: 1612.05560 [astro-ph.IM].

Colless, M. et al. (Dec. 2007). "Luminosity and Stellar Mass Functions from the 6dF Galaxy Survey". In: *Cosmic Frontiers*. Ed. by N. Metcalfe and T. Shanks. Vol. 379. Astronomical Society of the Pacific Conference Series, p. 126.

Colless, Matthew et al. (Dec. 2001). "The 2dF Galaxy Redshift Survey: spectra and redshifts". In: *MNRAS* 328.4, pp. 1039–1063. DOI: 10.1046/j.1365-8711.2001.04902.x. arXiv: astro-ph/0106498 [astro-ph].

Condon, J. J. et al. (May 1998). "The NRAO VLA Sky Survey". In: *AJ* 115.5, pp. 1693–1716. DOI: 10.1086/300337. URL: https://doi.org/10.1086/300337.

Croft, Steve et al. (Aug. 2006). "Minkowski's Object: A Starburst Triggered by a Radio Jet, Revisited". In: *ApJ* 647.2, pp. 1040–1055. DOI: 10.1086/505526. URL: https://doi.org/10.1086/505526.

Cutri, R. M. et al. (Nov. 2013). *Explanatory Supplement to the AllWISE Data Release Products*. Explanatory Supplement to the AllWISE Data Release Products.

Dabhade, P. et al. (Oct. 2020). "Search and analysis of giant radio galaxies with associated nuclei (SAGAN). I. New sample and multi-wavelength studies". In: *A&A* 642, A153, A153. DOI: 10.1051/0004-6361/202038344. arXiv: 2005.03708 [astro-ph.GA].

de Jong, Jelte T. A. et al. (Aug. 2017). "The third data release of the Kilo-Degree Survey and associated data products". In: *A&A* 604, A134, A134. DOI: 10.1051/0004-6361/201730747. arXiv: 1703.02991 [astro-ph.GA].

Dennett-Thorpe, J. et al. (Mar. 2002). "Jet reorientation in active galactic nuclei: two winged radio galaxies". In: *MNRAS* 330.3, pp. 609–620. DOI: 10.1046/j.1365-8711.2002.05106.x. arXiv: astro-ph/0110339 [astro-ph].

di Serego Alighieri, S. et al. (Aug. 1994). "New identifications and redshifts for southern 2-Jy radio sources." In: *MNRAS* 269, pp. 998–1010. DOI: 10.1093/mnras/269.4.998.

Eckart, A. et al. (Nov. 1986). "Investigation of a complete sample of flat spectrum radio sources from the S5 Survey. I. Analysis." In: *A&A* 168, pp. 17–24.

Eilek, J. A. et al. (Mar. 1984). "What bends 3C 465 ?" In: *ApJ* 278, pp. 37–50. DOI: 10.1086/161765.

Ekers, R. D. et al. (Dec. 1978). "NGC326 - A radio galaxy with a precessing beam". In: *Nature* 276, pp. 588–590. DOI: 10.1038/276588a0.

Ekers, R. D. et al. (Feb. 1989). "A complete sample of radio galaxies - I. The radio data." In: *MNRAS* 236, pp. 737–777. DOI: 10.1093/mnras/236.4.737.

Emonts, B. H. C. et al. (Apr. 2011). "MOLECULAR CO(1–0) GAS IN THE z $\sim$ 2 RADIO GALAXY MRC 0152-209". In: *ApJ* 734.1, p. L25. DOI: 10.1088/2041-8205/734/1/l25. URL: https://doi.org/10.1088/2041-8205/734/1/l25.

Erdoğdu, P. et al. (June 2006a). "The dipole anisotropy of the 2 Micron All-Sky Redshift Survey". In: *MNRAS* 368.4, pp. 1515–1526. DOI: 10.1111/j.1365-2966.2006.10243.x. arXiv: astro-ph/0507166 [astro-ph].

Erdoğdu, Pirin et al. (Nov. 2006b). "Reconstructed density and velocity fields from the 2MASS Redshift Survey". In: *MNRAS* 373.1, pp. 45–64. DOI: 10.1111/j.1365-2966.2006.11049.x. arXiv: astro-ph/0610005 [astro-ph].

Fanaroff, B. L. and J. M. Riley (Apr. 1974). "The Morphology of Extragalactic Radio Sources of High and Low Luminosity". In: *MNRAS* 167.1, 31P–36P. ISSN: 0035-8711. DOI: 10.1093/mnras/167.1.31P. eprint: https://academic.oup.com/

mnras/article-pdf/167/1/31P/8079923/mnras167-031P.pdf. URL: https://doi.org/10.1093/mnras/167.1.31P.

Ferrarese, Laura and David Merritt (Aug. 2000). "A Fundamental Relation between Supermassive Black Holes and Their Host Galaxies". In: *ApJ* 539.1, pp. L9–L12. DOI: 10.1086/312838. URL: https://doi.org/10.1086/312838.

Fleenor, Matthew C. et al. (Sept. 2005). "Large-Scale Velocity Structures in the Horologium-Reticulum Supercluster". In: *AJ* 130.3, pp. 957–967. DOI: 10.1086/431972. arXiv: astro-ph/0505361 [astro-ph].

Fleenor, Matthew C. et al. (Mar. 2006). "Redshifts and Velocity Dispersions of Galaxy Clusters in the Horologium-Reticulum Supercluster". In: *AJ* 131.3, pp. 1280–1287. DOI: 10.1086/500197. arXiv: astro-ph/0512169 [astro-ph].

Flesch, Eric W. (Mar. 2015). "The Half Million Quasars (HMQ) Catalogue". In: *Publ. Astron. Soc. Australia* 32, e010, e010. DOI: 10.1017/pasa.2015.10. arXiv: 1502.06303 [astro-ph.GA].

Fugmann, W., K. Meisenheimer, and H. J. Roeser (Oct. 1988). "CCD identification and classification of 5 GHz radio sources." In: *A&AS* 75, pp. 173–183.

Fujita, Yutaka et al. (Aug. 2002). "ChandraObservations of the Disruption of the Cool Core in A133". In: *AJ* 575.2, pp. 764–778. DOI: 10.1086/341352. URL: https://doi.org/10.1086/341352.

García-Burillo, S. et al. (July 2014). "Molecular line emission in NGC 1068 imaged with ALMA. I. An AGN-driven outflow in the dense molecular gas". In: *A&A* 567, A125, A125. DOI: 10.1051/0004-6361/201423843. arXiv: 1405.7706 [astro-ph.GA].

Gebhardt, Karl et al. (Aug. 2000). "A Relationship between Nuclear Black Hole Mass and Galaxy Velocity Dispersion". In: *ApJ* 539.1, pp. L13–L16. DOI: 10.1086/312840. arXiv: astro-ph/0006289 [astro-ph].

Gergely, László Árpád and Peter L. Biermann (June 2009). "The Spin-Flip Phenomenon in Supermassive Black hole binary mergers". In: *ApJ* 697.2, pp. 1621–1633. DOI: 10.1088/0004-637X/697/2/1621. arXiv: 0704.1968 [astro-ph].

Greene, Jenny E. and Luis C. Ho (Apr. 2006). "The M_{BH}-σ_* Relation in Local Active Galaxies". In: *ApJ* 641.1, pp. L21–L24. DOI: 10.1086/500507. arXiv: astro-ph/0512461 [astro-ph].

Hardcastle, M. J., D. A. Evans, and J. H. Croston (July 2009). "The active nuclei of z < 1.0 3CRR radio sources". In: *MNRAS* 396.4, pp. 1929–1952. DOI: 10.1111/j.1365-2966.2009.14887.x. arXiv: 0904.1323 [astro-ph.GA].

Heywood, Ian (Sept. 2020). *oxkat: Semi-automated imaging of MeerKAT observations*. ascl: 2009.003.

Hotan, A. W. et al. (Mar. 2021). "Australian square kilometre array pathfinder: I. system description". In: *Publ. Astron. Soc. Australia* 38, e009, e009. DOI: 10.1017/pasa.2021.1. arXiv: 2102.01870 [astro-ph.IM].

Hubble, E. P. (Dec. 1926). "Extragalactic nebulae." In: *ApJ* 64, pp. 321–369. DOI: 10.1086/143018.

Huchra, John P. et al. (Apr. 2012). "The 2MASS Redshift Survey—Description and Data Release". In: *ApJS* 199.2, 26, p. 26. DOI: 10.1088/0067-0049/199/2/26. arXiv: 1108.0669 [astro-ph.CO].

Hurley-Walker, N. et al. (Jan. 2017). "GaLactic and Extragalactic All-sky Murchison Widefield Array (GLEAM) survey - I. A low-frequency extragalactic catalogue". In: *MNRAS* 464.1, pp. 1146–1167. DOI: 10.1093/mnras/stw2337. arXiv: 1610.08318 [astro-ph.GA].

Intema, H. T. et al. (Feb. 2017). "The GMRT 150 MHz all-sky radio survey. First alternative data release TGSS ADR1". In: *A&A* 598, A78, A78. DOI: 10.1051/0004-6361/201628536. arXiv: 1603.04368 [astro-ph.CO].

Jarrett, T. H. et al. (May 2000). "2MASS Extended Source Catalog: Overview and Algorithms". In: *AJ* 119.5, pp. 2498–2531. DOI: 10.1086/301330. arXiv: astro-ph/0004318 [astro-ph].

Jonas, J. and MeerKAT Team (Jan. 2016). "The MeerKAT Radio Telescope". In: *MeerKAT Science: On the Pathway to the SKA*, p. 1.

Jones, D. Heath et al. (Dec. 2004). "The 6dF Galaxy Survey: samples, observational techniques and the first data release". In: *MNRAS* 355.3, pp. 747–763. DOI: 10.1111/j.1365-2966.2004.08353.x. arXiv: astro-ph/0403501 [astro-ph].

Jones, D. Heath et al. (Aug. 2005). "Second Data Release of the 6dF Galaxy Survey". In: *Publ. Astron. Soc. Australia* 22.3, pp. 277–286. DOI: 10.1071/AS05018. arXiv: astro-ph/0505068 [astro-ph].

Jones, D. Heath et al. (June 2006). "Near-infrared and optical luminosity functions from the 6dF Galaxy Survey". In: *MNRAS* 369.1, pp. 25–42. DOI: 10.1111/j.1365-2966.2006.10291.x. arXiv: astro-ph/0603609 [astro-ph].

Jones, Paul A. and W. B. McAdam (May 1992). "The Structure of Southern Extragalactic Radio Sources". In: *ApJS* 80, p. 137. DOI: 10.1086/191662.

Jones, T. W. and F. N. Owen (Dec. 1979). "Hot gas in elliptical galaxies and the formation of head-tail radio sources". In: *ApJ* 234, pp. 818–824. DOI: 10.1086/157561.

Joshi, Ravi et al. (Dec. 2019). "X-shaped Radio Galaxies: Optical Properties, Large-scale Environment, and Relationship to Radio Structure". In: *ApJ* 887.2, p. 266. DOI: 10.3847/1538-4357/ab536f. URL: https://doi.org/10.3847/1538-4357/ab536f.

Joye, W. A. and E. Mandel (Jan. 2003). "New Features of SAOImage DS9". In: *Astronomical Data Analysis Software and Systems XII*. Ed. by H. E. Payne, R. I. Jedrzejewski, and R. N. Hook. Vol. 295. Astronomical Society of the Pacific Conference Series, p. 489.

Kellermann, K. I. et al. (Oct. 1989). "VLA Observations of Objects in the Palomar Bright Quasar Survey". In: *AJ* 98, p. 1195. DOI: 10.1086/115207.

Kenyon, J. S. et al. (Aug. 2018). "CUBICAL - fast radio interferometric calibration suite exploiting complex optimization". In: *MNRAS* 478.2, pp. 2399–2415. DOI: 10.1093/mnras/sty1221. arXiv: 1805.03410 [astro-ph.IM].

Kondapally, R. et al. (Apr. 2021). "The LOFAR Two-meter Sky Survey: Deep Fields Data Release 1. III. Host-galaxy identifications and value added catalogues". In: *A&A* 648, A3, A3. DOI: 10.1051/0004-6361/202038813. arXiv: 2011.08201 [astro-ph.GA].

Kormendy, John and Luis C. Ho (Aug. 2013). "Coevolution (Or Not) of Supermassive Black Holes and Host Galaxies". In: *ARA&A* 51.1, pp. 511–653. DOI: 10.1146/annurev-astro-082708-101811. arXiv: 1304.7762 [astro-ph.CO].

Kormendy, John and Douglas Richstone (Jan. 1995). "Inward Bound—The Search For Supermassive Black Holes In Galactic Nuclei". In: *ARA&A* 33, p. 581. DOI: 10.1146/annurev.aa.33.090195.003053.

Kraft, R. P. et al. (Mar. 2005). "A Chandra Study of the Multicomponent X-Ray Emission from the X-shaped Radio Galaxy 3C 403". In: *ApJ* 622.1, pp. 149–159. DOI: 10.1086/427822. arXiv: astro-ph/0501031 [astro-ph].

Lacy, M. et al. (Mar. 2020). "The Karl G. Jansky Very Large Array Sky Survey (VLASS). Science Case and Survey Design". In: *PASP* 132.1009, 035001, p. 035001. DOI: 10.1088/1538-3873/ab63eb. arXiv: 1907.01981 [astro-ph.IM].

Laing, R. A., J. M. Riley, and M. S. Longair (July 1983). "Bright radio sources at 178 MHz : flux densities, optical identifications and the cosmological evolution of powerful radio galaxies." In: *MNRAS* 204, pp. 151–187. DOI: 10.1093/mnras/204.1.151.

Lal, Dharam Vir and A. Pramesh Rao (Jan. 2005). "3C 223.1: A source with unusual spectral properties". In: *MNRAS* 356.1, pp. 232–236. DOI: 10.1111/j.1365-2966.2004.08442.x.

Large, M. I. et al. (Apr. 1994). "Increasing the field size of the Molonglo Observatory Synthesis Telescope". In: *Publ. Astron. Soc. Australia* 11.1, pp. 44–49. DOI: 10.1017/S1323358000019652.

Leahy, J. P. and P. Parma (Jan. 1992). "Multiple outbursts in radio galaxies." In: *Extragalactic Radio Sources. From Beams to Jets*. Ed. by Jacques Roland, Hilhne Sol, and Guy Pelletier, pp. 307–308.

Leahy, J. P. and A. G. Williams (Oct. 1984). "The bridges of classical double radio sources." In: *MNRAS* 210, pp. 929–951. DOI: 10.1093/mnras/210.4.929.

Lynden-Bell, D. (Aug. 1969). "Galactic Nuclei as Collapsed Old Quasars". In: *Nature* 223.5207, pp. 690–694. DOI: 10.1038/223690a0.

Machalski, J. et al. (May 2008). "J1420-0545: The Radio Galaxy Larger than 3C 236". In: *ApJ* 679.1, pp. 149–155. DOI: 10.1086/586703. arXiv: 0808.2742 [astro-ph].

Madau, Piero and Mark Dickinson (Aug. 2014). "Cosmic Star-Formation History". In: *ARA&A* 52, pp. 415–486. DOI: 10.1146/annurev-astro-081811-125615. arXiv: 1403.0007 [astro-ph.CO].

Magorrian, John et al. (June 1998). "The Demography of Massive Dark Objects in Galaxy Centers". In: *AJ* 115.6, pp. 2285–2305. DOI: 10.1086/300353. arXiv: astro-ph/9708072 [astro-ph].

Mahatma, V H et al. (Jan. 2018). "Remnant radio-loud AGN in the Herschel-ATLAS field". In: *MNRAS* 475.4, pp. 4557–4578. ISSN: 0035-8711. DOI: 10.1093/mnras/sty025. eprint: https://academic.oup.com/mnras/article-pdf/475/4/4557/23995949/sty025.pdf. URL: https://doi.org/10.1093/mnras/sty025.

Malarecki, J. M. et al. (June 2013). "Giant radio galaxies - I. Intergalactic barometers". In: *MNRAS* 432.1, pp. 200–224. DOI: 10.1093/mnras/stt471. arXiv: 1303.4825 [astro-ph.CO].

Malarecki, J. M. et al. (May 2015). "Giant radio galaxies - II. Tracers of large-scale structure". In: *MNRAS* 449.1, pp. 955–986. DOI: 10.1093/mnras/stv273. arXiv: 1502.03954 [astro-ph.GA].

Mateos, S. et al. (Nov. 2012). "Using the Bright Ultrahard XMM-Newton survey to define an IR selection of luminous AGN based on WISE colours". In: *MNRAS* 426.4, pp. 3271–3281. DOI: 10.1111/j.1365-2966.2012.21843.x. arXiv: 1208.2530 [astro-ph.CO].

Mauch, T. et al. (July 2003). "SUMSS: a wide-field radio imaging survey of the southern sky - II. The source catalogue". In: *MNRAS* 342.4, pp. 1117–1130. DOI: 10.1046/j.1365-8711.2003.06605.x. arXiv: astro-ph/0303188 [astro-ph].

McMahon, Richard G. et al. (Nov. 2002). "Optical Counterparts for 70,000 Radio Sources: APM Identifications for the FIRST Radio Survey". In: *ApJS* 143.1, pp. 1–23. DOI: 10.1086/342623. arXiv: astro-ph/0110437 [astro-ph].

McMullin, J. P. et al. (Oct. 2007). "CASA Architecture and Applications". In: *Astronomical Data Analysis Software and Systems XVI*. Ed. by R. A. Shaw, F. Hill, and D. J. Bell. Vol. 376. Astronomical Society of the Pacific Conference Series, p. 127.

Merritt, David and R. D. Ekers (Aug. 2002). "Tracing Black Hole Mergers Through Radio Lobe Morphology". In: *Science* 297.5585, pp. 1310–1313. DOI: 10.1126/science.1074688. arXiv: astro-ph/0208001 [astro-ph].

Mills, B. Y. (Jan. 1981). "The Molonglo Observatory synthesis telescope". In: *Proceedings of the Astronomical Society of Australia* 4.2, pp. 156–159. DOI: 10.1017/S1323358000016222.

Mingo, B. et al. (Nov. 2016). "The MIXR sample: AGN activity versus star formation across the cross-correlation of WISE, 3XMM, and FIRST/NVSS". In: *MNRAS* 462.3, pp. 2631–2667. DOI: 10.1093/mnras/stw1826. arXiv: 1607.06471 [astro-ph.GA].

Mingo, B. et al. (Sept. 2019). "Revisiting the Fanaroff-Riley dichotomy and radio-galaxy morphology with the LOFAR Two-Metre Sky Survey (LoTSS)". In: *MNRAS* 488.2, pp. 2701–2721. DOI: 10.1093/mnras/stz1901. arXiv: 1907.03726 [astro-ph.GA].

Morganti, Raffaella et al. (Sept. 2013). "Radio Jets Clearing the Way Through a Galaxy: Watching Feedback in Action". In: *Science* 341.6150, pp. 1082–1085. DOI: 10.1126/science.1240436. arXiv: 1309.1240 [astro-ph.CO].

Mukherjee, Dipanjan et al. (Sept. 2016). "Relativistic jet feedback in high-redshift galaxies - I. Dynamics". In: *MNRAS* 461.1, pp. 967–983. DOI: 10.1093/mnras/stw1368. arXiv: 1606.01143 [astro-ph.HE].

Murphy, T. et al. (Nov. 2007). "The second epoch Molonglo Galactic Plane Survey: compact source catalogue". In: *MNRAS* 382.1, pp. 382–392. DOI: 10.1111/j.1365-2966.2007.12379.x. arXiv: 0708.3092 [astro-ph].

Nilsson, K. (Oct. 1998). "Kinematical models of double radio sources and the unified scheme. II. The database". In: *A&AS* 132, pp. 31–37. DOI: 10.1051/aas:1998442.

Norris, Ray P. et al. (Dec. 2006). "Deep ATLAS Radio Observations of the Chandra Deep Field-South/Spitzer Wide-Area Infrared Extragalactic Field". In: *AJ* 132.6, pp. 2409–2423. DOI: 10.1086/508275. arXiv: astro-ph/0610538 [astro-ph].

O'Dea, C. P. and F. N. Owen (Feb. 1986). "Multifrequency VLA Observations of the Prototypical Narrow-Angle Tail Radio Source, NGC 1265". In: *ApJ* 301, p. 841. DOI: 10.1086/163948.

O'Donoghue, Aileen A., Jean A. Eilek, and Frazer N. Owen (May 1993). "Flow Dynamics and Bending of Wide-Angle Tailed Radio Sources". In: *ApJ* 408, p. 428. DOI: 10.1086/172600.

Offringa, A. R. et al. (Oct. 2014). "WSCLEAN: an implementation of a fast, generic wide-field imager for radio astronomy". In: *MNRAS* 444.1, pp. 606–619. DOI: 10.1093/mnras/stu1368. arXiv: 1407.1943 [astro-ph.IM].

Olsen, E. T. (Sept. 1970). "Optical identification of radio source selected from the 4C catalogue." In: *AJ* 75, pp. 764–777. DOI: 10.1086/111023.

Planck Collaboration et al. (Sept. 2016). "Planck 2015 results. XIII. Cosmological parameters". In: *A&A* 594, A13, A13. DOI: 10.1051/0004-6361/201525830. arXiv: 1502.01589 [astro-ph.CO].

Proust, D. et al. (Feb. 2006). "Structure and dynamics of the Shapley Supercluster. Velocity catalogue, general morphology and mass". In: *A&A* 447.1, pp. 133–144. DOI: 10.1051/0004-6361:20052838. arXiv: astro-ph/0509903 [astro-ph].

Quici, Benjamin et al. (Feb. 2021). "Remnant radio galaxies discovered in a multi-frequency survey". In: *Publ. Astron. Soc. Australia* 38, e008, e008. DOI: 10.1017/pasa.2020.49. arXiv: 2101.09761 [astro-ph.GA].

Reid, R. I., P. P. Kronberg, and R. A. Perley (Oct. 1999). "VLA Images at 5 GHz of 212 Southern Extragalactic Objects". In: *ApJS* 124.2, pp. 285–381. DOI: 10.1086/313259. URL: https://doi.org/10.1086/313259.

Rizza, E. et al. (Jan. 2000). "X-Ray and Radio Interactions in the Cores of Cooling Flow Clusters". In: *AJ* 119.1, pp. 21–31. DOI: 10.1086/301167. URL: https://doi.org/10.1086/301167.

Robertson, J. G. (Jan. 1991). "The Most and Other Radio Telescope". In: *Australian Journal of Physics* 44.6, pp. 729–742. DOI: 10.1071/PH910729.

Robitaille, Thomas and Eli Bressert (Aug. 2012). *APLpy: Astronomical Plotting Library in Python*. ascl: 1208.017.

Safouris, V. et al. (Feb. 2009). "MRCB0319-454: probing the large-scale structure with a giant radio galaxy". In: *MNRAS* 393.1, pp. 2–20. DOI: 10.1111/j.1365-2966.2008.14181.x. arXiv: 0812.2052 [astro-ph].

Salpeter, E. E. (Aug. 1964). "Accretion of Interstellar Matter by Massive Objects." In: *ApJ* 140, pp. 796–800. DOI: 10.1086/147973.

Schilizzi, R. T. and W. B. McAdam (Jan. 1975). "Observations of extended sources at 408 MHz. I. The radio structures." In: *Mem. RAS* 79, p. 1.

Schilizzi, RT (1975). "Observations of extended sources at 408 MHz. II-The optical fields". In: *Mem. Soc. Astron. Italiana* 79, pp. 75–100.

Seyfert, Carl K. (Jan. 1943). "Nuclear Emission in Spiral Nebulae." In: *ApJ* 97, p. 28. DOI: 10.1086/144488.

Shankar, Francesco, David H. Weinberg, and Jordi Miralda-Escudé (Jan. 2009). "Self-Consistent Models of the AGN and Black Hole Populations: Duty Cycles, Accretion Rates, and the Mean Radiative Efficiency". In: *ApJ* 690.1, pp. 20–41. DOI: 10.1088/0004-637X/690/1/20. arXiv: 0710.4488 [astro-ph].

Slee, O. B., R. A. Perley, and Betty C. Siegman (Jan. 1989). "A VLA survey of rich clusters of galaxies. I. Whole-cluster maps, source list and statistics." In: *Australian Journal of Physics* 42, pp. 633–732. DOI: 10.1071/PH890633.

Slee, O. B. et al. (Sept. 2001). "Four Extreme Relic Radio Sources in Clusters of Galaxies". In: *AJ* 122.3, pp. 1172–1193. DOI: 10.1086/322105. URL: https://doi.org/10.1086/322105.

Smith, R. M. and J. G. Robertson (Feb. 1985). "A radio and optical study of the radio galaxy PKS 0511-48." In: *MNRAS* 212, pp. 809–816. DOI: 10.1093/mnras/212.4.809.

Swarup, Govind (Jan. 1991). "Giant metrewave radio telescope (GMRT)". In: *IAU Colloq. 131: Radio Interferometry. Theory, Techniques, and Applications*. Ed. by T. J. Cornwell and R. A. Perley. Vol. 19. Astronomical Society of the Pacific Conference Series, pp. 376–380.

Thompson, A. R. et al. (Oct. 1980). "The Very Large Array." In: *ApJS* 44, pp. 151–167. DOI: 10.1086/190688.

Tingay, S. J. et al. (2013). "The Murchison Widefield Array: The Square Kilometre Array Precursor at Low Radio Frequencies". In: *Publ. Astron. Soc. Australia* 30, e007. DOI: 10.1017/pasa.2012.007.

Tritton, S. B. (1978). "Recent work with the UK Schmidt Telescope". In: *Publ. Astron. Soc. Australia* 3.3, 206–207. DOI: 10.1017/S1323358000024565.

Urry, C. Megan and Paolo Padovani (Sept. 1995). "Unified Schemes for Radio-Loud Active Galactic Nuclei". In: *PASP* 107, p. 803. DOI: 10.1086/133630. arXiv: astro-ph/9506063 [astro-ph].

van Velzen, Sjoert et al. (Aug. 2012). "Radio galaxies of the local universe. All-sky catalog, luminosity functions, and clustering". In: *A&A* 544, A18, A18. DOI: 10.1051/0004-6361/201219389. arXiv: 1206.0031 [astro-ph.CO].

Weston, S. D. et al. (Feb. 2018). "Automated cross-identifying radio to infrared surveys using the LRPY algorithm: a case study". In: *MNRAS* 473.4, pp. 4523–4537. DOI: 10.1093/mnras/stx2562. arXiv: 1710.01449 [astro-ph.GA].

White, Sarah V. et al. (June 2020a). "The GLEAM 4-Jy (G4Jy) Sample: I. Definition and the catalogue". In: *Publ. Astron. Soc. Australia* 37, e018, e018. DOI: 10.1017/pasa.2020.9. arXiv: 2004.13125 [astro-ph.GA].

White, Sarah V. et al. (June 2020b). "The GLEAM 4-Jy (G4Jy) Sample: II. Host galaxy identification for individual sources". In: *Publ. Astron. Soc. Australia* 37, e017, e017. DOI: 10.1017/pasa.2020.10. arXiv: 2004.13025 [astro-ph.GA].

Whittam, I. H. et al. (Oct. 2018). "The Stripe 82 1-2 GHz Very Large Array Snapshot Survey: host galaxy properties and accretion rates of radio galaxies". In: *MNRAS* 480.1, pp. 358–370. DOI: 10.1093/mnras/sty1787. arXiv: 1806.10143 [astro-ph.GA].

Williams, W. L. et al. (Feb. 2019). "The LOFAR Two-metre Sky Survey. III. First data release: Optical/infrared identifications and value-added catalogue". In: *A&A* 622, A2, A2. DOI: 10.1051/0004-6361/201833564. arXiv: 1811.07927 [astro-ph.GA].

Willis, A. G., R. G. Strom, and A. S. Wilson (Aug. 1974). "3C236, DA240; the largest radio sources known". In: *Nature* 250.5468, pp. 625–630. DOI: 10.1038/250625a0.

Worrall, D. M., M. Birkinshaw, and R. A. Cameron (Aug. 1995). "The X-Ray Environment of the Dumbbell Radio Galaxy NGC 326". In: *ApJ* 449, p. 93. DOI: 10.1086/176035.

Wright, Edward L. et al. (Nov. 2010). "THE WIDE-FIELD INFRARED SURVEY EXPLORER (WISE): MISSION DESCRIPTION AND INITIAL ON-ORBIT PERFORMANCE". In: *AJ* 140.6, pp. 1868–1881. DOI: 10.1088/0004-6256/140/6/1868. URL: https://doi.org/10.1088/0004-6256/140/6/1868.

Wu, Chen et al. (Oct. 2018). "Radio Galaxy Zoo: Claran – a deep learning classifier for radio morphologies". In: *Monthly Notices of the Royal Astronomical Society* 482.1,

pp. 1211–1230. ISSN: 0035-8711. DOI: 10.1093/mnras/sty2646. eprint: https://academic.oup.com/mnras/article-pdf/482/1/1211/26205089/sty2646.pdf. URL: https://doi.org/10.1093/mnras/sty2646.

Wyndham, JD (1966). "Optical Identification of Radio Sources in the 3c Revised Catalogue". In: *AJ* 144, p. 459.

Zinn, P. C., E. Middelberg, and E. Ibar (July 2011). "Infrared-faint radio sources: a cosmological view. AGN number counts, the cosmic X-ray background and SMBH formation". In: *A&A* 531, A14, A14. DOI: 10.1051/0004-6361/201016264. arXiv: 1104.0564 [astro-ph.CO].